

SILVER-PLATINUM CORE-SHELL NANOWIRES FOR
ELECTROCHEMICAL APPLICATIONS

A THESIS SUBMITTED TO
THE GRADUATE SCHOOL OF NATURAL AND APPLIED SCIENCES
OF
MIDDLE EAST TECHNICAL UNIVERSITY

BY

ŞENSU TUNCA

IN PARTIAL FULFILLMENT OF THE REQUIREMENTS
FOR
THE DEGREE OF MASTER OF SCIENCE
IN
METALLURGICAL AND MATERIALS ENGINEERING

JULY 2021

Approval of the thesis:

**SILVER-PLATINUM CORE-SHELL NANOWIRES FOR
ELECTROCHEMICAL APPLICATIONS**

submitted by **ŞENSU TUNCA** in partial fulfillment of the requirements for the degree of **Master of Science in Metallurgical and Materials Engineering, Middle East Technical University** by,

Prof. Dr. Halil Kalıpçılar
Dean, Graduate School of **Natural and Applied Sciences** _____

Prof. Dr. Cemil Hakan Gür
Head of the Department, **Metallurgical and Materials Eng.** _____

Prof. Dr. Hüsnü Emrah Ünalın
Supervisor, **Metallurgical and Materials Eng., METU** _____

Examining Committee Members:

Prof. Dr. Levent Kamil Toppare
Department of Chemistry, METU _____

Prof. Dr. Hüsnü Emrah Ünalın
Metallurgical and Materials Eng, METU _____

Assoc. Prof. Dr. Emrullah Görkem Günbaş
Department of Chemistry, METU _____

Assist. Prof. Dr. Yusuf Keleştemur
Metallurgical and Materials Eng, METU _____

Assist. Prof. Dr. Recep Yüksel
Department of Chemistry, ESOGÜ _____

Date: 14.07.2021

I hereby declare that all information in this document has been obtained and presented in accordance with academic rules and ethical conduct. I also declare that, as required by these rules and conduct, I have fully cited and referenced all material and results that are not original to this work.

Name, Last name : Şensu, Tunca

Signature :

ABSTRACT

SILVER-PLATINUM CORE-SHELL NANOWIRES FOR ELECTROCHEMICAL APPLICATIONS

Tunca, Şensu
Master of Science, Metallurgical and Materials Engineering
Supervisor : Prof. Dr. Hüsnü Emrah Ünalan

July 2021, 113 pages

Silver nanowire (Ag NW) networks are one of the most outstanding candidates for optoelectronic applications to replace the commercial transparent conducting oxides (TCOs). Their high mechanical stability, solution based and scalable, low-cost synthesis and deposition routes make them an advantageous candidate over TCOs for future electronics. However, the integration of NW networks into electronic devices requires high thermal, chemical and electrochemical stability of NWs. This work describes the fabrication of highly stable silver-platinum (Ag-Pt) core-shell NW networks to be utilized in both amperometric hydrogen peroxide (H_2O_2) sensors and supercapacitors.

Detailed morphological and structural characterization of the Ag-Pt core-shell NWs showed that conformal and galvanic replacement free Ag-Pt core-shell NWs were obtained. Ag-Pt core-shell NWs had superior stability in harsh H_2O_2 environments compared to bare Ag NWs. To examine the use of Ag-Pt core-shell NWs in H_2O_2 sensors, stability of Ag-Pt core-shell NWs against H_2O_2 was investigated. Following that, Ag-Pt core-shell NW based H_2O_2 sensors were fabricated and a sensitivity of

0.167 $\mu\text{A}/\mu\text{M}$, in the linear range of 8.16-160.60 μM with a detection limit of 4.75 μM in phosphate buffer (pH 7) medium was obtained from the fabricated sensors.

For the fabrication of supercapacitors, Ag-Pt core-shell NW networks were electrochemically deposited with nickel hydroxide ($\text{Ni}(\text{OH})_2$). The prepared Ag-Pt- $\text{Ni}(\text{OH})_2$ nanocomposite electrodes showed high stability during electrochemical measurements and a specific capacitance of 816.7 F/g at a current density of 5 A/g was obtained.

Deposition of a conformal Pt shell layer improved the chemical and electrochemical stability of Ag NWs so that they can be used as electrodes for amperometric H_2O_2 sensors and supercapacitors. The successfully demonstrated applications of Ag-Pt core-shell NWs herein revealed the potential of these materials for their use in other optoelectronic and energy devices.

Keywords: Silver-Platinum Core-Shell Nanowires, Amperometric H_2O_2 Sensors, Supercapacitors

ÖZ

ELEKTROKİMYASAL UYGULAMALAR İÇİN GÜMÜŞ-PLATİN ÇEKİRDEK-KABUK NANOTELLERİ

Tunca, Şensu
Yüksek Lisans, Metalurji ve Malzeme Mühendisliği
Tez Yöneticisi: Prof. Dr. Hüsnü Emrah Ünalın

Temmuz 2021, 113 sayfa

Gümüş nanotel ağları, optoelektronik uygulamalarda kullanılmak üzere ticari olarak temin edilebilen şeffaf iletken oksitlerin yerini alacak en seçkin adaylardan biridir. Yüksek mekanik kararlılıkları, solusyon bazlı ve ölçeklenebilir sentez ve biriktirme metotları, onları gelecekteki elektronik cihazlar için şeffaf iletken oksitlere göre avantajlı bir aday haline getirmektedir. Bununla birlikte, nanotel ağlarının elektronik cihazlara entegrasyonu, nanotellerin yüksek kararlılığa sahip olmasını gerektirmektedir. Bu çalışma, hem amperometrik hidrojen peroksit (H_2O_2) sensörü hem de süperkapasitörler olarak kullanılacak, oldukça kararlı gümüş-platin (Ag-Pt) çekirdek-kabuk nanotel ağ elektrotlarının üretimini açıklamaktadır.

Ag-Pt çekirdek kabuk nanotellerinin ayrıntılı morfolojik ve yapısal karakterizasyonu, galvanik yerdeğiştirme reaksiyonunun görülmediği konformal kaplamanın sağlandığı Ag-Pt çekirdek-kabuk nanotellerinin elde edildiğini göstermiştir. Ag-Pt çekirdek-kabuk NW'lerinin, yalın Ag NW'lere kıyasla zorlu H_2O_2 ortamlarında üstün kararlılığa sahip olduğu gösterilmiştir. Üretilen Ag-Pt çekirdek-kabuk nanotellerinin, H_2O_2 sensörlerinde kullanımını incelemek için, Ag-Pt çekirdek-kabuk nanotellerin H_2O_2 maruziyetine karşı kararlılığı araştırılmıştır.

Daha sonrasında Ag-Pt çekirdek-kabuk nanotel bazlı H₂O₂ sensörü üretilmiş ve fosfat tamponu (pH 7) içerisinde 8.16-160.60 µM liner aralığı, 0.167 µA/µM hassasiyet, 4.75 µM algılama sınırı elde edilmiştir.

Süperkapasitörlerin üretimi için, Ag-Pt çekirdek-kabuk nanoteller üzerinde elektrokimyasal biriktirme yöntemi ile Ni(OH)₂ biriktirmesi gerçekleştirilmiştir. Üretilen elektrotlar, elektrokimyasal ölçümler sırasında, 5 A/g akım yoğunluğunda 816.7 F/g özgül kapasitans ile daha yüksek kararlılık sergilemiştir.

Koruyucu Pt kabuk tabakası kaplaması, Ag nanotellerin kimyasal ve elektrokimyasal kararlılığını geliştirmiş, böylece amperometrik H₂O₂ sensörleri ve süperkapasitörler için elektrot olarak kullanılmalarını sağlamıştır. Ag-Pt çekirdek-kabuk nanotellerinin başarıyla gösterilen uygulamaları, bu malzemelerin diğer optoelektronik ve enerji cihazlarında kullanılmaları için potansiyelini ortaya çıkartmıştır.

Anahtar Kelimeler: Gümüş-Platin Çekirdek-Kabuk Nanoteller, Amperometrik H₂O₂ Sensörü, Süperkapasitör.

To my family,

ACKNOWLEDGMENTS

This work was funded by Scientific and Technological Research Council of Turkey (TÜBİTAK) under grant number 117E539.

Firstly, I would like to express my deepest appreciation to my advisor Prof. Dr. H. Emrah Ünal for his guidance, patience and motivation throughout this study. I am very grateful for all the precious support and opportunities he provided during this journey and always feel lucky to work under his supervision.

I am also very thankful to Prof. Dr. Levent Kamil Toppare who shared my enthusiasm when I was an undergraduate student and light up this path for me. I will always be grateful for his guidance.

I would like to express my greatest gratitude to my research partner Serkan Koylan, for his dearest friendship, support, encouragements and valuable ideas. All the work and struggle became fun when we faced them together. Also thank you for always lighting up my mood, it would't be the same without you.

I would like to thank my lab mates Yusuf Tütel, Merve Nur Güven, Alptekin Aydın, Elif Özlem Güner, Dr. Aryan Azad, Mete Batuhan Durukan, Doğanca Tigan, Sevim Polat, Dr. Şahin Coşkun, Loay Madbouly, Doğa Doğanay, Şeyma Koç, Selin Özkul, Ögeday Çiçek, Caner Görür, Dr. Asude Çetin, Dr. Duygu Tan, Tufan Bölükbaşı, Onuralp Çakır, Hazal Başköy, Alptuğ Calasın and Deniz Keskin. I have always felt very lucky to be part of such a friendly, fun and productive research group. I also thank to Dr. Gökhan Polat for his valuable guidance and help in the most difficult times.

I am also thankful to Ece Alpuğan, one of the most loving person I get to know. I will always remember her with her big and beautiful smile. Also to Özlem Ünal, she will always be in my good memories.

I would like to express my thanks to our project partners Prof. Seung Hwan Ko and Dr. Dongkwan Kim from Seoul National University for their collaboration, TEM and SEM analysis and also for their hospitality during our visits to Republic of Korea.

I owe my profound gratitude to my sister Benu Tunca Altıntaş and to my parents and grandparents for being the role models for me and for giving me their endless support, encouragements and love. Thank you for always being there for me.

TABLE OF CONTENTS

ABSTRACT	v
ÖZ	vii
ACKNOWLEDGMENTS	x
TABLE OF CONTENTS	xii
LIST OF TABLES	xvi
LIST OF FIGURES	xvii
LIST OF ABBREVIATIONS	xxiii
LIST OF SYMBOLS	xxv
CHAPTERS	
1 INTRODUCTION	1
2 METAL NANOWIRE NETWORKS	5
2.1 Synthesis of Nanowires	5
2.1.1 Polyol Synthesis of Ag NWs	5
2.2 Random Networks Formation	7
2.3 Drawbacks of Nanowire Networks	8
3 FABRICATION OF CORE-SHELL METAL NANOWIRES	11
3.1 Protective Coating of Metal Nanowires	11
3.1.1 Oxide Coating	11
3.1.2 Hydroxide/Sulfide Coating	13
3.1.3 Carbon-Based Material Coating	14
3.1.3.1 Graphene and Graphene Oxide	14
3.1.3.2 Carbon Nanotubes	16

3.1.3.3	Polymer Coating	17
3.1.4	Metal Coating.....	19
3.2	Mechanism of Solution Based Metal Coating	21
4	EXPERIMENTAL DETAILS	27
4.1	Fabrication of Nanowire Networks.....	27
4.1.1	Synthesis of Silver Nanowires	27
4.1.2	Fabrication of Silver Nanowire Networks	30
4.2	Fabrication of Silver-Platinum Core-Shell Nanowires	31
4.3	Nanowire Characterization Methods	32
4.3.1	Scanning Electron Microscopy (SEM)	32
4.3.2	Transmission Electron Microscopy (TEM)	32
4.3.3	X-Ray Diffraction Analysis (XRD).....	33
4.3.4	X-Ray Photoelectron Spectroscopy (XPS)	33
4.3.5	pH Measurements	33
4.4	Results.....	34
4.4.1	Silver Nanowires.....	34
4.4.1.1	Silver-Platinum Core-Shell Nanowires	34
5	SILVER-PLATINUM CORE-SHELL NANOWIRE NETWORK BASED HYDROGEN PEROXIDE SENSORS.....	39
5.1	Introduction.....	39
5.2	Working Principle	39
5.3	Types of Amperometric Sensors.....	41
5.3.1	Enzyme Based Sensors	41
5.3.2	Enzymeless Sensors	45

5.4	Experimental Procedure	50
5.4.1	Electrode Preparation	50
5.5	Characterization Methods.....	51
5.5.1	Electrochemical Measurements.....	51
5.6	Results and Discussion	52
5.6.1	Stability of Ag-Pt core-shell NWs.....	52
5.6.2	Stability of Bare Ag NWs.....	53
5.6.3	Performance of Amperometric H ₂ O ₂ Sensors	54
5.6.3.1	Performance of Ag-Pt Core-Shell NW electrodes	54
5.6.3.2	Performance of Bare Ag NW Electrodes	60
6	SILVER-PLATINUM CORE-SHELL NANOWIRE NETWORK BASED SUPERCAPACITOR ELECTRODES	63
6.1	Introduction	63
6.2	Working Principle of Supercapacitors.....	64
6.3	Types of Supercapacitors	65
6.3.1	Electrical Double Layer Capacitors.....	65
6.3.2	Pseudocapacitors	67
6.3.3	Hybrid Supercapacitors	70
6.4	Experimental Procedure	71
6.4.1	Fabrication of Core-Shell Nanowire Networks.....	71
6.5	Characterization Methods.....	71
6.5.1	Electrochemical Measurements.....	71
6.5.1.1	Cyclic Voltammetry (CV).....	72
6.5.1.2	Galvanostatic Charge-Discharge (GCD).....	73

6.5.1.3	Electrochemical Impedance Spectroscopy (EIS).....	75
6.6	Results and Discussion	76
6.6.1	Electrochemical Deposition of Ni(OH) ₂	76
6.6.2	Electrochemical Characterization	79
6.6.2.1	Nanocomposite Electrodes	79
7	CONCLUSIONS AND FUTURE RECOMMENDATIONS.....	85
7.1	Conclusions.....	85
7.2	Future Recommendations	86
	REFERENCES	89
	APPENDICES	
A.	Electrodeposition of Ni(OH) ₂ on NW Networks	107
B.	Symmetric Supercapacitor	107
C.	Permission License	110

LIST OF TABLES

TABLES

Table 1. Comparison of sensitivity, linear range, and detection limit of amperometric measurements with Ag-Pt core-shell NWs conducted with the addition of 1, 5 and 10 mM H ₂ O ₂	57
Table 2. Comparison of H ₂ O ₂ sensors in terms of their linear range and detection limit.....	60

LIST OF FIGURES

FIGURES

Figure 2.1 Schematic representation of the mechanism provided for the evaluation and growth of a penta-twinned Ag NW from a nanoparticle in the presence of PVP followed by the Ag atom diffusion toward the ends [3].	6
Figure 2.2 Current simulation corresponding to different sized systems where L/l is (a) 10 and (b) 40. Current simulation of systems having different junction to stick ratios G_j/G_s is (c) 0.01 and (d) 100 [10].	8
Figure 2.3 SEM images of Ag NWs stored under ambient conditions for 60 days, (a) Ag ₂ S nanoparticle formation on the surface of the Ag NWs, (b) discontinuities of Ag NWs via the formation of Ag nanoparticles (NPs), (c) formation of agglomerations of Ag. TEM-EDS spectrum results of (d) one NP on the surface of the Ag NW in (a), (e) one NP at the point of discontinuity in (b), (f) SEM-EDS result of the large particle in (c) [21].	10
Figure 3.1 (a) Cyclic voltammetry (CV) plot of bare Ag NW (purple colored curve with a scan rate of 20 mV/s) and Ag NW/MoO ₂ core-shell nanocomposite (at different scan rates from 20 to 2 mV/s) in 1M LiClO ₄ in PC [29]. (b) TEM images of Ag NW/ZnO core-shell structure with 30 nm ZnO thickness (inset showing the five-fold twinning of Ag NWs having a ZnO shell layer) [30]. (c) Graph of precursor concentration-dependent TiO ₂ layer thickness change (inset shows the synthesis route of Ag NWs/TiO ₂ core-shell NWs) [35].	13
Figure 3.2 (a) Schematic representation of the formation of Ag NW/NiAl double hydroxide core-shell structures [49]. (b) CV plots for the Ag NW/Cu ₂ S core-shell electrodes at different scan rates in 3M KOH electrolyte[52].	14
Figure 3.3 (a) Comparison of the capacitance retention of Ag NWs to Ag NW/graphene electrode in 2500 CV cycles [53]. (b) Schematic representation of the hybrid structure of tightly attached single layer graphene on welded Ag NWs after the sintering procedure [18]. (c) CV of the fabricated symmetric Ag NWs-GO supercapacitor at various scan rates [55].	16

Figure 3.4 (a) Changes in sheet resistance with respect to testing conditions (85 °C and 85% RH environment) [57]. (b) Time dependent temperature profile of the SWCNT-Ag NW composite electrode as a function of a driving voltage (from 2 to 12 V) (inset shows the temperature distribution) [58]..... 17

Figure 3.5 (a) Mean temperature of the pristine Ag NWs, Ag NWs-PEDOT:PSS, and Ag NWs-PEDOT:PSS/ITO TFHs with respect to bias voltage [63]. (b) SEM image of Ag NW-PANI composite (inset showing the lower magnification image) [65]. (c) Comparison of the CV results of GCE ((a) red curve), Ag NWs/GCE ((b) black curve), Ag NWs/PANI/GCE ((c) green curve), PANI/GCE ((d) blue curve) [65]. 19

Figure 3.6 (a) Schematic representation of Ag-Au core-shell NWs fabrication. (b) TEM image of Ag-Au core-shell NWs [67]. (c) Comparison of capacitance retention percentage in 1 M KOH electrolyte for Ag NW/PUA and Ag-Ni core-shell NWs/PUA. (inset shows the CV curves of Ag-Ni NWs with the number of cycles) [71]. 21

Figure 3.7 (a) Schematic illustration Ag-Pt core-shell formation by the galvanic replacement between Ag and Pt ions [70]. (b) Schematic illustration of different routes for the synthesis of hollow porous Ag-Pt alloy NPs with Pt skin and Ag-Pt core-shell NPs with Pt shell on Ag core [75]. 25

Figure 4.1 Photographs taken at the different stages of the polyol synthesis: (a) 1 min, (b) 30 min, (c) 40 min and (d) 80 min of the reaction..... 29

Figure 4.2 Photos showing the (a) spray deposition method of NWs and (b) spray deposited Ag NW networks on a glass substrate..... 30

Figure 4.3 (a) Schematic representation of the fabrication of Ag-Pt core-shell NWs. SEM image of (b) Ag NWs (inset showing a schematic of Ag NW) and (c) Ag-Pt core-shell NWs (inset showing a schematic of Ag-Pt NW). 32

Figure 4.4 (a) HR-TEM image of an individual Ag NW. (b) SEM images and (c) XRD pattern of Ag NWs fabricated via polyol method (JCPDS Card no: 04-0783). 34

Figure 4.5 (a) SEM image (insets shows lower magnification SEM image) and (b) HAADF-STEM image of Ag-Pt core-shell NWs (insets shows lower magnification

TEM image). (c) HR-TEM image of a Ag-Pt core-shell NW with corresponding lattice fringes of Ag (green), interface of Ag and Pt (white) and Pt (blue).	35
Figure 4.6 (a) XRD pattern of Ag-Pt core-shell NWs (JCPDS Card no: 04-0802), (b) Comparison of XRD patterns of bare Ag NWs (black) and Ag-Pt core-shell NWs (red). Fitted XPS spectra for (c) Ag 3d and (d) Pt 4f.....	37
Figure 4.7 (a) SEM image of Ag-Pt core-shell NWs and correspondingly EDS maps for (b) Ag and (c) Pt.....	37
Figure 5.1 Schematic showing the components and working principle of a biosensor [82].....	41
Figure 5.2 Schematic of the sensing mechanism of glucose biosensor based on (rGO/Hap/GOx) nanocomposite modified GCE [91].....	42
Figure 5.3 (a) LSV curves for bare SPCE (d) and modified SPCEs (with Ag NWs/rGO (a), rGO (b), GO (c), Ag NW (e)), (b) The amperometric current responses of the GOD/PVP-AgNWs/GCE in PBS solution (pH 7.4) to 3 mM glucose at a scan rate of 50 mV s ⁻¹ [83]. (c) Amperometric measurement of the biosensor based on Au NWs at an applied potential of -0.2 V (vs. SCE) for successive addition of 0.5 mM glucose. Inset showing the calibration curve [93]. (d) Comparison of the current responses of Au-Ag NRs based biosensors relative to the addition of 5 mM glucose, and 5 mM glucose in the presence of 0.5 mM AA, DA, UA in O ₂ saturated (pH 7.4) 0.2 M PBS [94].	45
Figure 5.4 Amperometric response of the Ag NW array sensor to the addition of (a) 0.01 mM (red line) and 0.1 mM (blue line) (b) 3.26 mM H ₂ O ₂ in the 0.1 M PBS solution (pH 7.4) under the applied potential of -0.2 V vs. SCE. (c) Calibration curves for the freshly prepared and 14 and 42 days stored Ag NW array based H ₂ O ₂ sensors [84]. (d) Electroactive surface area by CVs at 100 mV/s scan rate in 0.2 M KCl containing 20 mM K ₃ Fe(CN) ₆ (a) for bare GCE (b) for Au NW modified GCE [93]. (e) Amperometric response of Au-C-Pt/GCE with respect to different molarities of H ₂ O ₂ in 0.1 M pH 7.0 PBS at 0 V. (f) Amperometric measurement of Au-C-Pt/GCE during the successive addition of 25 mM 10 μl H ₂ O ₂ , GL, DA, UA, AA [109].	50

Figure 5.5 Schematic representation of the three-electrode setup used for the amperometric measurements in this work.	51
Figure 5.6 SEM images of the (a) Ag-Pt core-shell NWs without H ₂ O ₂ exposure. After applying (b) 1 mM, (c) 5 mM, (d) 10 mM H ₂ O ₂ onto the Ag-Pt core-shell NWs on the Si wafer (Insets shows high magnification SEM images).	53
Figure 5.7 SEM images of the (a) bare Ag NWs before any H ₂ O ₂ exposure. Ag NWs exposed to (b) 1 mM, (c) 5 mM, (d) 10 mM H ₂ O ₂ (Insets shows high magnification SEM images).	54
Figure 5.8 Change in current with respect to applied potential for the detection of 25 μ l of 5 mM H ₂ O ₂ in 0.1 M phosphate buffer (pH 7.0).	55
Figure 5.9 Amperometric response of Ag-Pt core-shell NW modified electrode with respect to subsequent addition of (a) 1 mM, (b) 5 mM, (c) 10 mM H ₂ O ₂ into 0.1 M phosphate buffer at an applied potential of +0.8 V (vs. Ag/AgCl).	56
Figure 5.10 Calibration plot of Ag-Pt core-shell NW electrode for (a) 1 mM, (b) 5 mM, (c) 10 mM H ₂ O ₂ addition with corresponding linear regression equations.	56
Figure 5.11 Amperometric response of Ag-Pt core-shell NW electrode to successive addition of (a) 1, 5, and 10 mM H ₂ O ₂ (b) 5 mM H ₂ O ₂ , GL, AA, urea and OA.	58
Figure 5.12 (a) Five successive amperometric responses of a single Ag-Pt core-shell NW electrode to 5 mM H ₂ O ₂ in 0.1 M phosphate buffer at an applied potential of + 0.8 V (vs. Ag/AgCl). (b) Bar chart showing the average current response of five amperometric measurements of the same Ag-Pt core-shell NW electrode against the successive addition of 5 mM H ₂ O ₂ in 0.1 M phosphate buffer at an applied potential of + 0.8 V (vs. Ag/AgCl). (c) Amperometric measurements of five different Ag-Pt core-shell NW electrodes against 5 mM H ₂ O ₂ in 0.1 M phosphate buffer at an applied potential of + 0.8 V (vs. Ag/AgCl). (d) Bar chart corresponding to the amperometric measurements of five identical electrodes against 5 mM H ₂ O ₂ in 0.1 M phosphate buffer at an applied potential of + 0.8 V (vs. Ag/AgCl).	59
Figure 5.13 Amperometric response of bare Ag NW electrodes for the detection of 10 mM (black) and 100 mM H ₂ O ₂ (red) under an applied potential of 0.8 V (vs. Ag/AgCl). (b) Calibration plot of bare Ag NW electrode for the addition of 100 mM	

H ₂ O ₂ with corresponding linear regression equation in the linear concentration range of 756-1800 μ M.	61
Figure 6.1 Ragone plot for the comparison of energy storage devices [114].	64
Figure 6.2 Types of supercapacitors [111].	65
Figure 6.3 Schematic of the EDL model of Gouy-Chapman-Stern [119].	67
Figure 6.4 Schematic representation of the processes occurring for (a) EDLC, (b) pseudocapacitive and (c) faradaic electrode materials [121].	68
Figure 6.5 Schematic illustration of the three-electrode setup configuration.	72
Figure 6.6 (a) Rectangular-box shaped ideal capacitor CV curve. CV curves of (b) EDLC and (c) redox reaction peaks of pseudocapacitive materials [131].	73
Figure 6.7 GCD curves for (a) EDLCs, (b) pseudocapacitive materials [131].	74
Figure 6.8 Representation of a typical Nyquist plot showing the behavior of an EDLC (green), a pseudocapacitive material (blue) and a battery (red) [121].	76
Figure 6.9 SEM images of the Ag-Pt-Ni(OH) ₂ nanocomposites fabricated using deposition times of (a) 100, (b) 200, (c) 400 and (d) 600 sec.	77
Figure 6.10 (a) SEM image, (b) EDS maps for Ag (blue), Pt (green) and Ni (red) for 400 sec Ni(OH) ₂ deposited Ag-Pt core-shell NWs.	77
Figure 6.11 (a) XPS spectrum of Ni 2p from Ag-Pt-Ni(OH) ₂ electrodes. (b) XRD patterns of Ag-Pt core-shell NWs (red) and Ag-Pt-Ni(OH) ₂ nanocomposite electrodes (black).	78
Figure 6.12 (a) CV plots of the Ag-Pt-Ni(OH) ₂ nanocomposite electrode in 1 M aqueous KOH electrolyte with scan rates ranging from 100 mV/s to 5 mV/s. (b) GCD curves of Ag-Pt-Ni(OH) ₂ electrode at current densities ranging from 40 A g ⁻¹ to 5 A g ⁻¹	81
Figure 6.13 (a) Comparison of the GCD curves of Ag-Ni(OH) ₂ and Ag-Pt-Ni(OH) ₂ electrodes at a current density of 5 A g ⁻¹ . (b) EIS of Ag-Pt-Ni(OH) ₂ and Ag-Ni(OH) ₂ electrodes.	82
Figure 6.14 CV plots of (a) Ag-Pt-Ni(OH) ₂ and (c) Ag-Ni(OH) ₂ electrodes in 1 M aqueous KOH electrolyte with scan rates ranging from 100 mV/s to 5 mV/s in the potential window of -0.1-0.75V. GCD curves of (b) Ag-Pt-Ni(OH) ₂ and (d) Ag-	

Ni(OH)₂ electrodes electrode at current densities ranging from 20 A g⁻¹ to 6 A g⁻¹.
..... 83

Figure 6.15 CV plots of (a) Ag-Pt-Ni(OH)₂ and (b) Ag-Ni(OH)₂ electrodes with scan rates ranging from 5 mV/s to 100 mV/s, (c) the comparison of Ag-Pt-Ni(OH)₂ (black curve) and Ag-Ni(OH)₂ (red curve) electrodes at the scan rate of 25 mV/s within the potential window of -0.3-0.8V in 1 M aqueous KOH electrolyte. 84

LIST OF ABBREVIATIONS

ABBREVIATIONS

AA	Ascorbic Acid
Ag	Silver
Ag NPs	Silver Nanoparticles
AgDe NPs	Silver Decahedral Nanoparticles
AgPR NPs	Silver Pentagonal Nanoparticles
Ag NWs	Silver Nanowires
AgCl	Silver Chloride
AgNO ₃	Silver Nitrate
ALD	Atomic Layer Deposition
Au	Gold
AP-SALD	Atmospheric Pressure Spatial Atomic Layer Deposition
AZO	Aluminum Doped Zinc Oxide
CNF	Carbon Nanofiber
CNT	Carbon Nanotube
CS	Chitosan
CV	Cyclic Voltammetry
Cu ₂ S	Copper(I) Sulfide
Cu(NO ₃) ₂ ·5H ₂ O	Copper(II) Nitrate Trihydrate
CVD	Chemical Vapour Deposition
DA	Dopamine
DI	Deionized
EDLC	Electrical Double Layer Capacitance
EDS	Energy Dispersive Spectrometry
EG	Ethylene Glycol
Fe	Iron
GCE	Glassy Carbon Electrode
GO	Graphene Oxide
GOx	Glucose Oxidase
HAuCl ₆	Chloroauric Acid
H ₂ O	Water
H ₂ O ₂	Hydrogen Peroxide
H ₂ SO ₄	Sulfuric Acid
H ₂ PtCl ₆	Chloroplatinic Acid
HR-TEM	High-resolution Transmission Electron Microscopy
ITO	Indium Tin Oxide
KBr	Potassium Bromide
K ₂ PtCl ₆	Potassium hexachloroplatinate(IV)

LiClO ₄	Lithium Perchlorate
MnO ₂	Manganese Dioxide
Mn ₃ O ₄	Trimanganese tetraoxide
MoO ₂	Molybdenum(IV) Oxide
NaCl	Sodium Chloride
NaOH	Sodium Hydroxide
Na ₂ S	Sodium Sulfide
Na ₂ MoO ₄	Sodium molybdate
Na ₂ Pt(OH) ₆	Disodium Hexahydroxoplatinate
Ni	Nickle
Ni(OH) ₂	Nickel Hydroxide
PANI	Polyaniline
PC	Propylene Carbonate
PEDOT:PSS	Poly(3,4-ethylenedioxythiophene) Polystyrene Sulfonate
PET	Polyethylene Teraphtalate
PMMA	Poly(methyl methacrylate)
PPy	Polypyrrole
Pt	Platinum
Pt NP	Platinum Nanoparticle
PTP	Polythiophene
PUA	Polyurethane
PUS	Polyuethane Sponge
PVP	Polyvinylpyrrolidone
rGO	Reduced Graphene Oxide
RH	Relative Humidity
RSD	Relative Standard Deviation
RuO ₂	Ruthenium(IV) Oxide
SEM	Scanning Electron Microscopy
SERS	Surface Enhanced Raman Scattering
SCE	Saturated Calomel Electrode
Si	Silicon
SPCE	Screen-Printed Carbon Electrode
STEM	Scanning Transmission Electron Microscopy
SWCNT	Single-Walled Carbon Nanotubes
TFH	Transparent Flexible Heater
TiO ₂	Titanium Dioxide
TTB	Titanium Tetrabutoxide
UA	Uric Acid
UV	Ultraviolet
WO ₃	Tungsten(VI) oxide
XPS	X-Ray Photoelectron Spectroscopy
XRD	x-Ray Diffraction
ZnO	Zinc Oxide

LIST OF SYMBOLS

SYMBOLS

μA	microamper
μM	micromolar
θ	theta
$^\circ$	degree
ϕ_c	Critical Percolation Concentration

CHAPTER 1

INTRODUCTION

As human life has evolved, human needs showed progress to different areas, therefore in addition to fulfilling the basic necessities of people, the desire to go beyond those needs made way for the development of more futuristic and sophisticated technologies. In this concept, many novel materials were developed over time, following the rapid replacement of previous materials with more advanced ones. Nanomaterials are one such type. Due to their small size, nanomaterials represent superior and unique properties compared to their bulk forms. Furthermore, by tuning the structure and morphology of the nanomaterials during the fabrication process, new materials with controlled properties can be developed. Medical and electronics industry, studies based on environmental recovery and energy applications gained momentum with the use of nanomaterials. Accordingly, for adoption to dynamic and modern human life, flexible, transparent and stretchable technologies have become a strong focus of the recent research efforts. Light emitting diodes (LEDs), energy storage devices such as batteries and supercapacitors, heaters, touch screens, solar cells, photodetectors, sensors and electrochromic devices are a few of the application areas covering the latest technological developments. In this regard, many new materials such as transparent conductive oxides (TCOs) were developed. Typical examples of TCOs include indium thin oxide (ITO), fluorine doped tin oxide (FTO) and aluminum doped zinc oxide (AZO). In addition, carbon-based materials like graphene, carbon nanotubes, buckyball, activated carbon, and some conductive polymers such as poly(3,4-ethylenedioxythiophene):polystyrene sulfonate (PEDOT:PSS), polyaniline (PANI) and polypyrrole (PPy) are also some of the most widely studied materials. However,

the brittle nature and high cost of TCOs in addition to the low conductivity of polymers, enabled the metal nanowires in network form to come to the fore. Being one of the promising candidates for flexible electronic devices, metal nanowire networks have attracted the attention of researchers. In this regard, silver nanowire (Ag NW) networks hold great potential for future electronics. Ag NW networks take up a large space in both research and industrial applications due to their high electrical and thermal conductivity, mechanical stability, and optical transparency. Also, the ease of large-scale synthesis and the possibility of Ag NWs to be deposited onto various substrates makes them a promising candidate. Overall, NW networks provide better if not similar properties than traditional TCOs and conductive polymers.

Although being an excellent alternative for transparent, stretchable and flexible electronics, Ag NWs are prone to oxidation and sulphurization under different environments. Therefore, for the large scale utilization of these NW networks, recent studies have focused on the enhancement of their chemical, thermal, electrochemical and environmental stabilities.

In this work, a protective platinum (Pt) shell layer is deposited onto Ag NWs with a simple solution based method. Electrochemical stability and oxidation resistance of Ag NW networks are enhanced to be utilized in amperometric hydrogen peroxide (H_2O_2) sensors and supercapacitors. A novel enzymeless H_2O_2 sensor and a supercapacitor are demonstrated. Highly stable Ag-Pt core-shell NWs are directly used as a sensor material for H_2O_2 detection, while nickel hydroxide ($\text{Ni}(\text{OH})_2$) is electrochemically deposited onto Ag-Pt core-shell NWs to be used as pseudocapacitive active material for supercapacitor electrodes.

This thesis contains 7 chapters. Chapter 2 covers the polyol synthesis route of Ag NWs and the formation of random NW networks in addition to the drawbacks of NW networks. Chapter 3 explains the fabrication route of core-shell NWs via

examples from the literature on the fabrication and utilization of protective coatings on NWs. Mechanism of the metal shell coating on NWs are also discussed through the examples in the literature. Experimental details are provided in Chapter 4, which presents the synthesis routes of bare Ag NWs, fabrication of random Ag NW networks and synthesis of Ag-Pt core-shell NWs. Characterization methods include scanning electron microscopy (SEM), transmission electron microscopy (TEM), X-ray diffraction (XRD) and X-ray photoelectron spectroscopy (XPS).

Chapter 5 describes the working principles of amperometric sensors together with an investigation on the classification of enzyme and enzymeless sensors. Electrode preparation is detailed and a comparison of the stability of Ag-Pt core-shell NWs and bare Ag NWs was presented under different molarities of H₂O₂ exposures. The chapter is completed by presenting the electrochemical measurements of the Ag-Pt core-shell NW based amperometric H₂O₂ sensors.

In Chapter 6, firstly working principles and different types of supercapacitors are discussed. Fabrication of the Ag-Pt core-shell NW networks for the supercapacitor electrodes is described and characterization of the deposited pseudocapacitive Ni(OH)₂ layer is presented. Electrochemical characterization methods are discussed followed by the three-electrode setup measurements of the Ag-Pt-Ni(OH)₂ nanocomposite electrodes.

Lastly, Chapter 7 concludes the work done in this thesis together with the future recommendations for the improvement of the described work.

CHAPTER 2

METAL NANOWIRE NETWORKS

2.1 Synthesis of Nanowires

The synthesis routes of nanostructured materials can be categorized into two groups, which are physical and chemical methods [1]. Chemical methods such as a polyol, photoreduction and template methods were preferred over physical methods since the impurities are inevitably introduced to the system during physical methods like mechanical pulverization [2].

2.1.1 Polyol Synthesis of Ag NWs

Solution based synthesis is highly efficient and cost-effective route for the large scale synthesis of Ag NWs [3]. Among different physical and chemical methods to synthesize Ag NWs, polyol synthesis is the most promising method considering the ease in mass production of Ag NWs [2].

The first demonstration of the polyol process was made by Fievet et al. [4] and in 2001, the first synthesis of the Ag NWs via the polyol method was performed by Sun et al [5]. In a typical polyol synthesis, solvent is generally ethylene glycol (EG) due to its high boiling point. EG is used both as a solvent and a reducing agent for the reduction of metal ions to metals so that the nucleation and growth can take place [4]. In addition to that, poly(vinylpyrrolidone) (PVP) is used as a capping agent and silver nitrate (AgNO_3) acts as a Ag source for the reaction [2]. During the course of the reaction, many factors affect the outcome of the synthesis and reaction products. The concentration of the constituents, the molecular weight of PVP, reaction temperature, use of single or combination of different metal salts (i.e. sodium

chloride (NaCl), copper(II) chloride (CuCl_2), and potassium bromide (KBr) highly affect the yield, aspect ratio and morphology of the Ag NWs [6]. During the polyol method, as the Ag nanoparticles (Ag NPs) are formed at the initial stages of the synthesis via nucleation, some of the NPs do dissolve and form larger NPs via Ostwald ripening mechanism. PVP passivates the $\{100\}$ faces of these pentatwinned seeds through either oxygen or nitrogen atoms in the PVP structure. On the other hand, weaker bonding between PVP and the $\{111\}$ faces leaves the $\{111\}$ faces open for the addition of Ag atoms [3]. Thanks to this mechanism, anisotropic growth of Ag NWs through $\langle 110 \rangle$ direction is achieved forming 5-fold twinned structures. In this concept, Coskun et al. also clarified the effect of the molar ratio of PVP: AgNO_3 on the length and diameter of Ag NWs and showed that an increase in PVP: AgNO_3 molar ratio decreases the length of the Ag NWs [7]. A schematic representation of the passivation of PVP and the addition of Ag atoms to the active sites during the polyol method is provided in Figure 2.1.

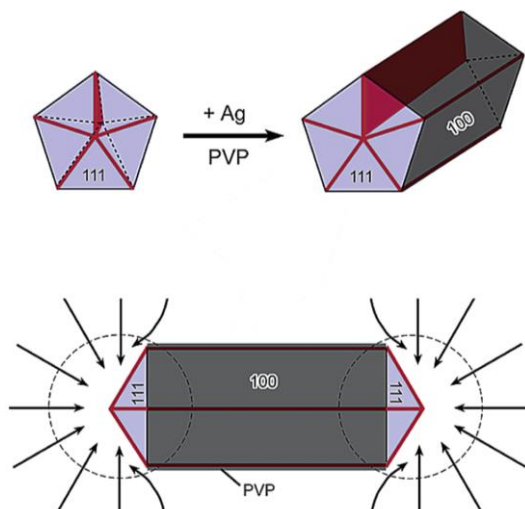


Figure 2.1 Schematic representation of the mechanism provided for the evaluation and growth of a penta-twinned Ag NW from a nanoparticle in the presence of PVP followed by the Ag atom diffusion toward the ends [3].

2.2 Random Networks Formation

The electrical properties of NWs were understood through the investigation of the formation of random networks and electrical percolation. Different simulation models were used to reveal the importance of critical percolation concentration, ϕ_c . Below this critical percolation concentration (threshold), which corresponds to the number of NWs per area at percolation, there is no conductivity for the system. The ϕ_c is also related to the aspect ratio (D/L , D = diameter, L = length) of the NWs, which further affects the optical properties of the NW networks [8]. To form a random NW network, different NW deposition methods were demonstrated such as spray coating, vacuum filtration, spin coating and drop coating [9].

Contact resistance at the junction points due to the existence of a thin layer of capping agent on NWs must be taken into consideration [9]. Žeželj et al. simulated the current passing through a 2D stick system, which explained the dependence of the conductivity on stick density (n) (in this case NW density) and on the junction to stick (G_j/G_s where G_j is the conductance of the stick, G_s is the conductance related to the stick to stick junction) conductance ratios. As shown in Figure 2.3, n_c corresponds to the critical percolation density, l is the stick length, L is the system size, L/l is the normalized system size and I_{max} is the maximal current in the system. When the density of the system is close or equal to the percolation threshold (n_c), the current is carried through only a small fraction of NWs and junctions (Figure 2.2 (a) and (b)). On the other hand at higher densities, where several NWs are connected forming various paths for current to pass through, conductivity highly depends on the junction to stick conductance values. In Figure 2.2 (c), at a lower G_j/G_s ratio, 0.01, where the conductivity of the junctions is low, the total current passes through the shortest path having the least number of junction points. On the contrary, with a higher G_j/G_s ratio current evenly passes through the multiple shortest paths in the system [10].

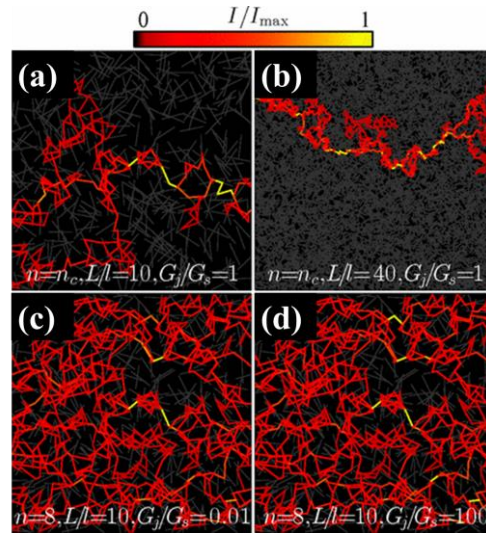


Figure 2.2 Current simulation corresponding to different sized systems where L/l is (a) 10 and (b) 40. Current simulation of systems having different junction to stick ratios G_j/G_s is (c) 0.01 and (d) 100 [10].

Since the network density and transparency are inversely related to each other, it is wise to control the aspect ratio of the NWs, which affects both the formation of the percolation network and optical properties. In addition to that, some post-treatments can also be performed for decreasing the contact resistance at the junction points [9]. Examples of those post-treatments include annealing [11],[12],[13], mechanical pressing [14],[15],[16] washing [15],[16],[17] and optical sintering [18],[19],[20]. These should be chosen according to the applications.

2.3 Drawbacks of Nanowire Networks

Although being a promising candidate for various device applications, Ag NWs suffer from their high tendency to get oxidized and sulphurized when subjected to water and ambient conditions [21]. This is because of their higher surface-to-volume ratio and thus surface reactivity compared to their bulk counterparts [22],[23]. Various studies were conducted on the investigation of stabilities of Ag NW networks that were stored in ambient conditions. Mayousse et al. showed that Ag NW network synthesized through the polyol method were stable under ambient

conditions for up to two and a half years [24]. On the other hand, Moon et al. showed that the Ag NW network lose its conductivity after 2 months [25]. Elechiguerra et al. showed morphological changes in Ag NWs within 3 weeks storage under ambient conditions. In addition, they found that the percolation network gets destroyed totally within 24 weeks [26]. In addition, Jiu et al. observed the formation of nanoparticles on the surface of Ag NWs in the first 60 days after fabrication when stored under ambient condition [23].

Deignan et al. investigated the effect of the electrode composition and processing parameters on the stability of Ag NWs [21]. It was reported that the diameter of Ag NWs, trace amount of leftover reactants, and PVP layer thickness of Ag NWs following post-processing techniques also affect the lifetime of the Ag NWs. Figure 2.3 shows SEM images associated with the three main causes of the degradation of Ag NWs under ambient conditions and their effect on the morphology and composition of Ag NWs. SEM image in Figure 2.3 (a) shows the formation of Ag nanoparticles (NPs) and corresponding EDS results are provided in Figure 2.3 (d), which represent the elemental outcome of the interaction of carbonyl sulfide (OCS) and hydrogen sulfide (H_2S) with Ag. This creates silver sulfide (Ag_2S) nanoparticles on the Ag NW surface causing discontinuities in the NW network after an experiment for 60 days. SEM image in Figure 2.3 (b) shows the effect of trace amount of Cl_2 (due to the use of NaCl in polyol synthesis) causing the rearrangement of the Ag into a nanoparticle and causing discontinuity of the Ag NWs. Corresponding EDS results are given in Figure 2.3 (e). Figure 2.3 (c) shows the SEM image observed for the dense networks of thin Ag NWs that predominantly undergo the formation of Ag agglomerates by the diffusion of Ag atoms from the NWs. EDS results in Figure 2.3 (f) shows that Ag agglomerates were also composed of trace amount of Cl and S.

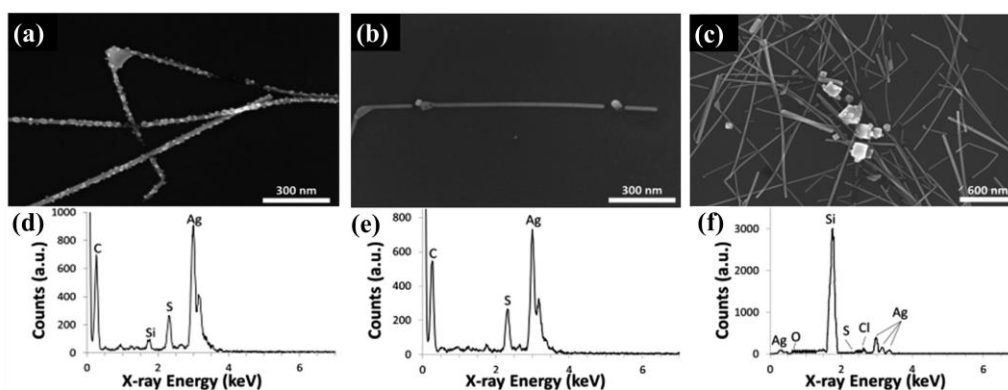


Figure 2.3 SEM images of Ag NWs stored under ambient conditions for 60 days, (a) Ag₂S nanoparticle formation on the surface of the Ag NWs, (b) discontinuities of Ag NWs via the formation of Ag nanoparticles (NPs), (c) formation of agglomerations of Ag. TEM-EDS spectrum results of (d) one NP on the surface of the Ag NW in (a), (e) one NP at the point of discontinuity in (b), (f) SEM-EDS result of the large particle in (c) [21].

In another study conducted by Jiu et al., humidity and light stability of Ag NWs were investigated [27]. Ag NW films were subjected to natural light under ambient conditions. Compared to their initial resistance, they experienced 3-5 folds and over 25 folds increase in resistance at the end of two weeks and three weeks, respectively. At the end of 30 weeks, films were completely destroyed. On the other hand, films that were kept under the same ambient conditions but were not subjected to natural light showed a slower resistance increase (5 folds over 30 days). In the same study effect of the moisture in the air was also investigated. At the end of 3 weeks, Ag NWs that were kept under 70-80 % relative humidity experienced a complete loss of film conductivity, whereas the films that were maintained in the desiccator maintained their initial resistance for over 2 months.

The instability of Ag NW electrodes under high current flow (17 mA cm^{-2}) was investigated by Khaligh et al [23]. As current passed through the electrode, the temperature of the electrode was found to rise due to Joule heating. However, junction points of the NWs experienced higher temperature values than the overall surface temperature. Such an effect of high current on Ag NWs causes the formation of NPs followed by the formation of broken Ag NWs and complete failure of the electrodes.

CHAPTER 3

FABRICATION OF CORE-SHELL METAL NANOWIRES

Considering the various factors affecting the NW stability, protective coating layers were started to be investigated. Coating of different protective layers such as metals, sulfides, hydroxides, oxides, and carbon-based materials like carbon nanotubes (CNTs), graphene, and polymers are widely demonstrated. With the additional coating layers, a core-shell approach can widen the application areas of metal nanowires through improving the device stabilities.

3.1 Protective Coating of Metal Nanowires

Promising electrical, optical and mechanical properties of NW networks depend on their chemical, environmental, electrochemical stabilities. Nowadays, many researchers study the development of NWs with enhanced stability for the improvement of both the lifetime and performance of the NW based devices [28]. For the development of electrochemical devices such as supercapacitors and amperometric H₂O₂ and/or glucose sensors different protective coating layers on NWs were explored such as oxide coatings, hydroxide/sulfide coatings, carbon-based coatings, and metal coatings forming core-shell, core-sheath, hybrid or coaxial nanostructures.

3.1.1 Oxide Coating

Oxide materials such as molybdenum (IV) oxide (MoO₂) [29], zinc oxide (ZnO) [13], [30]–[34], titanium dioxide (TiO₂) [35],[36],[37],[38], copper(I) oxide (Cu₂O) [39], trimanganese tetraoxide (Mn₃O₄) [40], aluminum oxide (Al₂O₃) [13],[41],[42], tungsten (VI) oxide (WO₃) [43] and silicon dioxide (SiO₂) [44],[45] were used as the

protective coating layers on Ag NWs. Various deposition procedures were investigated to coat Ag NWs with the indicated oxide layers. Typical coating methods include but not limited to electrochemical deposition [43],[29], atomic layer deposition (ALD) [13],[30],[41] and solution-phase methods [35],[39].

Electrodeposition of MoO₂ on Ag NWs was performed for the utilization of Ag NWs in supercapacitor applications. 0.1 M Na₂MoO₄ was used as the electrolyte and -1.2 V constant potential (vs. Ag/AgCl electrode) was applied for the electrodeposition of the MoO₂ layer. The optimum coating duration was determined as 800 sec corresponding to an approximately 180 nm thick MoO₂ layer. Compared to the bare Ag NW electrode, Ag NW/MoO₂ core-shell nanocomposite electrode had a large cyclic voltammetry (CV) curve area indicating the charge accumulation in the electrode, as shown in Figure 3.1 (a). With the introduction of the pseudocapacitive MoO₂ layer to Ag NWs, a supercapacitor with a specific capacitance of 500.7 F g⁻¹ at a current density of 0.25 A g⁻¹ was obtained with a capacitance retention of 90% after 5000 charge-discharge cycles [29]. In another study, atmospheric pressure spatial atomic layer deposition (AP-SALD) technique was used for the deposition of a conformal ZnO layer onto Ag NW network. Due to the hindrance of Ag diffusion, thermal and electrical stabilities of the network were improved. A thermal and electrical stability up to 500 °C and 18 V, were demonstrated, respectively. Figure 3.1 (b) shows the TEM image of the Ag NW/ZnO core-shell structure with a 30 nm ZnO layer, where the inset shows the five fold twinned Ag NWs with ZnO layer [30]. A solution based method was used for the deposition of TiO₂ shell layer onto Ag NWs using 5 μM titanium tetrabutoxide (TTB) for the functionalization of Ag NWs, followed by a hydrolysis procedure. The thickness of the TiO₂ shell was altered via changing the TTB concentration as shown in Figure 3.1 (c). Ag/TiO₂ core-shell network was stable up to 700 °C, which was far beyond the temperature that the Ag NWs could withstand [35]. In another study, Ag NWs were used for the fabrication of electrochromic devices (ECDs). For this purpose, an approximately 200 nm thick electrochromic WO₃ layer was deposited onto the Ag NW networks via the electrochemical deposition method. Gel electrolyte, lithium perchlorate

(LiClO₄) in propylene carbonate (PC), and poly(methyl methacrylate) (PMMA) were used for the device fabrication. Enhanced cyclic stability, up to 150 cycles, compared to the conventional ITO based ECDs were observed together with the high coloration efficiency of 86.9 cm² C⁻¹ (at 1100 nm) [43].

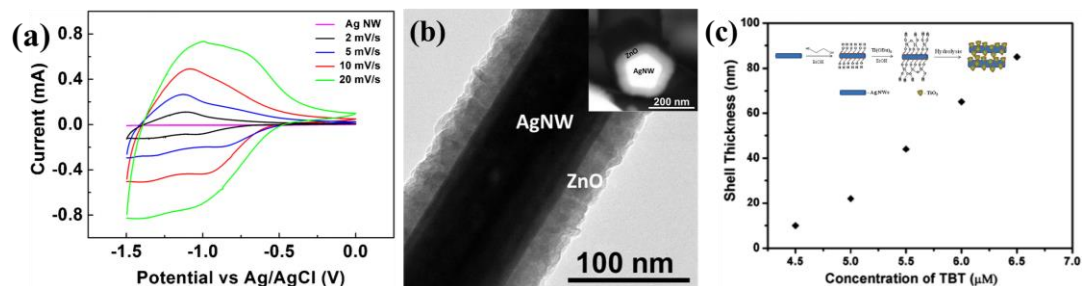


Figure 3.1 (a) Cyclic voltammetry (CV) plot of bare Ag NW (purple colored curve with a scan rate of 20 mV/s) and Ag NW/MoO₂ core-shell nanocomposite (at different scan rates from 20 to 2 mV/s) in 1M LiClO₄ in PC [29]. (b) TEM images of Ag NW/ZnO core-shell structure with 30 nm ZnO thickness (inset showing the five-fold twinning of Ag NWs having a ZnO shell layer) [30]. (c) Graph of precursor concentration-dependent TiO₂ layer thickness change (inset shows the synthesis route of Ag NWs/TiO₂ core-shell NWs) [35].

3.1.2 Hydroxide/Sulfide Coating

Ag NWs were coated with various hydroxide and sulfide materials such as Ni(OH)₂ [46],[47], double hydroxides of NiAl [48],[49], NiCo [50],[51] and Cu₂S [52]. In one example, Ni(OH)₂ shell was coated onto Ag NWs using the electrodeposition technique. Mechanically stable and flexible electrodes were obtained on polyethylene terephthalate (PET) substrates with a specific capacitance of 1165.2 F g⁻¹ at a current density of 3 A g⁻¹. After 3000 charge-discharge cycles, a capacitance retention of 93% was reported [46]. NiAl double hydroxide coating was studied by Wu et al and Ag NW/NiAl double hydroxide nanosheets were fabricated via hydrothermal (Figure 3.2 (a)). Compared to bare Ag NW networks, a specific capacitance of 1246.8 F g⁻¹ was obtained [49]. Cu₂S shell layer was coated onto drop casted Ag NWs using successive ionic layer adsorption and reaction (SILAR) method using 0.5 M copper(II) nitrate trihydrate (Cu(NO₃)₂·5H₂O) and 0.5 M

sodium sulfide (Na_2S). Ag NWs with a diameter of 30 nm were coated with a 55 nm thick Cu_2S shell layer. AgNWs/ Cu_2S core-shell electrodes prepared on Ni foam were subjected to CV and a specific capacitance of 707 Fg^{-1} was obtained (Figure 3.2 (b)) [52].

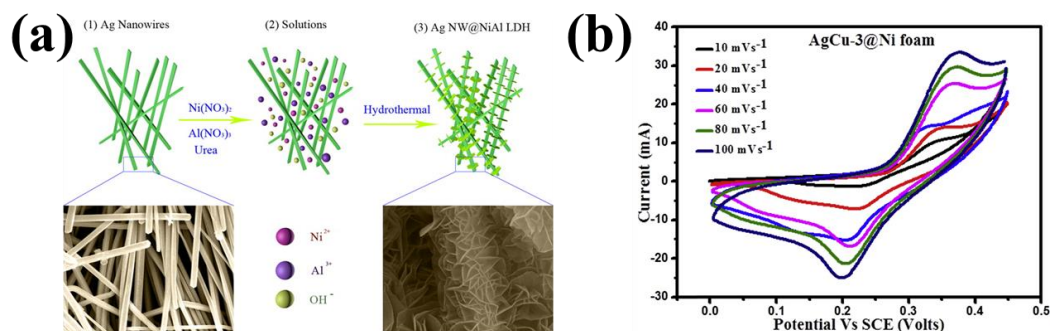


Figure 3.2 (a) Schematic representation of the formation of Ag NW/NiAl double hydroxide core-shell structures [49]. (b) CV plots for the Ag NW/ Cu_2S core-shell electrodes at different scan rates in 3M KOH electrolyte[52].

3.1.3 Carbon-Based Material Coating

Carbon-based protective coating layers were also investigated by many researchers due to their beneficial mechanical, electrochemical and electrical properties in addition to their high chemical stability and large specific surface area. Graphene [53],[54],[18], graphene oxide (GO) [55], [56] carbon nanotubes (CNTs) [57],[58], and polymer coatings such as poly(3,4-ethylenedioxythiophene) polystyrene sulfonate (PEDOT:PSS) [59],[60],[61],[62],[63] polypyrrole (PPy) [64], polyaniline (PANI) [65],[66] are some examples of carbon based coatings utilized for improving the stability of Ag NW networks.

3.1.3.1 Graphene and Graphene Oxide

It was demonstrated that the stability of Ag NW networks can be enhanced by a protective graphene layer. With the electrophoresis method, Ag NW/graphene composite electrodes with high electrochemical stability were fabricated by

Alshammari et al. The specific capacitance of the composite electrode was 108.4 F g^{-1} with a capacitance retention of 82.6% after 2500 cycles. This indicated the enhanced cycling stability of the electrodes as shown in Figure 3.3 (a) [53]. In another study, polycrystalline graphene grown with the chemical vapor deposition method (CVD) was used to fabricate Ag NW/graphene hybrid structure to be utilized as transparent conductive electrodes (TCEs). Low sheet resistance (R_s of $22 \text{ } \Omega/\square$) with high transmittance (88%) was obtained, where 2D sheets of graphene in the hybrid structure bridged the junctions of Ag NWs. High stability of the electrodes under atmospheric conditions, mechanical bending and mechanical pressure was achieved, all of which outperformed commercially available ITO [54]. In a study conducted by Yang et al., graphene was spray coated onto Ag NWs, where PMMA was used as the adhesive and optical sintering was performed for the welding of the junctions of Ag NW/graphene hybrid nanostructures. A schematic showing the hybrid structure of graphene attached and welded Ag NWs is provided in Figure 3.3 (b). In addition to the enhancement in the chemical stability with the use of graphene, sheet resistance of the hybrid electrode was also improved (from $47 \text{ } \Omega/\square$ to $13.9 \text{ } \Omega/\square$) during the sintering process. This was due to high lateral thermal conductivity of graphene that promoted the welding of Ag NWs [18].

A sandwich-like Ag NWs/graphene oxide (GO) structure was fabricated by Patil et al. [55]. The fabricated electrode had a specific capacitance of 251 F g^{-1} at 10 mV s^{-1} . A potential window of -0.2 to 0.8 V and an electrolyte of 0.1 M H_2SO_4 was used. A symmetric supercapacitor was also fabricated and analyzed in the potential window of 0 to 0.6 V (Figure 3.3 (c)). A specific capacitance of 154 F g^{-1} at a scan rate of 10 mV s^{-1} was obtained.

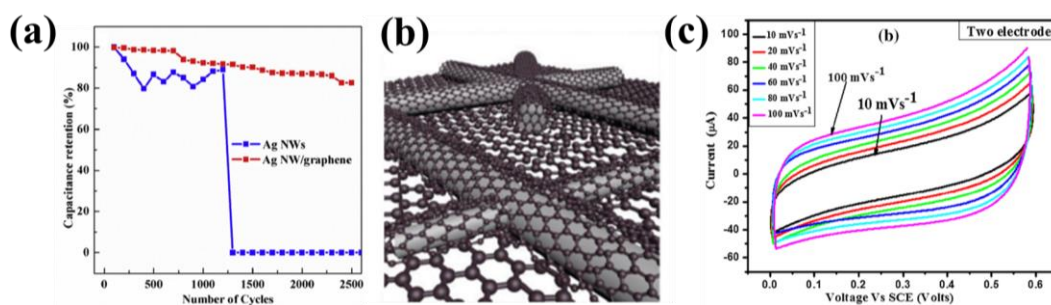


Figure 3.3 (a) Comparison of the capacitance retention of Ag NWs to Ag NW/graphene electrode in 2500 CV cycles [53]. (b) Schematic representation of the hybrid structure of tightly attached single layer graphene on welded Ag NWs after the sintering procedure [18]. (c) CV of the fabricated symmetric Ag NWs-GO supercapacitor at various scan rates [55].

3.1.3.2 Carbon Nanotubes

Lee et al. utilized bar coating method for the deposition of CNT-Ag NW hybrid coating on PET substrate at room temperature [57]. CNT-Ag NWs on PET were kept in 85 °C and 85% RH environment for 120 h and 240 h separately. Roughness of the Ag NWs after 240 h was considerably increased, while no decrease in conductivity was reported, as shown in Figure 3.4 (a). CNT-Ag NWs composite network also showed high mechanical durability with only a 1.6% increase in resistance upon 100 bending cycles, whereas ITO and bare Ag film experienced 34.9 % and 73.9 % increase in resistance, respectively. In another study, transparent stretchable heaters were fabricated using single-walled carbon nanotube (SWCNT) – Ag NWs composite films with improved mechanical stability. Spray coating method was used for the deposition of SWCNT-Ag NW suspension onto 150 % prestrained adhesive acrylic elastomer, which was released after the deposition. Decomposition of Ag NWs was effectively prevented with the use of SWCNTs under 250 °C for 3 h. In addition to that, under an applied potential of 12 V, SWCNT-Ag NW composite film successfully reached to 186.2 °C, as shown in Figure 3.4 (b) [58].

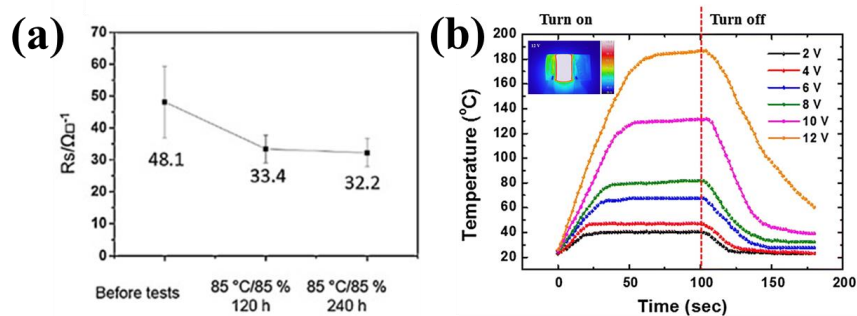


Figure 3.4 (a) Changes in sheet resistance with respect to testing conditions (85 °C and 85% RH environment) [57]. (b) Time dependent temperature profile of the SWCNT-Ag NW composite electrode as a function of a driving voltage (from 2 to 12 V) (inset shows the temperature distribution) [58].

3.1.3.3 Polymer Coating

PEDOT:PSS is one of the most widely used coating material due to its high conductivity and environmental stability upon. Moon et al. fabricated a flexible macro porous PEDOT:PSS/Ag NWs composite on polyurethane sponge. Both mechanical and electrical properties of the composite structure were found to get enhanced as well as the environmental stability upon 3000 charge-discharge cycles (capacitance retention of 85.8% at 5 A g^{-1}) and under bending deformation (electrical conductivity of $3.94 \times 10^{-4} \text{ S cm}^{-1}$ was preserved). An all solid-state supercapacitor device was fabricated [59]. In another study, transparent and flexible heaters (TFH) were fabricated. Composite films of Ag NWs/PEDOT:PSS and Ag NWs/PEDOT:PSS/ITO were fabricated. As shown in Figure 3.5 (a), among three TFHs, the mean temperature of Ag NWs is lowest at 9 V, which is correlated to the local junction failure in the Ag NW network [63]. Compared to bare Ag NW based TFHs, fabricated composite films showed improved mechanical stability and optical transparency with a higher maximum heating temperature compared to that of bare Ag NWs.

Due to its biocompatibility, high conductivity and mechanical properties, PPy was also utilized as a coating material. Yuksel et al. fabricated a Ag NW/PPy core-shell nanocomposites and investigated their supercapacitive properties as an electrode.

PPy layer protected the core Ag NWs and prevented them from getting oxidized and corroded. A specific capacitance of 509.0 F g^{-1} for the symmetric supercapacitors was reported [64].

In another study, a solution based method was used for the deposition of PANI onto Ag NWs. Ag NWs-PANI composite was developed to be used in an electrochemical sensor for the detection of 4-nitrophenol (4-NP). Due to the electrostatic interaction of aniline monomer and Ag NWs, PANI was coated onto Ag NW surface forming an irregular porous network (Figure 3.5 (b)). Also, the electrocatalytic performance of Ag NW-PANI structure on glassy carbon electrode (GCE) was better than that of bare Ag NWs/GCE. In the presence of 0.1 mM of 4-NP in 0.1 M phosphate-buffered saline (PBS) (pH 7.0). CV plots are provided in Figure 3.5 (c) where reduction of 4-NP was observed around -0.77 V for Ag NW-PANI electrode with a negative shift around 60 mV compared to Ag NWs electrode. This indicated the formation of a hydrogen bonding and electrostatic interaction with 4-NP in the presence of PANI [65]. Kumar et al. also studied the PANI coating to improve the surface properties of Ag NWs for their adaptation to optoelectronic devices. A polyaniline : polystyrene sulfonate (PANI:PSS) aqueous solution was deposited onto PET substrates via the Mayer rod coating. Ag NWs synthesized via polyol method with 40 nm diameter were coated onto the PANI : PSS layer. They were then mechanically pressed to each other. Pressing technique provided a slight increase in the transmittance and decrease in the sheet resistance of the network. Both surface roughness (less than 6.5 nm) and the gaps between Ag NWs in the network were found to decrease upon mechanical pressing [66].

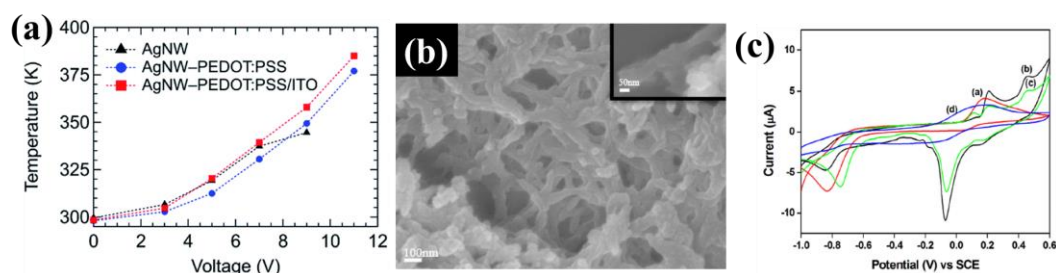


Figure 3.5 (a) Mean temperature of the pristine Ag NWs, Ag NWs-PEDOT:PSS, and Ag NWs-PEDOT:PSS/ITO TFHs with respect to bias voltage [63]. (b) SEM image of Ag NW-PANI composite (inset showing the lower magnification image) [65]. (c) Comparison of the CV results of GCE ((a) red curve), Ag NWs/GCE ((b) black curve), Ag NWs/PANI/GCE ((c) green curve), PANI/GCE ((d) blue curve) [65].

3.1.4 Metal Coating

Various metals such as Au [67],[68],[69], Pt [70], Ni [71], Fe [71] were used for the coating of Ag NWs. Au shell layer is highly preferred since it is an inert noble metal that is capable of improving the overall stability of the Ag NWs. Formation of Ag-Au core-shell structure was practiced via a solution base method by Lee et al.[67]. In Figure 3.6 (a), chloroauric acid (HAuCl_4) was the Au source for the galvanic replacement free synthesis of Ag-Au core-shell NWs. Ag NWs with a diameter of 30 nm were coated with a 5 nm thick Au shell layer as shown in Figure 3.6 (b). For Au deposition, an aqueous solution of Ag NWs was added into an aqueous dispersion of AA/PVP/NaOH, and then HAuCl_4 was injected into the reaction medium via a syringe pump. The chemical and electrochemical stability of the Ag NWs were found to get enhanced upon Au deposition due to higher reduction potential of Au compared to Ag. It was found that Ag-Au core-shell NW network remained intact under 22 °C and 45 % RH and 12.5 % hydrogen peroxide (H_2O_2) aqueous solution. After 50 cycles, CV curves of the Ag-Au core-shell NW networks converged to rectangular shape indicating the ideal capacitive behavior. Irreversible oxidation of Ag at around 0.45V was suppressed with the Au shell layer deposition and potential window was widened as 0-0.6 V. Moreover, Ag-Au core-shell NW based

supercapacitors showed an areal capacitance of $0.2099 \text{ mF cm}^{-2}$ and maintained their electrochemical stability up to a strain level of 60 %.

Ag-Au core-sheath NWs were synthesized via solution-phase method by Yang et al., where 2-3 atomic layers of Au was conformally deposited onto Ag NWs [69]. With the addition of NaOH, an alkaline solution of HAuCl_4 was prepared and Au(OH)_4^- was used as the Au source. Fabrication of Ag-Au core-sheath NWs was achieved under alkaline conditions with the use of ascorbic acid ($\text{C}_6\text{H}_8\text{O}_6$, AA) and Au(OH)_4^- . Various oxidants such as O_2 , H_2O_2 , and iron (III) nitrate ($\text{Fe(NO}_3)_3$) were used to highlight the importance of Au sheath for the enhanced stability of the NWs. Furthermore, for the fabrication of transparent and flexible conductors, Ag-Au core-sheath NWs were considered as a good alternative to replace bare Ag NWs.

As another noble metal, Pt was used as a protective layer for Ag NPs by Wojtyasiak et al. [72] potassium hexachloroplatinate(IV) (K_2PtCl_6) was used as a Pt source and galvanic replacement reactions took place between PtCl_4^{2-} ions and Ag seeds in the presence of AA leading to the formation of Ag-Pt core-shell nanoparticles.

Pt metal deposition onto Ag NWs was also studied by Shen et al. [70]. Ag NWs were grown on TiO_2 coated Si wafers via a thermal assisted photoreduction method. Instead of K_2PtCl_6 or chloroplatinic acid (H_2PtCl_6), which are the common Pt sources, disodium hexahydroxoplatinate ($\text{Na}_2\text{Pt(OH)}_6$) was chosen due to the smaller electronegativity of the OH^- group, which eased the reduction of Pt ions. Ag NWs were then added into the aqueous solution of $\text{Na}_2\text{Pt(OH)}_6$ and isothermally heated to reflux for the galvanic exchange between Ag and Pt to take place. A conformal Pt nanocrystal shell was formed on the Ag NWs.

Focusing on the poor electrochemical stability of the Ag NWs, in addition to the use of noble metals (Au, Pt through solution based routes), Park et al. demonstrated electrodeposition of a thin nanoshell of Ni and Fe metals onto Ag NW networks [71]. Both of the stretchable and transparent Ag-Ni and Ag-Fe core-shell NW networks on polyurethane acrylate (PUA) electrodes were found to be electrochemically stable in KOH electrolyte. A capacitance retention of 112 % was obtained after 1000 cycles

for Ag-Ni NWs since the core Ag NWs was protected against galvanic replacement reaction, as shown in Figure 3.6 (c). Working potential window for Ag-Ni NWs was 0-0.7 V. 50 cycles of CV in 1M KOH electrolyte are shown in the inset of Figure 3.6 (c), while bare Ag NWs experienced a rapid current drop at the 30th cycle within the potential window of 0-0.5 V. An asymmetric Ag-Ni/ Ag-Fe NWs supercapacitor was fabricated and operated in a potential window of 0-1.6 V. A capacitance retention of 92% and 91% upon 5000 cycles were obtained when it is released and stretched to 35% strain, respectively.

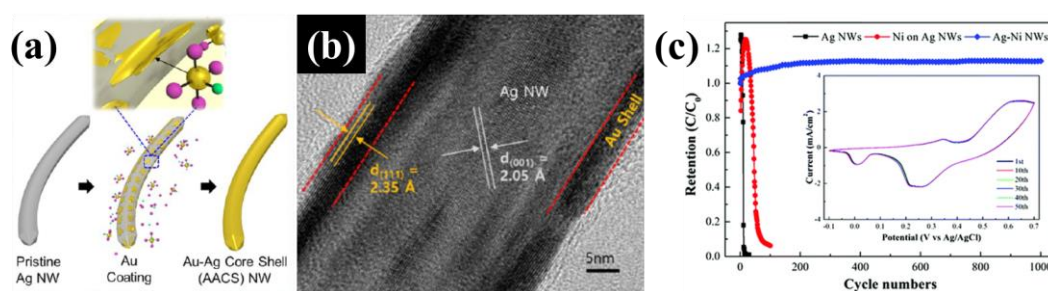


Figure 3.6 (a) Schematic representation of Ag-Au core-shell NWs fabrication. (b) TEM image of Ag-Au core-shell NWs [67]. (c) Comparison of capacitance retention percentage in 1 M KOH electrolyte for Ag NW/PUA and Ag-Ni core-shell NWs/PUA. (inset shows the CV curves of Ag-Ni NWs with the number of cycles) [71].

3.2 Mechanism of Solution Based Metal Coating

Deposition of a thin metal shell on NWs has many challenges since it is difficult to perform a galvanic replacement free coating. As an example, galvanic replacement reaction between Ag and Au salt (HAuCl_4), causes pits or voids in the NW structure if not avoided. Yang et al. studied the reaction route for galvanic replacement free, 0.6 nm thick, Au shell deposition on Ag nanocubes [73]. For the synthesis of Ag-Au core-shell NWs, AA was chosen as a reducing agent. Provided that the reaction medium was basic ($\text{pH}=11.02$), the reduction rate of HAuCl_4 by AA was higher than the galvanic reaction rate between Ag and HAuCl_4 . Hence a galvanic replacement-free synthesis was achieved. On the other hand, the galvanic reaction rate was higher causing hollow Ag-Au nanocubes in a reaction medium having a pH of 2.63. By

increasing the pH of the reaction medium, reduction power of AA was optimized and HAuCl₄ was reduced by AA before any galvanic reaction took place between HAuCl₄ and Ag nanocubes. Au atoms were uniformly deposited onto Ag nanocubes. It was concluded that the reduction of HAuCl₄ by AA in a reaction medium with a pH of 9.5 and above completely suppressed the galvanic reaction. When exposed to 2.3 % aqueous H₂O₂, Au-Ag core-shell nanocubes remained stable for 10 h, whereas bare Ag nanocubes were oxidized within only 3 min.

Another study conducted by Murshid et al. revealed the importance of slow addition of Au source into the reaction medium to lower the reduction potential of Au ions and to deposit a uniform gold shell [74]. Silver decahedral NPs (AgDe NPs) and pentagonal rod NPs (AgPR NPs) were synthesized via slow addition of HAuCl₄ to a reaction medium containing Ag NPs, citrate was used as charge stabilizer and polyvinylpyrrolidone (PVP) as steric stabilizer. When Au % (molar percentage of deposited Au relative to Ag precursor) was 10 %, galvanic replacement was minimized with an increase in chemical stability. In the case where Au % was less than 10 %, insufficient Au amount caused non-uniform deposition on the surface. Such an insufficiency also caused the dissolution of Ag in H₂O₂ solution. When Au % was more than 10 %, hollow Au-Ag NPs were formed due to galvanic replacement. In addition to that, they found out that using low concentration of HAuCl₄ and slow injection rate (12 h) prevented the formation of pits and voids. On the other hand, use of mild reducing agents and change in the pH of the reaction medium was not sufficient to avoid galvanic replacement reactions if high concentrations of Au and high injection rates were preferred. Fabricated Au@AgPR NPs were proved to be chemically stable in 0.5 M H₂O₂ solution for 30 days, while bare NPs dissolved only after several minutes.

In another study conducted by Yang et al. for the synthesis of Ag@Au core-sheath NWs, an alkaline condition with a pH around 11.0 was used to enhance the reduction power of AA [69]. As a result, reduction of Au³⁺ to Au prevented the galvanic replacement between Au³⁺ and Ag. However, it was stated that the complete prevention of galvanic reaction was not possible even under those conditions.

Therefore, reduction potential of the Au^{3+}/Au pair was lowered by replacing the Cl^- in AuCl_4^- with OH^- ions. This was achieved at pH values higher than 10.35 with the addition of sodium hydroxide (NaOH) to HAuCl_4 , where AuCl_4^- was transferred to $\text{Au}(\text{OH})_4^-$ and was used as Au source. As a result, low reduction potential of $\text{Au}(\text{OH})_4^-/\text{Au}$ and strong reducing power of AA in alkaline media suppressed the galvanic reaction between Au^{3+} and Ag. In addition to stability against oxidants such as O_2 and $\text{Fe}(\text{NO}_3)_3$, stability against H_2O_2 exposure was determined using UV-vis and TEM analysis both before and after the H_2O_2 treatment. For that purpose, Ag-Au core-shell NWs suspension was mixed with a H_2O_2 solution in 1:1 (v/v) ratio (final H_2O_2 concentration was 0.85 M). Thanks to the 1 nm thick Au shell decrease in localized surface plasmon resonance (LSPR) peak intensity was around 3 %, indicating no Ag dissolution during H_2O_2 treatment, whereas bare Ag NWs were etched after 1 h.

Ag-Au core-shell NWs were also synthesized by Lee et al. through a solution based process [67]. Aqueous solutions of AA and NaOH were introduced into the PVP solution one by one, followed by the addition of Ag NWs to the aqueous solution. An aqueous solution of HAuCl_4 was slowly injected into the reaction media via a syringe pump. A 5 nm thick Au shell was coated onto Ag NWs having a diameter of 30 nm (Figure 3.6 (b)). In 12.5 % H_2O_2 solution, bare Ag NWs were damaged and removed from the substrate surface in seconds. On the other hand, Ag-Au core-shell NWs remained stable under such a corrosive environment. In addition to chemical stability, electrochemical stability was also enhanced upon Au shell deposition. In the potential window of 0-0.6 V, pristine Ag NWs experienced an irreversible oxidation at around 0.45 V. On the other hand, in the same potential window, Ag-Au core-shell NWs operated up to 50 cycles. Under ambient conditions (22 °C and 45% RH) Ag-Au core-shell NW network preserved its conductivity for 4 weeks.

In addition to Ag-Au core-shell NWs, silver-platinum (Ag-Pt), core-shell NWs were fabricated by Shen et al. via thermal assisted photoreduction of Ag NWs on Si template and galvanic exchange between Ag and Pt ions [70]. Sodium hexahydroxyplatinate(IV) ($\text{Na}_2\text{Pt}(\text{OH})_6$) was used as the Pt source rather than

chloroplatinic acid (H_2PtCl_6). Due to the low electronegativity of the OH^- group (3.02) compared to Cl^- (3.16), Pt ions were reduced easily by the electrons formed with the oxidation of Ag. For the Pt shell deposition, dispersion of Ag NWs and $\text{Na}_2\text{Pt}(\text{OH})_6$ was refluxed at 100 °C, 170 °C, and 200 °C. During the reaction, diameter of the core Ag was found to decrease, while thickness of the Pt nanocrystal layer increased with the interface controlled galvanic deposition process. As shown in Figure 3.7 (a), boundaries of Pt nanocrystal formed microchannels which helped the transportation of Ag^+ at the interface to the Pt shell. Also, electrons moved to the conductive Pt shell and supported the reduction of Pt^{4+} on the outer surface of the shell.

Ag-Pt core-shell NPs were synthesized by Wojtysiak et al. via a seeded growth reaction with the use of AA to reduce PtCl_4^{2-} [72]. AA and K_2PtCl_4 were added to Ag seed containing medium. Ag-Pt core-shell nanoparticles were fabricated by the galvanic reaction between Ag seeds and PtCl_4^{2-} . It was stated that avoiding the oxidation of Ag to obtain a pinhole-free Pt layer was both dependent on the deposition of large amounts of Pt and use of AA.

A study conducted by Fu et al. stated the different synthesis routes for hollow porous nanoparticles (NPs) with Pt coating and Ag-Pt core-shell NPs. Hollow porous Ag-Pt alloy NPs having a Pt deposit were synthesized via controlled galvanic replacement reaction, which is shown in route A in Figure 3.7 (b). For both route A and B, AA, PVP, and K_2PtCl_4 was used; however, the main factor in the formation of Ag-Pt core-shell NPs was doubling the reducing agent (AA) amount to avoid the galvanic replacement reaction occurring between Ag and PtCl_4^{2-} . Completion of the reaction was assessed by the color change of the solution from brown to black [75].

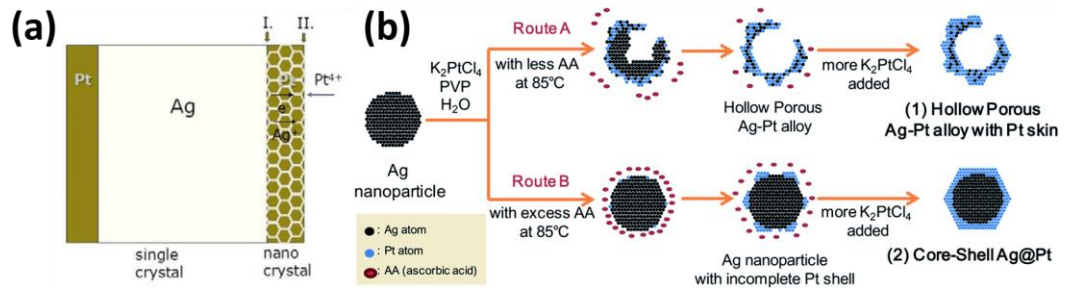


Figure 3.7 (a) Schematic illustration Ag-Pt core-shell formation by the galvanic replacement between Ag and Pt ions [70]. (b) Schematic illustration of different routes for the synthesis of hollow porous Ag-Pt alloy NPs with Pt skin and Ag-Pt core-shell NPs with Pt shell on Ag core [75].

CHAPTER 4

EXPERIMENTAL DETAILS

Chemicals with the details given below were used as purchased without further purification. Ethylene glycol (anhydrous, 99.8%), poly(vinylpyrrolidone) (PVP) (powder, average Mw ~ 55,000), silver nitrate (ACS reagent, $\geq 99.0\%$), sodium chloride (ACS reagent, $\geq 99.0\%$), L-Ascorbic acid (ACS reagent, $\geq 99.0\%$), chloroplatinic acid solution (8 wt% in H₂O), Gold(III) chloride hydrate (99.995 % trace metals basis), D-(+)-glucose monohydrate (anhydrous, 97.5–102.0 %), urea (BioReagent $\geq 98\%$), DL-lactic acid (90%), oxalic acid dihydrate (ACS reagent, $\geq 99\%$), acetone (ACS reagent, $\geq 99.5\%$), ethanol (absolute, $\geq 99.8\%$), nitric acid (ACS reagent, 70%) were purchased from Sigma-Aldrich. Sodium hydroxide (pellets pure, $\geq 99\%$) was purchased from Merck.

Prior to each experiment, all glassware and magnetic stirrers were cleaned. Initially, all was washed with Alconox detergent and rinsed with DI water. Magnetic stirrers were cleaned via ultrasonication in 10 % nitric acid-DI water solution followed by DI water rinsing. In the final step, all of the glassware and magnetic stirrers were ultrasonicated for 15 min with acetone, ethanol and DI water.

4.1 Fabrication of Nanowire Networks

4.1.1 Synthesis of Silver Nanowires

An improved solution-based polyol method, which was initially developed by Coskun et al. [7] was followed for the synthesis of the Ag NWs throughout this work. In this method, ethylene glycol (EG) was used both as the solvent and the reducing agent for the precursor. Silver nitrate (AgNO₃) was used as the Ag precursor. In

addition, poly(vinylpyrrolidone) (PVP) was introduced to the reaction medium as a capping agent for the directional growth of Ag seeds.

Two different solutions were prepared. One contained 0.45 M PVP ($M_w = 55\text{K g/mol}$) and 1 mM NaCl dissolved in 80 ml EG and other contained 0.12 M AgNO_3 dissolved in 40 ml EG. First, into a 250 ml round bottom flask 0.12 M AgNO_3 and 40 ml EG were added and the solution was stirred for 20 min at 1000 rpm until all the solid in the flask was dissolved. Next, a solution containing PVP and NaCl dissolved in 80 ml EG was stirred under 90 °C for 20 min at 1000 rpm in a 100 ml beaker. After all the solids were dissolved in EG and a clear solution was obtained, the solution was left to cool down to room temperature. The solution containing AgNO_3 in EG was placed into a silicon oil bath, which was preheated to 120 °C at 1000 rpm. Dropwise addition of the solution containing PVP and NaCl in EG was performed. Following the completion of addition a condenser was placed on top of the round bottom flask and a reflux system was initiated. Immediately after the placement of the condenser, the temperature of the silicon oil bath stirred at 1000 rpm was set at 160°C and the reaction continued for 80 min at this temperature.

In Figure 4.1 (a)-(d), the photographs of the different steps of the polyol synthesis are provided. At the first 30 min of the reaction, brown-red color appears corresponding to the process of the formation of Ag seeds. As the reaction was continued at 160°C with constant stirring in the 40th min gray-like color appears indicating the formation of Ag NWs.

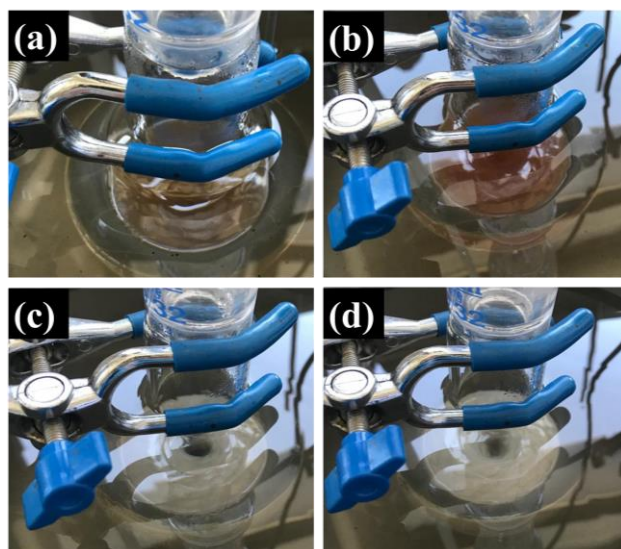


Figure 4.1 Photographs taken at the different stages of the polyol synthesis: (a) 1 min, (b) 30 min, (c) 40 min and (d) 80 min of the reaction.

Following the completion of the Ag NWs synthesis, Ag NWs were separated from the byproducts and excess components. First, a decantation process was followed, where the Ag NWs suspension was collected in a 250 ml beaker and left to settle for a few days. At this first stage of the purification process the separation of the Ag NWs, from Ag NPs, EG, and the excess amount of PVP was achieved. Further purification was continued by a multi-step centrifugation. First, to get rid of any residual organic substance, Ag NW suspension that was acquired at the decantation step was diluted at a 1:4 ratio with acetone. Centrifugation of diluted Ag NW suspension was performed under 7000 rpm for 3 min. Precipitate at the bottom of the centrifugation tube was then combined with ethanol and Ag NW-ethanol suspension was centrifuged two more times at 7000 rpm for 6 min. After centrifugation, Ag NWs were collected with ethanol into a 250 ml beaker. However, even after those initial decantation and centrifugation steps, there were Ag NPs still present in the ethanolic suspension. Therefore this suspension was subjected to a sedimentation process, where the Ag NPs were expected to precipitate while Ag NWs suspend in ethanol. Sedimentation was repeated until a suspension without a precipitate was obtained.

For further use, Ag NWs were also collected in DI water. Additional centrifugation with DI water at 7000 rpm for 10 min followed with a sedimentation procedure in DI water was performed for this purpose.

4.1.2 Fabrication of Silver Nanowire Networks

Purified Ag NWs, dispersed in ethanol was deposited onto glass or PET substrates via spray deposition method. In a typical spray deposition process, glass or PET substrates were placed on a hot plate arranged at a specific temperature that is compatible with both substrate and solvent, as shown in Figure 4.2 (a). Glass and PET substrates were cleaned beforehand through 15 min ultrasonication in acetone, ethanol and DI water. During spray deposition of NWs, vaporization of the solvent took place forming the random NW network. During this process, both pressure of the N₂ gas and the distance between the hot plate and the tip of the air brush were very important parameters.

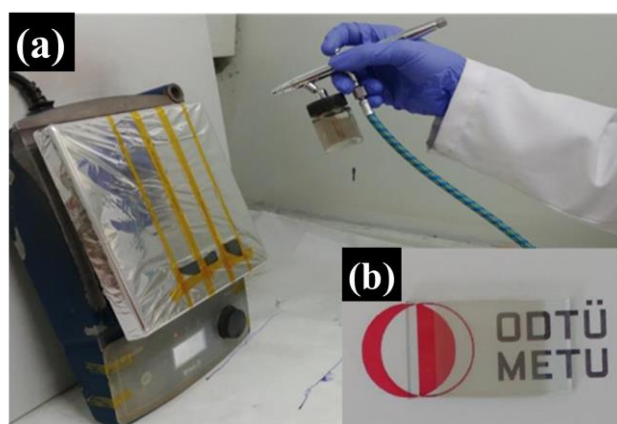
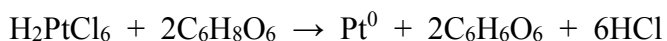


Figure 4.2 Photos showing the (a) spray deposition method of NWs and (b) spray deposited Ag NW networks on a glass substrate.

4.2 Fabrication of Silver-Platinum Core-Shell Nanowires

A solution based method was followed for the conformal platinum (Pt) shell coating onto Ag NWs based on the initial work by Stewart et al. [76]. During the synthesis, H_2PtCl_6 was used as the platinum source for the shell layer coating and AA was used as the reducing agent. In a 25 ml beaker, 5.5 ml of 1 M AA-DI water and 2 ml of 5 wt. % PVP-DI water solution was prepared. Following the complete dissolution of the components, a dropwise addition of 3.0 ml 0.5 mg/ml Ag NWs-DI water dispersion was performed. The dispersion was stirred at 500 rpm for 3 min at room temperature. After that 0.47 ml of 0.01 M chloroplatinic acid solution was added into the reaction medium. The reaction took place at room temperature under constant stirring at 500 rpm for 3 min. During the reaction with the addition of H_2PtCl_6 , the color of the dispersion gradually turned from grey to black. The major reaction for the Ag-Pt core-shell NWs fabrication was,



Purification of the Ag-Pt core-shell NWs from byproducts was achieved by multi-step centrifugation. First, the reaction suspension in DI water was centrifuged at 7000 rpm for 10 min. Following that, the precipitate at the bottom of the centrifugation tube was washed with DI water two times at 7000 rpm for 10 min. Lastly, centrifugation with ethanol was performed both to get rid of any excess PVP or AA left and to collect the Ag-Pt core-shell NWs at the ethanol phase. A schematic representation of the fabrication of Ag-Pt core-shell NWs is shown in Figure 4.3 (a). Corresponding SEM images of Ag NWs and Ag-Pt core-shell NWs are provided in Figure 4.3 (b) and Figure 4.3 (c), respectively (insets showing the schematics of Ag NW and Ag-Pt core-shell NWs).

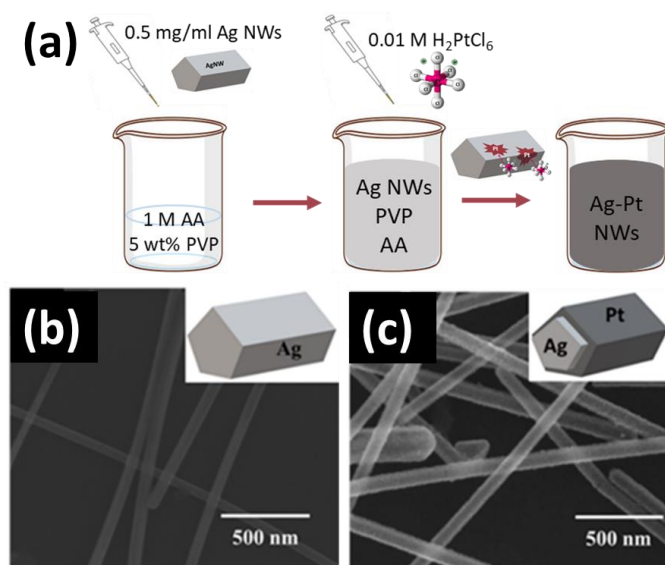


Figure 4.3 (a) Schematic representation of the fabrication of Ag-Pt core-shell NWs. SEM image of (b) Ag NWs (inset showing a schematic of Ag NW) and (c) Ag-Pt core-shell NWs (inset showing a schematic of Ag-Pt NW).

4.3 Nanowire Characterization Methods

4.3.1 Scanning Electron Microscopy (SEM)

Field emission scanning microscopy (FE-SEM) (Nova NanoSEM 430) operated at 20 kV was used to examine the fabricated NWs. Ag NWs and Ag-Pt core-shell NWs were dried on Si wafers and used for the SEM analysis. Prepared Si wafers were fixed onto the SEM holders via double-sided conductive carbon tape. No additional coating was used for sample preparation.

4.3.2 Transmission Electron Microscopy (TEM)

For the atomic scale morphological analysis of the synthesized Ag NWs and Ag-Pt core-shell NWs, transmission electron microscopy (TEM) was used at an operating voltage of 200 kV in high-resolution mode (HR-TEM) (JEOL JEM-2100F UHR/HRP 200 Kv). TEM samples were prepared via drop casting of ethanolic NW

suspension onto holey carbon coated 400 mesh copper grids. Lattice fringes were determined and measured using GATAN software.

4.3.3 X-Ray Diffraction Analysis (XRD)

For the crystal structure analysis of NWs, X-Ray diffraction method was used. A Rigaku D/Max-2000 diffractometer with Cu K α radiation operating at 40 kV was used. Patterns were collected within 2 Θ range of 20-80° at a scan rate of 0.5 °/min.

4.3.4 X-Ray Photoelectron Spectroscopy (XPS)

X-Ray photoelectron spectroscopy (XPS) analysis was performed for the further characterization of NWs. PHI 5000 versaprobe (XPS) spectrometer was used with Al-monochromatic X-rays and operation power of ion gun at 0.5-5 keV. OriginPro 2018 software was used for XPS peak fitting where a Gaussian function was used to fit for a baseline correction. Carbon (1s) line at 284.8 eV was chosen as a reference and was used for charge correction.

4.3.5 pH Measurements

pH measurements during the synthesis of core-shell NWs were conducted using a scientific Orion 3-star conductivity meter. Before and after each pH measurement, the pH probe was rinsed with DI water and was carefully dried with a lint free cleanroom tissue. pH probe was kept in its storage solution when not in use.

4.4 Results

4.4.1 Silver Nanowires

HR-TEM image of a Ag NW is shown in Figure 4.4 (a), where perfect crystallinity of the Ag NW was apparent. Presence of a thin layer of PVP (3-5 nm) was also evident. The morphology of the fabricated Ag NWs was also examined via SEM. In Figure 4.4 (a) and (b) by-product free, purified Ag NWs were presented with a calculated mean diameter and length of 52.4 ± 3.8 nm and 9.5 ± 2.4 μm , respectively. 15 individual Ag NWs were randomly selected for the diameter and length measurements. Figure 4.4 (c) shows the XRD pattern of the fabricated Ag NWs to determine the phase purity and crystallinity. The diffraction angles of 38.18° , 44.80° and 64.56° correspond to (111), (200), and (220) planes of face-centered cubic (FCC) crystal structure of Ag, respectively, (JCPDS Card no: 04-0783).

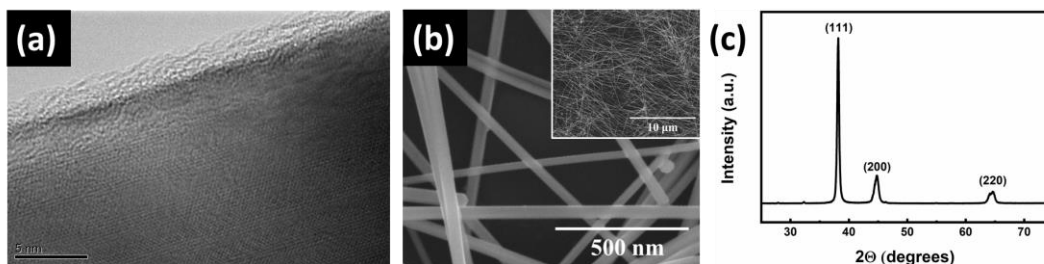


Figure 4.4 (a) HR-TEM image of an individual Ag NW. (b) SEM images and (c) XRD pattern of Ag NWs fabricated via polyol method (JCPDS Card no: 04-0783).

4.4.1.1 Silver-Platinum Core-Shell Nanowires

The average diameter of Ag-Pt core-shell NWs was calculated as 83.5 ± 4.5 nm from the SEM images shown in Figure 4.5 (a). Compared to the average diameter of bare Ag NWs (52.4 ± 3.8 nm), an increase in diameter indicated the deposition of the Pt shell layer. As shown in Figure 4.5 (a), a galvanic replacement free shell layer deposition was achieved. TEM image of an individual Ag-Pt core-shell NW is provided in Figure 4.5 (b). Different contrast within the TEM image of the NW

verified the core-shell NW structure, where Ag core and Pt shell appeared as bright and dark regions, respectively. From the HR-TEM images shown in Figure 4.5 (c) it was found that the lattice fringes with a spacing of 0.24 nm and 0.23 nm were associated with the (111) planes of Ag and Pt in the core and shell layers, respectively. However, it was inevitable to completely avoid the galvanic reactions that took place at the initial stages of the synthesis of Ag-Pt core-shell NWs. Therefore, lattice fringe spacing value of the interface region was found to be 0.24 nm, which can be associated to the formation of a (2-3 nm thick) face centered cubic (FCC) Ag-Pt solid solution at the interface due to the inevitable galvanic reactions between Ag core and Pt shell layers.

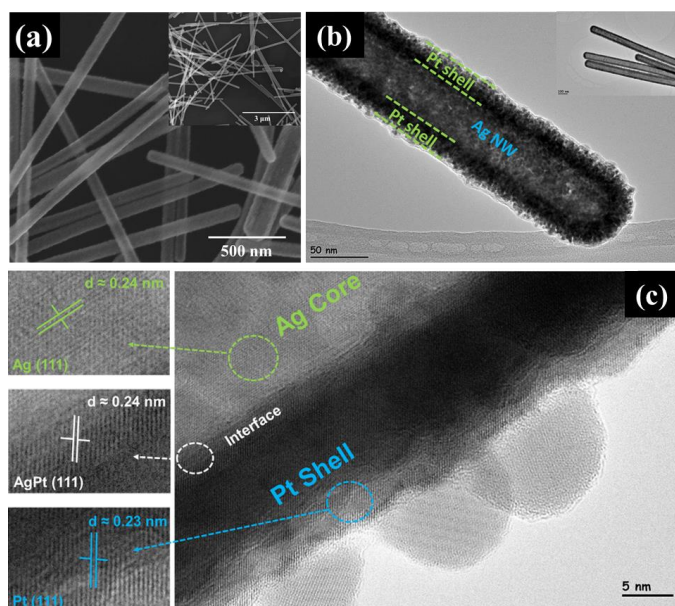


Figure 4.5 (a) SEM image (insets shows lower magnification SEM image) and (b) HAADF-STEM image of Ag-Pt core-shell NWs (insets shows lower magnification TEM image). (c) HR-TEM image of a Ag-Pt core-shell NW with corresponding lattice fringes of Ag (green), interface of Ag and Pt (white) and Pt (blue).

Figure 4.6 (a) shows the XRD pattern of Ag-Pt core-shell NWs. Diffraction angles of 38.82° , 45.14° , and 65.72° were assigned to be (111), (200), and (220) planes, respectively, and showed that Ag-Pt core-shell NWs has the FCC structure. Comparison of the XRD patterns of bare Ag NWs and Ag-Pt core-shell NWs is given in Figure 4.6 (b). Weaker diffraction of Pt from the shell layer compared to the

stronger diffraction of Ag from the core region caused the overlapping of weak Pt peaks with strong Ag peaks as shown in the XRD pattern for Ag-Pt core-shell NWs. Hence, broad peaks were observed for Ag-Pt rather than individual Ag and Pt peaks [77]. Lattice fringe spacing values for Ag core 0.24 nm and Pt shell 0.23 nm was also supported with the XRD results, which were associated with the (111) planes of Ag (0.2359 nm, PDF card 00-004-0783) and (111) planes of Pt (0.2326 nm, PDF card 01-087-0644).

X-Ray photoelectron spectroscopy (XPS) analysis was conducted to determine the chemical states of the elements in the fabricated Ag-Pt core-shell NWs. XPS deconvoluted spectra of Ag 3d and Pt 4f in Figure 4.6 (c) and (d), respectively, shows the peak positions and curve fits. The two prominent peaks of Ag corresponding to $3d_{5/2}$ and $3d_{3/2}$ were observed at 365.1 eV and 371.1 eV, respectively. Compared to the 3d orbitals of metallic Ag^0 at 368.3 eV and 374.3 eV, peaks are slightly shifted to lower binding energy values [78]. Such a decrease in the binding energies indicates that a change in the chemical environment of the Ag atoms occurred due to the interaction of Ag atoms with the N or O in the polyvinyl skeleton of the PVP [79]. Two shoulder peaks at 366.6 eV and 372.1 eV corresponds to silver at +1 state (Ag^+). Prominent peaks observed at 68.3 eV and 71.5 in Figure 4.6 (d) corresponds to the $4f_{7/2}$ and $4f_{5/2}$ orbit states of metallic Pt. Two shoulder peaks at 69.7 eV and 72.8 eV also correspond to the $4f_{7/2}$ and $4f_{5/2}$ of Pt at +2 state (Pt^{2+}), due to the contact with air during the sample preparation [80]. Shifts to higher binding energies are due to the electronegativity difference between cation and metal. With the formation of cations, due to the lowered electron number shielding of the nucleus was reduced, which causes an increase in binding energies [81]. Compared to bulk Pt binding energies at 71.58 and 74.90 eV for $4f_{7/2}$ and $4f_{5/2}$ orbitals, negative shifts in metallic Pt peaks indicate that there is tensile stress caused by Ag, which also proves the presence of distinct Ag core and Pt shell [75]. The presence of Ag^+ and Pt^{2+} peaks can also support the formation of a Ag-Pt solid solution at the interface region.

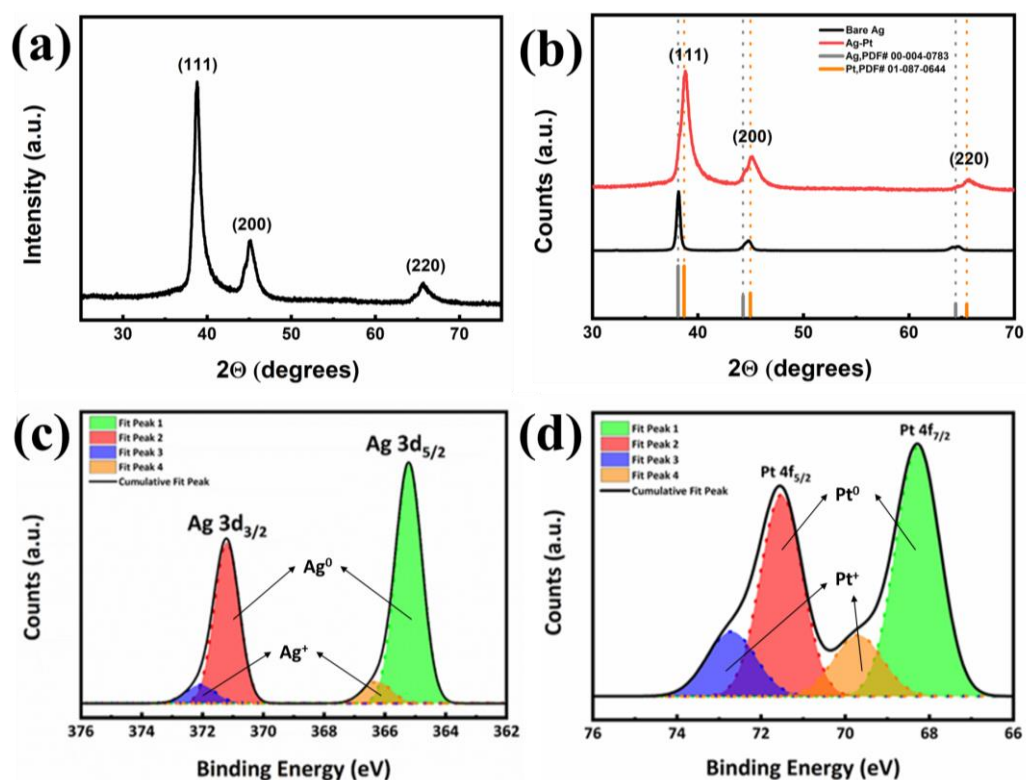


Figure 4.6 (a) XRD pattern of Ag-Pt core-shell NWs (JCPDS Card no: 04-0802), (b) Comparison of XRD patterns of bare Ag NWs (black) and Ag-Pt core-shell NWs (red). Fitted XPS spectra for (c) Ag 3d and (d) Pt 4f.

SEM-EDS maps obtained from the SEM image in Figure 4.7 (a) are given in Figure 4.7 (b) and (c) for Ag and Pt, respectively. Existence of a sufficient Pt deposition on the Ag NW surface was also determined by the EDS mapping method. In addition, EDS analysis revealed that the relative atomic percentages of Ag and Pt were 78 % and 22 %, respectively, which also showed the presence of Pt on Ag NW surface.

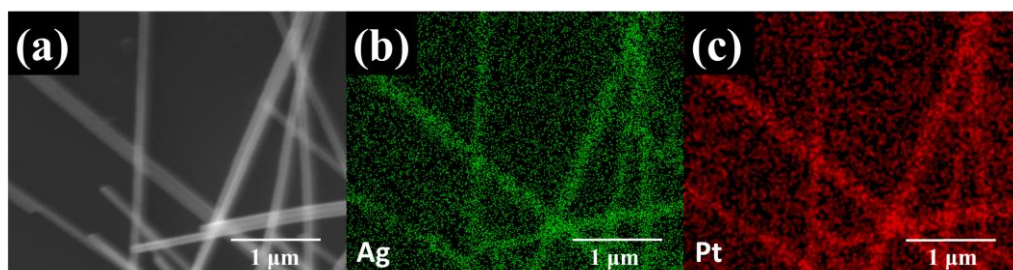


Figure 4.7 (a) SEM image of Ag-Pt core-shell NWs and correspondingly EDS maps for (b) Ag and (c) Pt.

CHAPTER 5

SILVER-PLATINUM CORE-SHELL NANOWIRE NETWORK BASED HYDROGEN PEROXIDE SENSORS

5.1 Introduction

Electrochemical sensors are one of the subclasses of chemical sensors, which are used for the detection of various analytes [82]. H_2O_2 has an important role in many fields such as medicine, pharmacy, food, agriculture cosmetics industries. It is used as a sterilizer, paper bleach and also it is a residual component of food disinfection and a waste product of many industrial processes. It also has the potential to react with the targets in the cell and can thus cause various diseases [83],[84], [85]. Therefore, various methods are developed to detect H_2O_2 . The main methods are spectrophotometry, chromatography, titration, fluorometry and electrochemical techniques [84]. Due to their high sensitivity and selectivity, electrochemical sensors have been studied and used for the successful detection of hydrogen peroxide (H_2O_2) [83].

5.2 Working Principle

Sensors are analytical devices that convert biological, chemical or physical changes into measurable analytical signals. Different sensors are fabricated for different analytes to be detected. A sensor should consist of a recognition element in contact with a transducer (electrode) and a signal processor. A schematic of a simple detector is provided in Figure 5.1. The recognition element minimizes the possible interferences from other components and selectively responds to only a specific analyte or analyte group. Transducer transfers a chemical or biological signal into an analytical signal by transferring the electrical charge produced by a reaction. The

final component of a sensor, which is the signal processor or read-out system collects and amplifies the signal to be displayed [82].

In the sensing layer of an amperometric sensor, redox species are oxidized or reduced on the surface of the transducer. A measurable change in current is generated through the electrode and displayed via the signal processor [86]. An ideal biosensor should hold high sensitivity and selectivity towards the substrate together with fast response, low detection limit in a wide linear range, high stability, reproducibility, long lifetime and ease in fabrication [82]. Considering those criteria, fast electron transfer from the recognition element to the electrode is very important for achieving high sensitivity and fast response [86].

In the amperometric measurements, electrochemical oxidation or reduction of the substrate generates a current, which is carefully monitored with respect to time; meanwhile potential between the working electrode (WE, sensor electrode) and reference electrode (RE) is kept constant. During the amperometric measurements, the potential is set to a specific value and analytes are introduced into the system. As the concentration of the analyte changes, the current response of the sensor also changes [82].

The use of nanostructured materials such as nanoparticles, nanowires or nanorods, and nanopores can improve the sensitivity of the sensor. Due to their large surface to volume ratio, nanomaterials can enhance and prolong the entrapment of the analyte. The short distance between analyte and surface of the electrode promotes the electron transfer rate, which is also beneficial for the detection of low amount samples [84], [82], [87].

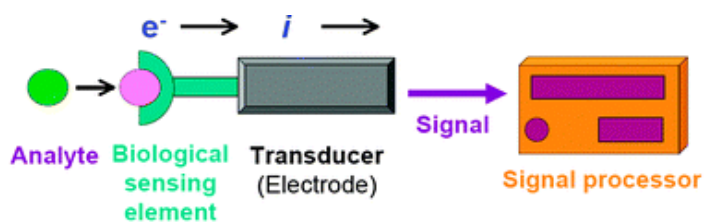


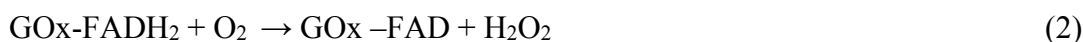
Figure 5.1 Schematic showing the components and working principle of a biosensor [82].

5.3 Types of Amperometric Sensors

5.3.1 Enzyme Based Sensors

Enzymes are used as recognition elements for the fabrication of enzyme-based sensors, also named as biosensors, due to their analyte selectivity and high biocatalytic activity. Some of the most known examples of biosensors are commercial blood glucose detection devices. Such biosensors have simple designs via inexpensive production techniques. Enzymes are used for the detection of a very specific individual biological substance. Their very complex molecular structure enables the specific detection of substances in complex environments. In this concept, effective interaction between enzyme and substrate depends on the successful immobilization of the enzyme, which prevents the enzyme to diffuse out of the biosensor [88]. Physical adsorption, covalent bonding or enzyme entrapment can be followed for the immobilization of enzymes [89], [90]. For a biosensor, to be able to observe the small variations in the current response, storage and operation stability of the enzyme is very important. Therefore, pH, temperature, and stirring parameters should be carefully selected and monitored. In the amperometric measurements of biosensors, oxidation/reduction potentials are specific to the analyte to be detected. Periodical renewal of enzymes is necessary for biosensors, since enzymes lose their activity and denaturalize after repeated usage [82].

One of the most frequently used enzyme is glucose oxidase (GOx), which is used for the fabrication of glucose biosensors. Due to its high specificity toward β -D-glucose below reactions occur as also shown in Figure 5.2.



Falvin group (FAD) in the GOx reacts with glucose and reduces to GOx-FADH₂ as in Reaction (1). Due to the presence of dissolved oxygen, GOx-FADH₂ is oxidized and regenerates both GOx-FADH₂ and H₂O₂. Following that, oxidation of H₂O₂ takes place on the surface of the WE and two electrons are transferred to the WE and cause a current response [82],[91]. A schematic of a glucose biosensor is given in Figure 5.2 representing a nanocomposite electrode based on hydroxyapatite (HAp) nanorods on reduced graphene oxide (rGO) and GOx on a GCE.



Figure 5.2 Schematic of the sensing mechanism of glucose biosensor based on (rGO/Hap/GOx) nanocomposite modified GCE [91].

An amperometric glucose biosensor was fabricated by Wang et al. using Ag NWs, chitosan (CS), and GOx on a GCE (GOx-CS/Ag NWs/GCE). Making use of its biocompatibility and high film-forming ability and mechanical strength chitosan was used as an immobilization matrix for GOx. At an applied potential of -0.15 V, the linear range of the biosensor was from 10 μ M to 0.8 mM and the detection limit was 2.83 μ M (S/N=3). The current response of the biosensor decreased to 7 % of its initial value after 10 days of storage at 4 $^{\circ}$ C. In addition to the large surface-to-

volume ratio, the long-term stability of the biosensor was related to the high mechanical strength and biocompatibility provided with the use of chitosan [92].

Ag NWs/rGO composite was fabricated by Li et al. for the utilization of a biosensor that detects ascorbic acid (AA), dopamine (DA) and uric acid (UA) [56]. The use of Ag NWs as nanospacers provided conductive pathways for electron conduction between rGO layers and created more catalytic sites for the analytes to be oxidized. Linear sweep voltammetry (LSV) was used for the simultaneous determination of AA, DA and UA. When compared to Ag NWs/rGO nanocomposite, bare Ag NWs on screen-printed carbon electrode (SPCE) were unable to distinguish the three different analytes and resulted in a low broad anodic peak current (Figure 5.3 (a)). Limit of detection (LOD) of Ag NWs/rGO/SPCE for AA, DA, UA was 0.81, 0.26 and 0.30 mM, respectively. Amperometric measurements were performed at applied potentials of 0.02, 0.2, and 0.33 V (vs. Ag/AgCl) for AA, DA and UA, respectively. Storage stability of the biosensor was also examined by keeping the sensor at 10 °C after each amperometric measurement for 10 days. A 6.18 % decrease in maximum peak current change was recorded for AA. Reproducibility was examined based on the current response measurements conducted on six independent sensors. Low relative standard deviation (RSD) was obtained as 3.24 % for AA, 2.16 % for UA and 2.21 % for DA indicating promising reproducibility of the fabricated biosensor.

H₂O₂ sensor and glucose biosensors were fabricated using Ag NWs synthesized by polyol process by Yang et al. [83]. PVP was indicated as a protecting agent for Ag NWs and PVP-Ag NWs modified GCE was used as a biosensor. GOx was immobilized onto PVP-AgNWs/GCE and the fabricated sensor had a sensitivity of 15.86 $\mu\text{A mM}^{-1}\text{cm}^{-2}$ and linear range from 1.5 to 6.5 mM ($R=0.998$) for glucose detection in human blood serum. In contrast to the enzymeless H₂O₂ sensor during the long-term stability tests under 4°C storage condition, the current response of the biosensor was decreased by 19% of the initial response, which corresponds to the loss of enzyme activity during 5 days of storage (Figure 5.3 (b)).

In another study gold nanowires (Au NWs) were fabricated through electrodeposition method using nanopore polycarbonate (PC) membranes. Glucose biosensor was fabricated thanks to the ease in adsorption of GOx onto the large surface area of the biocompatible Au NWs structure. For the fabrication of enzyme functionalized Au NWs, NWs were first dispersed in GOx solution overnight (at 4 °C) followed by their dispersion in chitosan solution. Amperometric measurements were conducted at an applied potential of -0.2 V (vs. saturated calomel electrode (SCE)) in pH 6.98 phosphate buffer as shown in Figure 5.3 (c). Glucose detection was performed at a linear range of 10^{-5} to 2×10^{-2} M with a 5×10^{-6} M detection limit. Biocompatibility of Au NWs and chitosan in addition to the good adhesion ability of chitosan provided a better immobilization of the enzyme. Therefore, after one month of storage at 4 °C, the current response of the biosensor maintained 85 % of its initial value [93].

Au-Ag core-shell nanorods (Au-Ag NRs) were synthesized through a seed mediated growth method. For the fabrication of a biosensor, GOx was immobilized onto Au-Ag NRs, which were casted on GCE and a chitosan solution was dropped onto the GOx to prevent the enzyme leaching. The sensitivity of the biosensor was $34.29 \mu\text{A mM}^{-1}\text{cm}^{-2}$, with a linear range of 2-12 mM. 4.1 % RSD of the current response of 6 different measurements showed the repeatability of the biosensor. After 7 days of storage at 4 °C, the current response decreased 14.69 % of its initial value, which was correlated with the loss of enzyme activity during the storage period. Selectivity of the biosensor, shown in Figure 5.3 (d) was monitored via the introduction of different interferences such as AA, DA and UA during the amperometric measurements of glucose, which yielded promising results [94].

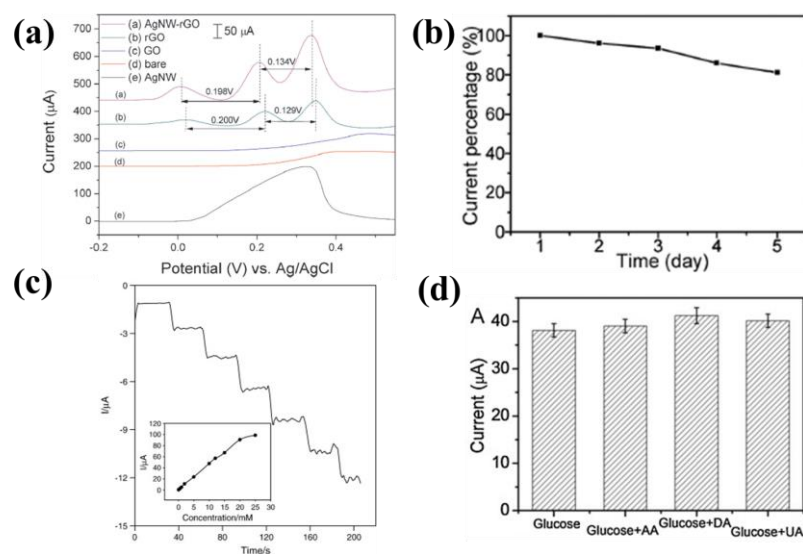


Figure 5.3 (a) LSV curves for bare SPCE (d) and modified SPCEs (with Ag NWs/rGO (a), rGO (b), GO (c), Ag NW (e)), (b) The amperometric current responses of the GOD/PVP-AgNWs/GCE in PBS solution (pH 7.4) to 3 mM glucose at a scan rate of 50 mV s^{-1} [83]. (c) Amperometric measurement of the biosensor based on Au NWs at an applied potential of -0.2 V (vs. SCE) for successive addition of 0.5 mM glucose. Inset showing the calibration curve [93]. (d) Comparison of the current responses of Au-Ag NRs based biosensors relative to the addition of 5 mM glucose, and 5 mM glucose in the presence of 0.5 mM AA, DA, UA in O_2 saturated (pH 7.4) 0.2 M PBS [94].

5.3.2 Enzymeless Sensors

Due to the short lifetime of enzyme based biosensors because of the enzyme denaturation with temperature and pH values, non-enzymatic sensors are receiving attention for the determination of H_2O_2 with high sensitivity, long-term stability and pH-independent fast response [85]. In addition, different compounds may be oxidized at similar applied potentials and decrease the selectivity of the biosensor. Detection of H_2O_2 is important since it is used in various fields such as food processing, clinical sterilizations, paper bleaching, pharmaceutical products and cosmetics [95]. In this regard, nanomaterial based enzymeless electrodes are designed for creating an enzyme-mimetic behavior for the electrochemical detection of H_2O_2 . Due to their high conductivity, large surface to volume ratio, and effective

electrical signal transmission, nanorods and nanowires are considered as one of the promising candidates for H₂O₂ sensor applications [84].

Various kinds of nanostructured electrode materials have been used for the fabrication of enzymless H₂O₂ sensors. Some of those nanostructures are based on carbonaceous materials, polymers, and metal NPs / NWs and their combinations [95], [96], [97], [98], [99], [85], [100]. Among them, noble metal based nanostructured electrodes such as Pd, Pt, Ag and Au are highly used for the determination of H₂O₂ due to their high electrocatalytic activity. They can catalyze the redox process of different compounds due to their large surface area, high conductivity and surface chemistry. In addition to the single component noble metal nanostructures, multi component structures such as core-shell, alloys or a combination of those two can greatly enhance the activity and stability of the electrode materials [101].

1D metallic NWs show high electrocatalytic performance for the reduction of H₂O₂ due to their fast reaction kinetics as a result of their large surface to volume ratio and fast electrical signal transmission due to their high conductivity [84]. NW fabrication parameters are also important since the morphological structure and NW dimensions play a critical role. Fast electron diffusion and charge transport can be achieved for NWs with smaller diameters and higher lengths [85].

Depending on the electrode potential, in general, H₂O₂ can be reduced to H₂O (H₂O₂ reduction reaction), E⁰=1.76 V, or can be oxidized to O₂ (H₂O₂ oxidation reaction), E⁰= 0.695 V [102]. According to Jia et al., high applied potentials results in high sensitivity and fast current response during the detection of H₂O₂. However, attention should be paid while working under high applied potentials to eliminate the oxidation of interferences in real samples [103]. Under applied voltage, electrochemical reaction occurring on the electrocatalytic surface of Pt during the H₂O₂ oxidation is as shown in Reaction (4); [104]



A H₂O₂ sensor composed of a heterostructure of Pt NPs and carbon nanofibers (CNFs) on a glassy carbon electrode (GCE) was fabricated by Yang et al. [105]. Under an applied voltage of -0.2 V (vs. Ag/AgCl), sensor exhibited a linear behavior in the concentration range of 5 μM to 15 mM with a detection limit of 1.7 μM (S/N=3). In addition to the presence of Pt NP catalyst, fast catalytic oxidation of H₂O₂ was enhanced by the conductive and porous CNFs matrix, which provided better immobilization of Pt NPs and fast diffusion of molecules.

In another study, for the fabrication of a H₂O₂ sensor, a GCE was modified with a stable poly-melamine layer via electropolymerization method and Pt NPs were electrodeposited onto the modified GCE. With the synergized effect of the conductive film and Pt NP catalyst, electrocatalytic activity of Poly-melamine/Pt NPs/GCE structure provided the reduction of H₂O₂. Under 0.08 V (vs. Ag/AgCl) applied potential, a linear range of 5 μM to 1650 μM, with a detection limit of 0.65 μM (S/N=3) was achieved. Interference free detection of H₂O₂ with long term stability was also provided. When stored in PBS for two weeks at 4 °C, the sensor retained 96.5 % of its initial response. Promising reproducibility was also revealed by the conductivity measurements on 5 different sensors, with a relative standard deviation (RSD) of only 1.9 % [106].

Taking advantage of the high electrocatalytic performance of 1D nanostructures, for the detection of H₂O₂, Ag NWs were synthesized via polyol process by Yang et al. [83]. PVP was used as a protecting agent for Ag NWs and the H₂O₂ sensor consist of PVP-AgNWs modified on GCE had a linear range and detection limit of 20 μM-3.62 mM (R=0.998) and 2.3 μM, respectively (S/N=3). Amperometric measurements were conducted in N₂-saturated 0.2 M PBS (pH 6.5) under an applied potential of -0.3 V. Thanks to the low operating voltage of the sensor, no interference was observed related to the other possible electroactive substances. The current response only decreased to 8.4 % of its initial value after 7 days of storage in contrast to the glucose biosensor fabricated in the same study (decreased by 19% of the initial response after 5 days, in Figure 5.3 (b))

Different than the polyol process, Ag NW array was fabricated by electrodeposition of Ag into the nanopores of anodic aluminum oxide (AAO) template. At an applied potential of -0.2 V (vs. SCE), H₂O₂ determination was achieved with a sensitivity of 0.0266 $\mu\text{A } \mu\text{M}^{-1}\text{cm}^{-2}$ in the linear range from 0.1 to 3.1 mM with a detection limit of 29.2 μM . Low noise level measurements are shown in Figure 5.4 (a). These were obtained when low concentrations of H₂O₂ (0.01, 0.1 mM) were added to PBS during amperometric measurements. When higher concentration of H₂O₂ (3.26 mM) was added, a noisy current response was observed as shown in Figure 5.4 (b) in addition to the nonlinear current vs time graph as the successive H₂O₂ addition continued. As shown in Figure 5.4 (c), after 42 days of storage, linear relationship was maintained between peak current density and concentration of H₂O₂. Sensitivity of the sensor increased from 0.0215 to 0.0329 $\mu\text{A } \mu\text{M}^{-1}\text{cm}^{-2}$ from day 14 to 42 due to the changes in specific surface area of the electrode. Long term stability of the sensor was also related to the enzyme-less nature of the prepared sensor, since there was no denaturation of the sensor material [84].

H₂O₂ detection with fast response and high sensitivity was achieved at low applied potential with the use of Au NWs. Au NWs were dispersed in a chitosan solution and were coated onto GCE surface. To determine the active surface area of the electrodes Randles-Sevcik equation was used in the cyclic voltammograms (CVs) of both bare and Au NW, modified GCEs in 20 mM K₃Fe(CN)₆ in 0.2 M KCl at 100 mv/s scan rate. The electroactive surface area of the Au NW modified GCE was found to be 2.5 times higher than that of bare GCE as provided in Figure 5.4 (d). The high electrochemical response of the electrode was related to the high electroactive surface area, high catalytic activity, and high electrical conductivity of the Au NWs [93].

In another study, high catalytic activity toward H₂O₂ reduction of Ag nanomaterials was combined with high biocompatibility of Au by Yang et al. [94] Au-Ag core-shell nanorods (NRs) was drop casted onto GCE for the detection of H₂O₂. Amperometric measurements were performed at a low applied potential of -0.3 V to prevent the co-existing electroactive substances to interfere with the H₂O₂ reduction.

Successive addition of 1.0 mM H₂O₂ into 0.2 M PBS (pH 6.5) was performed under constant stirring. Response time of the electrode was less than 2s, a wide linear range of 0.02-7.02 mM was obtained with a lower detection limit of 0.67 μM (S/N=3) than electrodes based on Ag NWs (2.3 μM) [83], (29.2 μM) [84], Ag-C-Ag core-shell nanospheres (23 μM) [107], Pt nanoparticle on carbon nanofiber (1.7 μM) [105], Au-Pt alloy NWs (1.5 μM) [108] due to the enhanced electrocatalytic activity of the bimetallic structure.

Thanks to high stability, increased functionality, and low consumption of the core material, core-shell NP structures were used. Au-C-Pt core-double shell structure was synthesized and used as an enzymeless electrode material on GCE for the detection of H₂O₂. Au, C, and Pt were chosen due to their excellent electronic and catalytic properties and high stability. At 0 V (vs. Ag/AgCl) applied potential sensor showed two linear ranges from 9.0 μM to 1.86 mM and 1.86 to 7.11 mM with a sensitivity of 144.7 μA μM⁻¹cm⁻² and 80.1 μA μM⁻¹cm⁻², respectively. As shown in Figure 5.4 (e) current response of the sensor increases with an increase in the molarity of the H₂O₂. The detection limit was calculated as 0.13 μM (S/N=3). 30 days storage at room temperature resulted in only an 8 % decrease in the current response to 1.0 mM H₂O₂ addition. RSD of 5 independent sensors was 4.3 % indicating high stability and reproducibility of the sensor. Noteworthy selectivity of the sensor was also determined by adding interferences such as glucose (GL), DA, UA, AA after the addition of H₂O₂ during the amperometric measurements as presented in Figure 5.4 (f) [109].

Another core-shell structure of Ag-C-Ag nanospheres having a trilaminar core-shell structure was also utilized for the detection of H₂O₂. The sensor had a wide linear range of 70 μM - 10 mM and a detection limit of 23 μM (S/N=3). Ag-C-Ag/GCE sensor was stored at 4 °C and only 4% of the initial current was lost to 1.0 mM H₂O₂ detection after 21 days. RSD of 5 independent electrodes was found to be 1.8% and RSD of an electrode response to 5 different measurements of 1.0 mM H₂O₂ detection was 1.3 % [107].

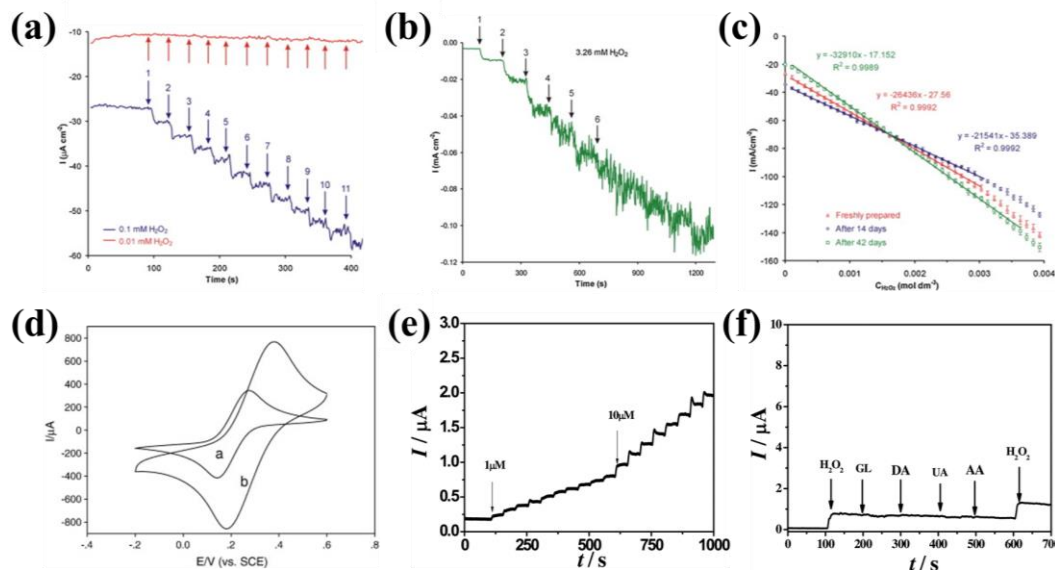


Figure 5.4 Amperometric response of the Ag NW array sensor to the addition of (a) 0.01 mM (red line) and 0.1 mM (blue line) (b) 3.26 mM H_2O_2 in the 0.1 M PBS solution (pH 7.4) under the applied potential of -0.2 V vs. SCE. (c) Calibration curves for the freshly prepared and 14 and 42 days stored Ag NW array based H_2O_2 sensors [84]. (d) Electroactive surface area by CVs at 100 mV/s scan rate in 0.2 M KCl containing 20 mM $\text{K}_3\text{Fe}(\text{CN})_6$ (a) for bare GCE (b) for Au NW modified GCE [93]. (e) Amperometric response of Au-C-Pt/GCE with respect to different molarities of H_2O_2 in 0.1 M pH 7.0 PBS at 0 V. (f) Amperometric measurement of Au-C-Pt/GCE during the successive addition of 25 mM 10 μl H_2O_2 , GL, DA, UA, AA [109].

5.4 Experimental Procedure

5.4.1 Electrode Preparation

Prior to each electrode fabrication, graphite rods with 3 mm diameters were grinded with emery paper and polished with alumina dispersion with 1 μm and 0.3 μm sized particles. Following that, the tip of the graphite rods was ultrasonicated with ethanol and DI water for few minutes. 25 μl Ag-Pt NWs (75 $\mu\text{g}/\text{ml}$) and 5 μl Ag NWs (0.5 mg/ml) were deposited onto different graphite rods with the help of a micro pipette and left in air to dry.

5.5 Characterization Methods

5.5.1 Electrochemical Measurements

A three-electrode setup was used by operating a Biologic 3-channel VMP3 electrochemical workstation for the amperometric measurements, where the fabricated electrodes were used as working electrode (WE), Ag/AgCl in saturated potassium chloride (KCl) as the reference electrode (RE) and Pt wire as the counter electrode (CE). Schematic of the measurement setup is provided in Figure 5.5. All electrochemical measurements were conducted at room temperature and the reaction cell was filled with 15 ml of 0.1 M phosphate buffer (pH 7.0) solution. Under constant stirring at 500 rpm 25 μ l of 1, 5, 10 mM H_2O_2 solution was added to the phosphate buffer at an applied potential of 0.8 V vs. Ag/AgCl. During the amperometric measurements, different interferences were introduced into the phosphate buffer solution such as glucose, ascorbic acid, urea, lactic acid and oxalic acid to determine the selectivity of the sensor. Current change with time was recorded upon the addition of different analytes.

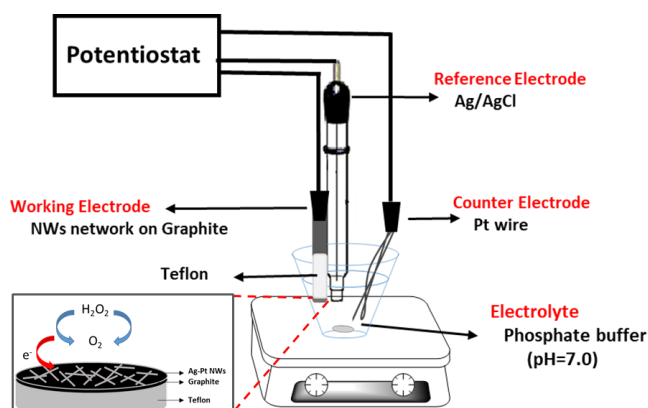


Figure 5.5 Schematic representation of the three-electrode setup used for the amperometric measurements in this work.

5.6 Results and Discussion

Before going into the results of amperometric measurements conducted for the determination of H_2O_2 , it is better to show the stability of Ag-Pt core-shell NWs against different concentrations of H_2O_2 . Environmental, chemical and electrochemical stabilities of the fabricated NWs were also investigated in a different study, where in all conditions Ag-Pt core-shell NWs showed enhanced stability over bare Ag NWs [110].

Ethanol solution of bare Ag NWs and Ag-Pt core-shell NWs were dropped onto different Si wafers and dried at room temperature. To determine the stability of NWs against H_2O_2 , 1 drop of H_2O_2 at concentrations of 1, 5, and 10 mM was dropped onto the Si wafer and dried at room temperature.

5.6.1 Stability of Ag-Pt core-shell NWs

SEM image of the galvanic replacement reaction free Ag-Pt core-shell NWs with smooth surfaces is provided in Figure 5.6 (a). For the stability tests, Ag-Pt core-shell NWs were subjected to 1, 5, 10 mM H_2O_2 and corresponding SEM images are provided in Figure 5.6 (b)-(d), respectively. When Ag-Pt core-shell NWs were exposed to 1 mM H_2O_2 , no change occurred on the NW integrity as well as the morphology (Figure 5.6 (b)). When H_2O_2 concentration was increased to 5 and 10 mM a similar result was obtained as shown in the SEM images given in Figure 5.6 (c) and (d), respectively. Increase in the concentration of H_2O_2 did not cause any deformation on the Ag-Pt core-shell NWs (Figure 5.6 (b)-(d)). Higher magnification SEM images in the insets of Figure 5.6 (b)-(d) also shows the stability of Ag-Pt core-shell NWs with no morphological change under H_2O_2 exposure.

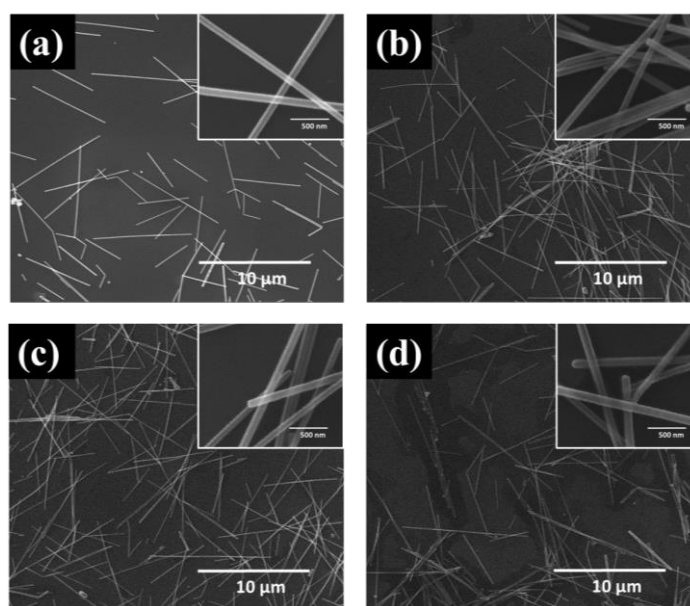


Figure 5.6 SEM images of the (a) Ag-Pt core-shell NWs without H₂O₂ exposure. After applying (b) 1 mM, (c) 5 mM, (d) 10 mM H₂O₂ onto the Ag-Pt core-shell NWs on the Si wafer (Insets shows high magnification SEM images).

5.6.2 Stability of Bare Ag NWs

Both before and after H₂O₂ exposure, the morphology of NWs were investigated via SEM. Figure 5.7 shows the effect of H₂O₂ on bare Ag NWs. SEM images of bare Ag NWs before any H₂O₂ exposure is provided in Figure 5.7 (a). Figure 5.7 (b)-(d) shows the effect of 1, 5, 10 mM H₂O₂ exposure to bare Ag NWs, respectively. Insets show the high magnification SEM images of the effect of H₂O₂ on NWs. A gradual increase in the destruction of NWs as the concentration of the H₂O₂ increases is observable from the SEM images. When 1 mM H₂O₂ was dropped on the NWs breakage of the NWs and deformation of the NW morphology was apparent in Figure 5.7 (b) compared to the bare NWs without any H₂O₂ exposure (Figure 5.7 (a)). Under 5 mM H₂O₂ exposure, rather than NW breakage, particle formation occurred and NW morphology was seriously damaged compared to 1 mM H₂O₂ exposure. In this case voids were formed on the NWs as shown in the inset of Figure 5.7 (c). The major effect was observed when NWs were exposed to 10 mM H₂O₂. They started to lose

the NW form (inset in Figure 5.7 (d)) due to the etching of Ag with H₂O₂. NWs formed into nanoparticles and accumulated to create bigger particles.

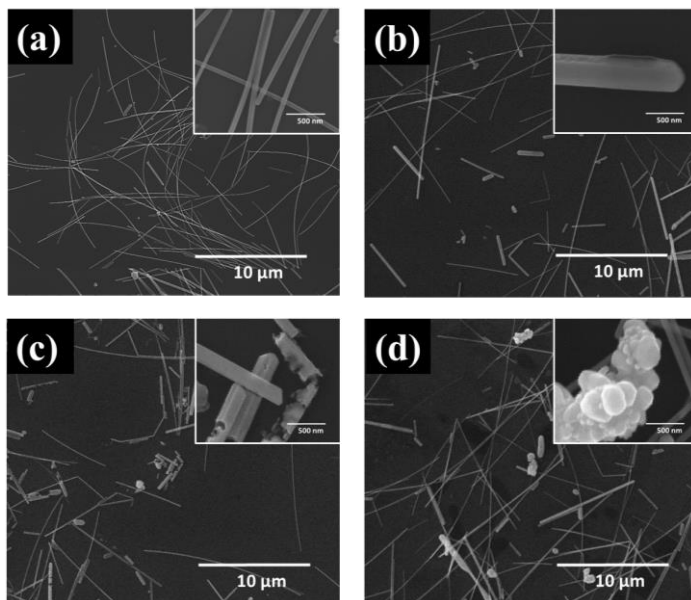


Figure 5.7 SEM images of the (a) bare Ag NWs before any H₂O₂ exposure. Ag NWs exposed to (b) 1 mM, (c) 5 mM, (d) 10 mM H₂O₂ (Insets shows high magnification SEM images).

5.6.3 Performance of Amperometric H₂O₂ Sensors

After proving that 1, 5, and 10 mM H₂O₂ solution does not cause a structural or morphological change on the Ag-Pt core-shell NWs, amperometric measurements for core-shell NW based electrodes were conducted according to the study by Koylan and Tunca et al. [111]. Performance of the bare Ag NW based H₂O₂ sensors is also given for comparison purposes.

5.6.3.1 Performance of Ag-Pt Core-Shell NW electrodes

To determine appropriate voltage, amperometric measurements were conducted under continuous stirring (500 rpm) while different potentials from 0 V to 1.2 V (vs. Ag/AgCl) were applied. At each measurement, 5 successive additions of 25 μl of 5

mM H_2O_2 was performed into the 0.1 M phosphate buffer (pH 7.0). Figure 5.8 shows the average peak currents for each applied potential. The highest current response was achieved when the applied potential was 0.8 V. Further increasing the applied potential caused the hydrolysis of the aqueous electrolyte, which led to a decrease in the average peak current response of the electrode. Accordingly amperometric measurements were conducted at an applied potential of 0.8 V.

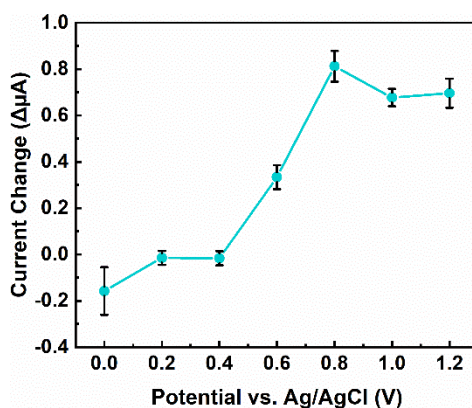


Figure 5.8 Change in current with respect to applied potential for the detection of 25 μl of 5 mM H_2O_2 in 0.1 M phosphate buffer (pH 7.0).

Amperometric measurements were conducted by adding of 25 μl of 1, 5 and 10 mM H_2O_2 into the 0.1 M phosphate buffer (pH 7) under continuous stirring at 500 rpm. The current response of the Ag-Pt NWs deposited on graphite electrodes was collected with respect to time. As shown in Figure 5.9 (a)-(c) under a constant applied potential of 0.8 V, current increases simultaneously with the addition of H_2O_2 . Such an increase in the current is followed by a steady state between subsequent additions of H_2O_2 . It was observed that the current difference between one steady-state plateau and the other increases with the increase in H_2O_2 concentration. The effect of different molarities of H_2O_2 on current response is also provided in Figure 5.9 (d). The current response of the electrode increases with the increase in H_2O_2 concentration as a result of the increased number of electrons produced by the oxidation of H_2O_2 . Response times for the successive addition of 1, 5 and 10 mM H_2O_2 at an applied potential of + 0.8 V (vs. Ag/AgCl) were calculated as 2.03, 2.18, and 2.44 seconds using 90% of the initial step change in the current.

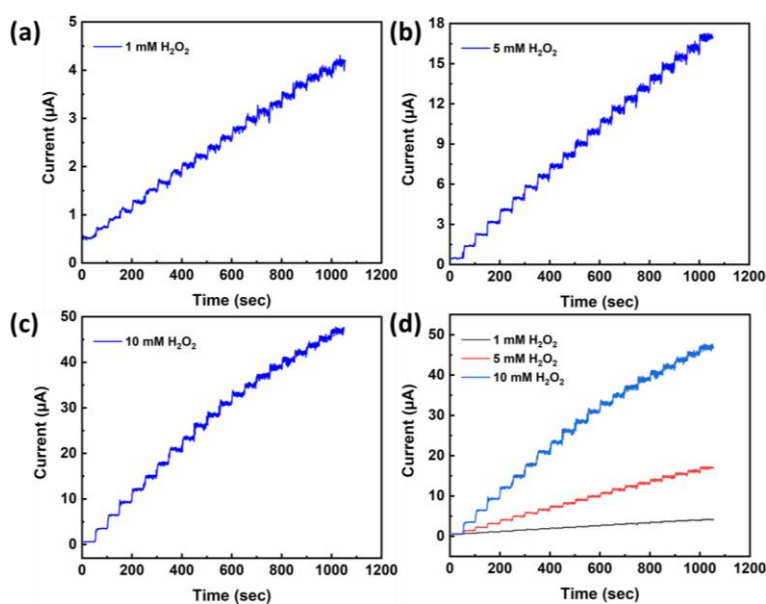


Figure 5.9 Amperometric response of Ag-Pt core-shell NW modified electrode with respect to subsequent addition of (a) 1 mM, (b) 5 mM, (c) 10 mM H₂O₂ into 0.1 M phosphate buffer at an applied potential of +0.8 V (vs. Ag/AgCl).

A linear relationship was observed between the current and molarity of the electrolyte. For the amperometric measurement conducted with 1 mM H₂O₂ regression equation was $I (\mu\text{A}) = 0.55 + 0.113 \times [\text{H}_2\text{O}_2]/\mu\text{M}$ with a correlation coefficient R^2 of 0.9995 (Figure 5.10 (a)). For 5 mM H₂O₂ and 10 mM H₂O₂ addition (Figure 5.10 (b) and (c)) regression equations were determined as $I (\mu\text{A}) = 0.68 + 0.102 \times [\text{H}_2\text{O}_2]/\mu\text{M}$ and $I (\mu\text{A}) = 1.08 + 0.167 \times [\text{H}_2\text{O}_2]/\mu\text{M}$ with correlation coefficients of R^2 of 0.9996 and 0.9984, respectively.

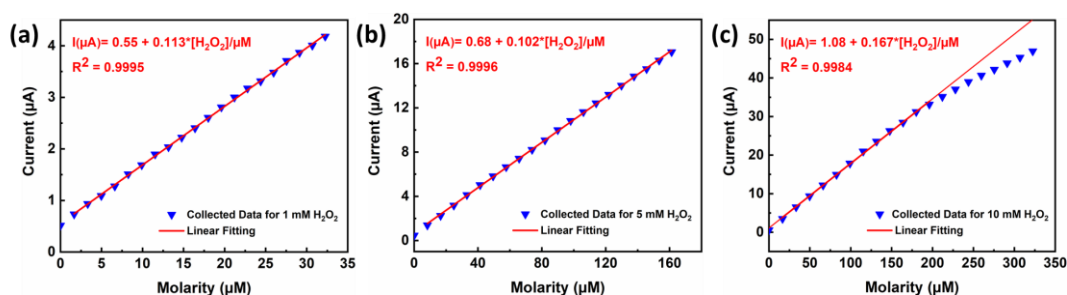


Figure 5.10 Calibration plot of Ag-Pt core-shell NW electrode for (a) 1 mM, (b) 5 mM, (c) 10 mM H₂O₂ addition with corresponding linear regression equations.

As shown in Table 1, according to the calibration plots, linear range was 1.69-32.29 μM for 1 mM H_2O_2 , 8.16-160.60 μM for 5 mM H_2O_2 , and 16.11-194.81 μM for 10 mM H_2O_2 addition. Sensitivity was calculated from the slope of the fitting lines. Sensitivities of 0.113 $\mu\text{A}/\mu\text{M}$, 0.102 $\mu\text{A}/\mu\text{M}$ and 0.167 $\mu\text{A}/\mu\text{M}$ for 1, 5 and 10 mM H_2O_2 addition, respectively, was obtained. The detection limit was calculated from 3.3 σ/n rule (σ is the standard deviation and n is the slope of the fitting line) and for 1, 5 and 10 mM H_2O_2 addition it was calculated as 0.33 μM , 1.37 μM and 4.75 μM , respectively.

Table 1. Comparison of sensitivity, linear range, and detection limit of amperometric measurements with Ag-Pt core-shell NWs conducted with the addition of 1, 5 and 10 mM H_2O_2 .

$[\text{H}_2\text{O}_2]$ (mM)	Sensitivity ($\mu\text{A}/\mu\text{M}$)	Linear range (μM)	Detection Limit (μM)
1	0.113	1.69-32.29	0.33
5	0.102	8.16-160.60	1.37
10	0.167	16.11-194.81	4.75

The successive addition of 1, 5 and 10 mM H_2O_2 was also recorded as shown in Figure 5.11 (a) to support the relationship between the increase in current with an increase in H_2O_2 concentration. At higher H_2O_2 concentrations, a larger current difference between two consecutive steady-state plateaus was observed. Another indication of a good sensor is its selectivity to specific analytes. Therefore, the selectivity of the amperometric sensor towards H_2O_2 was investigated in the presence of some possible electroactive interferents. Different interfering species such as AA, GL, urea and oxalic acid (OA) were chosen to represent physiological samples. During the amperometric measurements, successive addition of 5 mM H_2O_2 , GL, AA, urea and OA was performed at an applied potential of + 0.8 V (vs. Ag/AgCl). The current response of the electrode towards H_2O_2 and interferents is shown in Figure 5.11 (b). A clear current response was recorded corresponding to the addition of H_2O_2 , while no current response was observed for the addition of GL, AA, urea and OA representing the good selectivity of Ag-Pt core-shell NW electrodes towards H_2O_2 .

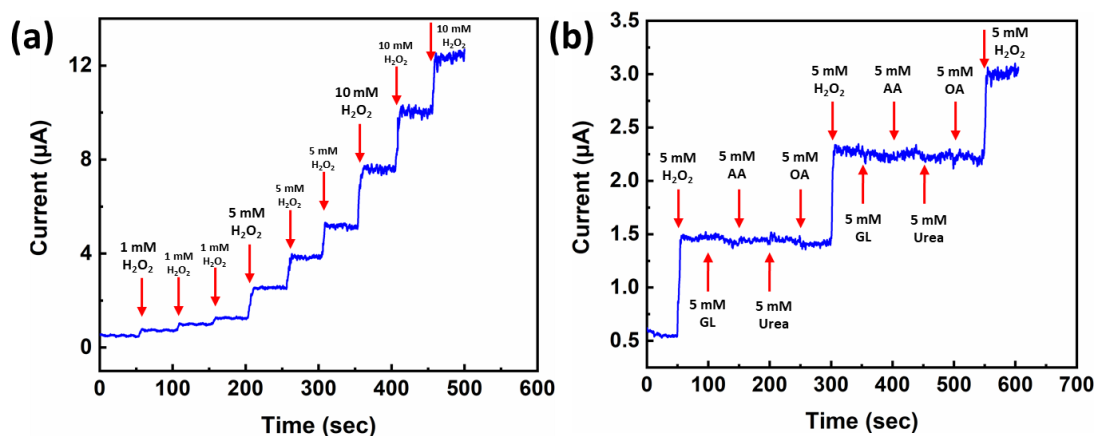


Figure 5.11 Amperometric response of Ag-Pt core-shell NW electrode to successive addition of (a) 1, 5, and 10 mM H₂O₂ (b) 5 mM H₂O₂, GL, AA, urea and OA.

The stability of Ag-Pt core-shell NW electrodes towards amperometric detection of H₂O₂ was investigated by conducting five successive amperometric measurements at an applied potential of + 0.8 V (vs. Ag/AgCl) using the same electrode. After each measurement, electrolyte was refreshed. Five amperometric measurements of the same electrode and average current response toward 5 mM H₂O₂ with the standard deviations are shown in Figure 5.12 (a) and (b), respectively. At each measurement, electrode showed similar response, which is also supported by the low standard deviations for the first five steps as 0.08, 0.11, 0.14, 0.18, 0.25, 0.27 μA. To show the reproducibility of the fabricated electrodes, 5 identical Ag-Pt core-shell electrodes were prepared. Amperometric response to 5 mM H₂O₂ in 0.1 M phosphate buffer at an applied potential of + 0.8 V (vs. Ag/AgCl) for 5 different electrodes is shown in Figure 5.12 (c) and the responses are represented as bar charts in Figure 5.12 (d). The current response of the electrodes was very close to each other. Differences in the current response of the electrodes were found to be negligible since manual addition of H₂O₂ by the operator causes minor differences in the injection speed, micropipette distance and position. The stability of the fabricated electrodes due to the high stability of Ag-Pt core-shell NWs in harsh H₂O₂ environments in addition to good selectivity and reproducibility makes the fabricated Ag-Pt core-shell NWs promising electrode materials for H₂O₂ sensors.

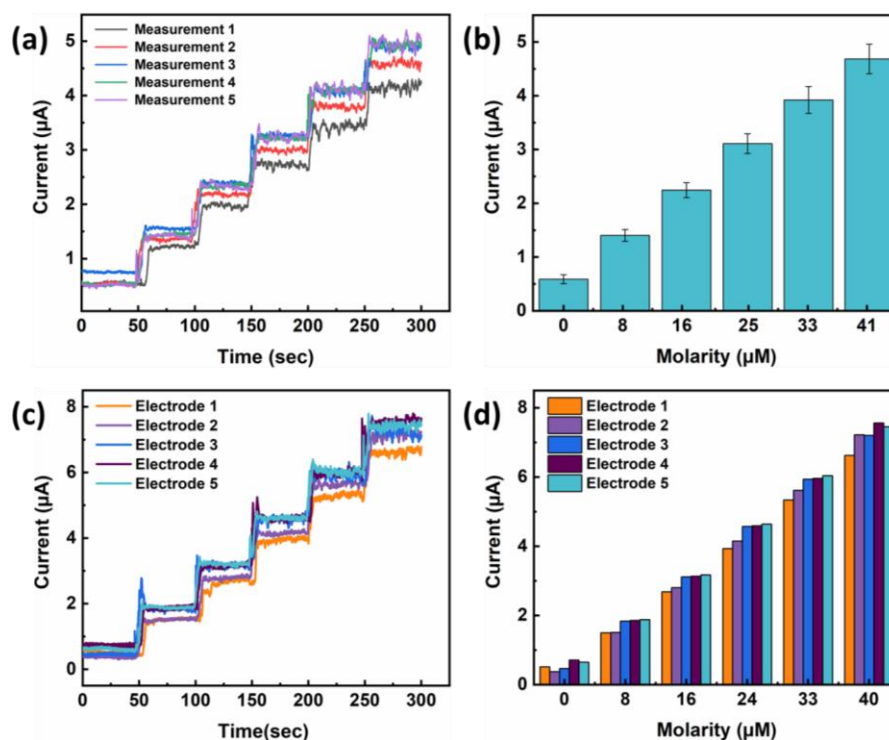


Figure 5.12 (a) Five successive amperometric responses of a single Ag-Pt core-shell NW electrode to 5 mM H₂O₂ in 0.1 M phosphate buffer at an applied potential of +0.8 V (vs. Ag/AgCl). (b) Bar chart showing the average current response of five amperometric measurements of the same Ag-Pt core-shell NW electrode against the successive addition of 5 mM H₂O₂ in 0.1 M phosphate buffer at an applied potential of +0.8 V (vs. Ag/AgCl). (c) Amperometric measurements of five different Ag-Pt core-shell NW electrodes against 5 mM H₂O₂ in 0.1 M phosphate buffer at an applied potential of +0.8 V (vs. Ag/AgCl). (d) Bar chart corresponding to the amperometric measurements of five identical electrodes against 5 mM H₂O₂ in 0.1 M phosphate buffer at an applied potential of +0.8 V (vs. Ag/AgCl).

Linear range and detection limit of the fabricated Ag-Pt core-shell NW electrodes are compared to other metal nanostructures of previous studies for the detection of H₂O₂. Performance of the fabricated sensors greatly depends on the measurement conditions therefore, direct comparison of the performance of H₂O₂ sensors was difficult. However, in this work, sensors fabricated from Ag-Pt core-shell NWs as novel electrode materials provide promising results in terms its linear range and detection limit when compared to those in literature as compared in Table 2.

Table 2. Comparison of H₂O₂ sensors in terms of their linear range and detection limit.

Electrodes	Linear Range (μM)	Detection Limit (μM)
Ag NWs Array [84]	100-3100	29.2
Ag-C-Ag NPs [104]	70-10000	23
Ag-C-Pt NPs [106]	9-1860	1.3
Ag NPs-Graphene-GC [98]	100-40000	28
Pt NPs-GCE [103]	5-1650	0.65
Ag NPs-NFC [99]	100-80000	62
Ag NWs-GCE [85]	1-1075	0.05
Ag NWs-GC [100]	50-10350	10
Ag-Pt Core-Shell NWs (This Work)	16.1-194.8	4.75

5.6.3.2 Performance of Bare Ag NW Electrodes

To compare the performance of Ag-Pt core-shell NW based amperometric H₂O₂ sensors with bare Ag NW based H₂O₂ sensors, performance of the bare Ag NW sensors were also investigated at an applied potential of 0.8 V (vs. Ag/AgCl). Amperometric measurements were again conducted in 0.1 M phosphate buffer (pH 7.0) under constant stirring (500 rpm).

To determine the response of the Ag NW based H₂O₂ sensor, addition of 5 mM of H₂O₂ was performed in every 50 seconds. However, no current response was detected for the addition of 5 mM H₂O₂. Concentration of the H₂O₂ was further increased and current responses of the electrodes was collected as provided in Figure 5.13 (a) for 10 mM and 100 mM H₂O₂ addition. Higher current response was observed for the 100 mM of H₂O₂ addition compared to 10 mM H₂O₂ addition. However, still the current response of the bare Ag NW electrodes were lower than that of Ag-Pt core-shell NW based electrodes. Also no clear step wise current response was observed when bare Ag NWs were used. From the calibration curve provided in Figure 5.13 (b) sensitivity of the bare Ag NW electrodes was determined

as $2.11 \times 10^{-4} \mu\text{A}/\mu\text{M}$ for 100 mM of H_2O_2 addition. This was significantly lower than the sensitivity of the Ag-Pt core-shell NW based H_2O_2 electrodes. Low current response and sensitivity of the bare Ag NW electrodes under 0.8 V (vs. Ag/AgCl) (Figure 5.13 (a) and (b)), in addition to the SEM images of bare Ag NWs that were exposed to H_2O_2 solution (Figure 5.7) indicated that performance of the bare Ag NWs are restricted by the instability and dissolution of Ag against H_2O_2 and electrochemical measurements. Such insufficient performance of the bare Ag NW based amperometric H_2O_2 sensors highlights the importance of the utilization of the Ag-Pt core-shell NWs for the amperometric detection of H_2O_2 .

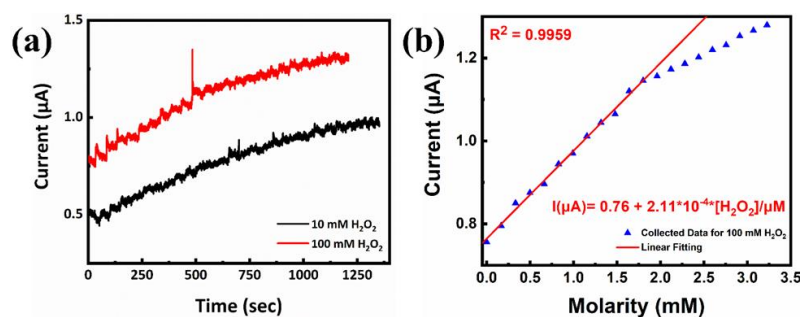


Figure 5.13 Amperometric response of bare Ag NW electrodes for the detection of 10 mM (black) and 100 mM H_2O_2 (red) under an applied potential of 0.8 V (vs. Ag/AgCl). (b) Calibration plot of bare Ag NW electrode for the addition of 100 mM H_2O_2 with corresponding linear regression equation in the linear concentration range of 756-1800 μM .

CHAPTER 6

SILVER-PLATINUM CORE-SHELL NANOWIRE NETWORK BASED SUPERCAPACITOR ELECTRODES

6.1 Introduction

Alternative energy sources and storage systems were developed to fulfill the need for high energy and high power density [112]. Such energy storage systems are now essential to power hybrid/electric vehicles, electronic gadgets and to store energy from renewable sources. In that sense, electrochemical capacitors (ECs) are in high demand considering their ability to deliver and store electrical energy at high rates. [113].

Figure 6.1 shows the Ragone plot, which demonstrates the performance of the energy storage systems (ESSs) with respect to the change in specific energy with a specific power. High energy and low power region represent the characteristics of batteries, where they can provide low power for long time applications. Li-ion batteries dominate the market due to their high energy density. However, short battery life (a few thousand cycles) and long charging time because of the volume changes during charging-discharging, ion diffusion in the bulk, phase transformations and size dependent energy density of batteries limit their uses for small sized and wearable devices [113],[114]. Capacitors, on the other hand, lie in the low energy and high power region. ECs, also called supercapacitors or ultracapacitors, fill the gap between batteries and capacitors in energy and power and can deliver high power compared to batteries for short operation periods. Although they manage a hundred to thousand times higher power, they store lower charge compared to batteries [112]. They can be charged/discharged in a few seconds thus, they have lower energy density than batteries. But they can deliver/uptake higher power for shorter times [115]. Different than conventional capacitors, supercapacitors are composed of

electrodes with higher effective surface area, which in turn increases the capacitance of the supercapacitors (by roughly 10^4 times than conventional capacitors) [116].

Therefore, the performance of supercapacitors can complement or even replace batteries where the system needs to store/release high amount of energy in seconds with high reliability and exceptional cycle life [117],[113]. Hence, supercapacitors are usually used in hybrid electric vehicles, portable electronics, uninterruptible power supplies (UPS), volatile memory backups in PCs, wind turbines and etc. [118],[119], [120].

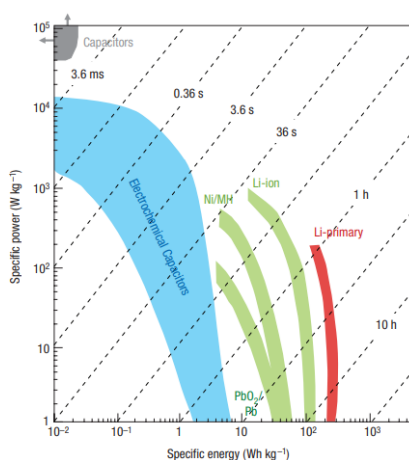


Figure 6.1 Ragone plot for the comparison of energy storage devices [115].

6.2 Working Principle of Supercapacitors

Different electrochemical mechanisms take place in supercapacitors. The charge storage property depends on these mechanisms. For batteries, redox reactions occur in the bulk of the electrode due to the diffusion controlled, slow insertion of Li^+ ions. On the other hand, no redox reactions take place in electrical double layer capacitors (EDLCs) and charge is stored through adsorption of electrolyte ions onto the electrode surface. Such redox reaction free mechanism gives rise to high power supercapacitors with fast response against changes in potential, whereas surface confined charge storage mechanism brings lower energy density compared to batteries [121]. Thanks to such surface storage very little amount of volume change

of the electrode occur, which brings fast charging ability and long cycle life (over 10^6 cycles of charge-discharge) to the supercapacitor [113]. A different type of supercapacitors, pseudocapacitors, on the other hand, are operated with fast redox reactions. Such faradaic reactions enhance the charge storage ability and allows pseudocapacitors to possess high energy and power densities [114],[117].

A typical supercapacitor cell consists of current collectors, film of an active material electrode, separator and electrolyte. Two electrodes can be composed of the same composition in symmetric supercapacitor configuration or can be different in asymmetric supercapacitors. To prevent the electrical contact of electrodes a separator allowing transfer of ionic charges having high ionic conductance and low thickness is soaked in an electrolyte and placed between the electrodes. Depending on their active material and charge storage mechanism, there exist different types of supercapacitors as electrical double-layer capacitors (EDLCs), pseudocapacitors (redox capacitors) and hybrid capacitors (Figure 6.2) [112], [113],[115].

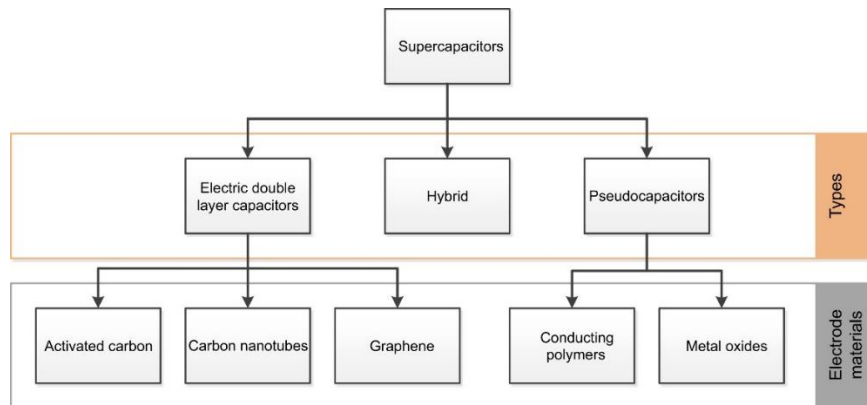


Figure 6.2 Types of supercapacitors [112].

6.3 Types of Supercapacitors

6.3.1 Electrical Double Layer Capacitors

In EDLCs, charge is stored electrostatically through reversible electrolyte ion adsorption and desorption onto the active material [115]. At the electrode electrolyte

interface oppositely charged layers are created due to electrostatic attraction between the electrode surface and electrolyte ions [114]. Double layer capacitance arises from the electrostatically stored surface energy at the interface of the electrodes [119]. Energy is stored non-faradically and no redox reactions occur in EDLCs type supercapacitors. This provides long life ($>10^6$ cycles) and high power delivery and uptake capability. Rectangular box-shaped cyclic voltammograms (CVs) and galvanostatic charge-discharge (GCD) plots are the indications of non-faradaic nature of the charge-storage mechanism. Mainly electrode materials with high surface area are used. Nanoporous carbon is the most typical one for efficient ion adsorption onto the electrode. Due to the polarization at the interface of electrode and electrolyte, charge separation occurs, which was described with the double-layer capacitance by Helmholtz [113]:

$$C = \frac{\epsilon_r \epsilon_0 A}{d}$$

,where C is the double-layer capacitance, ϵ_0 and ϵ_r is the dielectric constant of vacuum and electrolyte, respectively, A is the surface area of the electrode, and d is the effective thickness of the double layer (charge separation distance) [113]. Helmholtz described the EDL in a way that all the charges were assumed to be adsorbed on the surface of the electrode. Later Gouy and Chapman modified the previous model and suggested that ions are not rigid and attached to the electrode surface, they tend to diffuse into the solution and the thickness of the diffusion layer is determined by the kinetic energy of the ions. In this diffusion model, from the analytical point of view Boltzmann distribution was followed for the ionic concentration near the electrode surface. However, the model fails experimentally, where calculated double layer thickness is smaller than the measured thickness for highly charged double layer. Better representing the reality, a model was developed by Stern (Figure 6.3), where previous two Helmholtz and Gouy-Chapman models were combined and ions were stated to have a finite size with a limited approach to the surface. Two distinct layers were explained for EDL as the inner-Stern layer (Helmholtz layer) and outer-diffuse layer (Gouy-Chapman) [112], [120].

This model clarifies the EDL on plane surfaces, however, ion electrosorption in supercapacitors with nanoporous electrodes thus, the charge storage mechanism still requires a better understanding of the behavior of ions in the nanopores and the effect of pore size [113], [114].

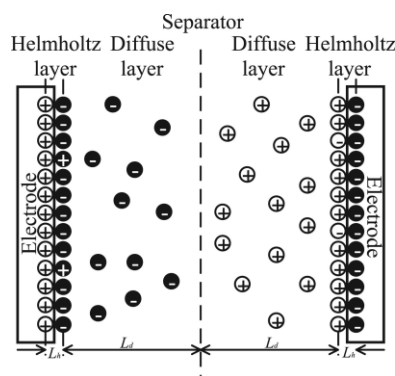


Figure 6.3 Schematic of the EDL model of Gouy-Chapman-Stern [120].

6.3.2 Pseudocapacitors

Different than EDLCs, pseudocapacitors or redox capacitors are operated such that fast redox reactions take place at the active material surface. Charge storage mechanism of the pseudocapacitors is not entirely based on electrostatics; but also involves faradaic processes and redox reactions. Instead of static separation of charges, redox reactions occur across the double layer [116]. This in turn improves the capacitance and energy density [113]. Over the years, pseudocapacitors gained high interest due to their potential to combine battery like high energy density and EDLC like long cycle life and power density [114]. The presence of redox reactions enhances the charge storage ability compared to EDLCs. Therefore, similar to EDLCs, rectangular box-shaped CVs are observed for pseudocapacitor devices. Such confinement of redox reactions differentiates pseudocapacitors from batteries, where the faradaic reaction occurs in the bulk [113], [115]. Different than the faradaic reactions in bulk for batteries, pseudocapacitive materials follows the characteristics of linear dependence of charge on potential (which results in a mechanism based on the transfer of electrons rather than the accumulation of charges

[116]). Capacitance for pseudocapacitor is represented by the following equation [116];

$$C = \frac{d(\Delta q)}{d(\Delta V)}$$

,where C is the pseudocapacitance, which is the derivative of charge acceptance (Δq) and potential change (ΔV). Capacitance is obtained by the applied potential that produces faradaic current from redox reactions of the electroactive materials [116].

An illustration showing the comparison of the electrode processes taking place for EDLCs and pseudocapacitors together with battery like storage devices is given in Figure 6.4. Figure sums up the nature and kinetics of each of the charge storage mechanisms.

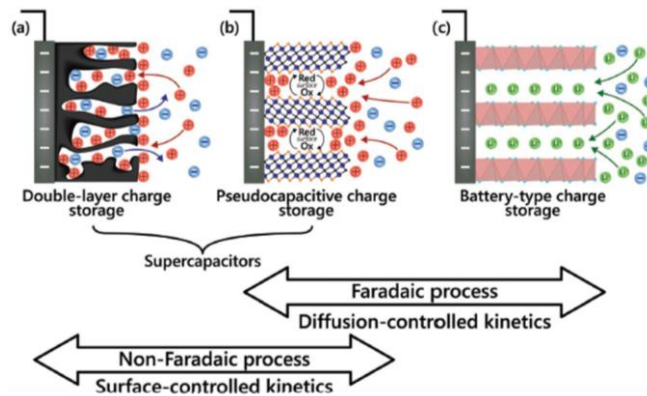


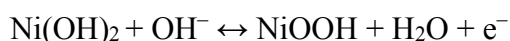
Figure 6.4 Schematic representation of the processes occurring for (a) EDLC, (b) pseudocapacitive and (c) faradaic electrode materials [122].

Electroactive materials representing the pseudocapacitive behavior are the ones that exhibit high charge/discharge rates and high energy densities [114]. Manganese oxide (MnO_2) [123], ruthenium oxide (RuO_2) [124], iron oxide (Fe_3O_4) [125], nickel hydroxide ($Ni(OH)_2$) [126],[127] and nickel oxide (NiO) [128] also conducting polymers (negatively charged (n-type) and positively charged (p-type)) such as, polyaniline (PANI) [129], polypyrrole (PPy) [130] and polythiophene (PTP) were widely used for the fabrication of pseudocapacitors. For the well-known pseudocapacitive material of RuO_2 high capacitance was achieved through fast and

reversible electron transfer with insertion and de-insertion of protons into the anhydrous RuO₂ according to the following reaction [115];



,where $0 \leq x \leq 2$ over a potential window of ~ 1.2 V [115]. Together with NiO, which is a cheap and environmentally friendly pseudocapacitive material with a theoretical capacitance of 2583 F g^{-1} in the potential window up to 0.5 V, Ni(OH)₂ is also recognized as a promising electrode material [128]. Both crystalline and amorphous Ni(OH)₂ shows unique electrochemical behavior. Ni(OH)₂ nanosheets that were grown on Ni foam showed excellent performance with a specific capacitance of 2384.3 F g^{-1} at 1 A g^{-1} by preserving 75 % of its initial capacitance after 3000 cycles. The faradaic reaction associated with Ni(OH)₂ is as follows [127];



As an example of conductive polymers, PANI is a very promising material for pseudocapacitors due to its ease in preparation (chemically or electrochemically), high specific capacitance values and electrical conductivity ($0.1\text{-}5 \text{ S cm}^{-1}$) in addition to its environmental stability [116]. A specific capacitance of 1210 F g^{-1} was reported for PANI nanofibers by Zhang et al. [131].

However, the use of aqueous electrolytes for the operation of conventional pseudocapacitive materials restricts the voltage window (up to ~ 1 V) and consequently restricts both the energy and power density. Also, the high cost of RuO₂, low cycling stability due to the high tendency of decomposition of conductive polymers with time as a result of mechanical stress (swelling-shrinking during redox reactions) and low electrical conductivity and limited capacitance of MnO₂ creates obstacles in the way of widespread use of commercially offered pseudocapacitors. Thus, the commercialized use of pseudocapacitors still requires some improvements on the device and material fabrication [113], [115].

6.3.3 Hybrid Supercapacitors

Improved capacitance and energy storage capability are achieved by coupling an EDLC and pseudocapacitor taking advantage of both of their characteristics. The combination of the properties and storage mechanisms of EDLCs and pseudocapacitors enhance the characteristics of hybrid devices. In addition to higher working potential, higher energy and power density than an EDLC and pseudocapacitor alone achieved through hybrid supercapacitors. According to such a coupling approach, hybrid systems are composed of capacitor-like (nonfaradaic) and battery-like (faradaic) electrodes and can possess a symmetric or asymmetric assembly of electrodes [116].

Most of the commercial hybrid devices combine a capacitive porous-carbon electrode with a Li-ion battery graphite anode, which is known as Li-ion capacitors (LIC) reaching a high operating voltage of 2.2 - 3.8 V. Although they have high energy density values ($> 20 \text{ Wh kg}^{-1}$) they suffer from low power capability compared to EDLCs [113]. Some other commercially available hybrid supercapacitors are also conducting polymer based asymmetric devices, which provides high specific capacitance. Charge is stored and released through the redox reactions. Ions are transferred through the polymer backbone during oxidation, and they are transferred back to the electrolyte in the reduction step. In addition to the behavior of electrode materials, internal resistance (related to the current collectors, electrolyte resistance, equivalent series resistance (ESR)) are very critical in terms of power performance of a supercapacitor. Therefore choosing proper electrode materials together with a suitable electrolyte is very important for the overall performance of hybrid supercapacitors [116].

6.4 Experimental Procedure

6.4.1 Fabrication of Core-Shell Nanowire Networks

Ag-Pt core-shell NWs, dispersed in ethanol was deposited onto glass via spray deposition method. Glass substrates were cleaned beforehand through 15 min ultrasonication in acetone, ethanol and DI water. Similar to the spray deposition of Ag NWs, glass substrates were placed on a hot plate at 110 °C. With an air brush Ag-Pt core-shell NWs were deposited from a 15 cm distance to the substrate at a pressure of 2.5 atm. Upon vaporization of the solvent, random NW network was obtained.

6.5 Characterization Methods

6.5.1 Electrochemical Measurements

For the characterization of supercapacitor electrodes, a Biologic (VMP 3) 3-channel Electrochemical Workstation was utilized. A three-electrode setup was used where all the electrochemical measurements were conducted at room temperature (Figure 6.5). In a three-electrode setup working electrode (WE) was the active material electrode and a reference electrode (RE) was positioned close to the WE. Potential applied to the WE is with respect to the RE of Ag/AgCl electrode (in saturated potassium chloride (KCl)). A Pt plate was used as a counter electrode (CE). As being chosen from one of the inert materials such as Pt, Au, and graphite rod CE allows the current to travel through the system without causing a chemical reaction on itself. All three of the WE, RE, and CE were connected to a potentiostat [132]. Thanks to this three-electrode setup, potential changes occurring at the WE were measured independently from any possible changes occurring at the CE. Different electrolytes were chosen for different electrochemical procedures. For the electrodeposition of Ni(OH)₂, 0.1 M nickel acetate (Ni(OCOCH₃)₂·4H₂O) solution was used as the

electrolyte. For the electrochemical characterization of Ag-Pt-Ni(OH)₂ nanocomposite electrodes 1 M KOH was chosen as the electrolyte.

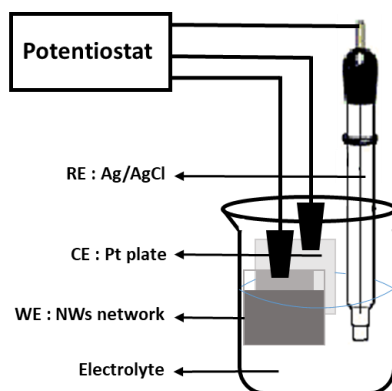


Figure 6.5 Schematic illustration of the three-electrode setup configuration.

6.5.1.1 Cyclic Voltammetry (CV)

CV is one of the most common techniques that is used for the qualitative and quantitative electrochemical characterization of various types of active materials of the WE. A potential is applied to the WE with respect to the RE (having a fixed potential). A certain potential window is scanned in forward and reverse directions with different scan rates, while recording the current that passes through the system. It provides information about the kinetics, mechanism and reversibility of the electrochemical reactions occurring on the electrode surface and in the electrolyte. For an ideal supercapacitor, rectangular-box shaped CV graphs should be observed as shown in red curve (a) in Figure 6.6. The rectangular shape is also common for EDLCs, shown with the blue dashed lines in Figure 6.6 (b). CV graph of pseudocapacitive materials on the other hand shows redox peaks as in the green dashed lined CV plot in Figure 6.6. In the case, where there is a supercapacitor with high resistivity CV plot appears to be a parallelogram. Also increasing the scan rate may cause distortion from the ideal rectangular CV curve since the kinetics of the electrochemical processes may not follow the fast changes in the potential [132],[133].

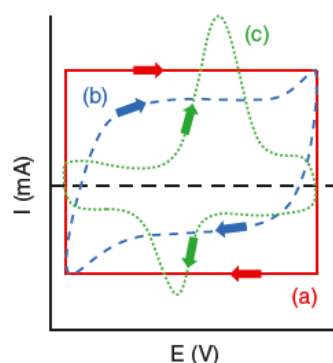


Figure 6.6 (a) Rectangular-box shaped ideal capacitor CV curve. CV curves of (b) EDLC and (c) redox reaction peaks of pseudocapacitive materials [132].

Electrochemical properties of the electrodes can be studied according to the scan rates and specific capacitance of the electrodes can be calculated. Using the area under the CV in a potential window from E_1 (V) to E_2 (V), specific capacitance (C_{sp} ($F\ g^{-1}$)) can be obtained through the equation shown below, where i (A) represents the measured current and m (g) represents the mass of the active material on the WE [132]:

$$C_{sp} = \frac{1}{m(E_2 - E_1)} \int_{t=0(E_1)}^{t(E_2)} i(E) dt$$

6.5.1.2 Galvanostatic Charge-Discharge (GCD)

Another method to measure the capacitance of a material is the GCD measurement. A constant current is applied and changes in the potential are measured with respect to time. To determine the capacitance, WE is charged to a potential and the discharge process is monitored. EDLCs and pseudocapacitive materials display different GCD behaviors as shown in Figure 6.7. A linear charge-discharge behavior is observed for EDLCs (like triangle), whereas nonlinearity (voltage plateaus) is observed in the presence of redox reactions for pseudocapacitive materials [132].

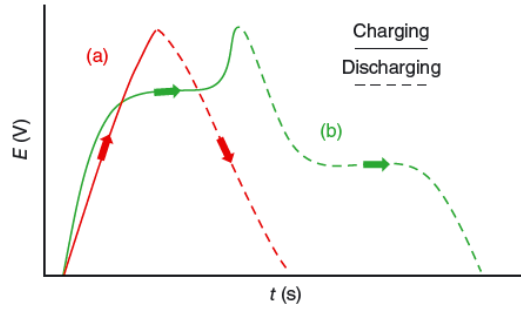


Figure 6.7 GCD curves for (a) EDLCs, (b) pseudocapacitive materials [132].

Different equations for C_{sp} are present since different GCD behaviors are observed for EDLCs and pseudocapacitive materials. For EDLCs, specific capacitance is obtained from the slope of the discharging process as shown in the equation below, where C_{sp} ($F\ g^{-1}$) is the specific capacitance, ΔV is the potential (voltage) window, m (g) is the mass of the total active material, I (A) is the current, and Δt is the time passed for the discharge process :

$$C_{sp} = \frac{I}{m \frac{\Delta V}{\Delta t}}$$

Due to the presence of the redox reactions for the pseudocapacitive materials, calculations from the discharge curve is not possible. Therefore, integral of the area under the discharge section is used to calculate the specific capacitance. According to the following equations, discharge energy, E , capacitance of the cell, C_{cell} , and specific capacitance, C_{sp} , can be calculated.

$$E = I \int_{t(V_{max})}^{t(V_{min})} V(t) dt \quad C_{cell} = \frac{2E}{V_{max}^2} \quad C_{sp} = 4C_{cell}$$

Here, I represents the current in ampere (A), V is the voltage window in volts (V), and t is the discharging time in seconds (s). C_{cell} is calculated according to two series connected electrodes and it contains masses of two electrodes, therefore C_{sp} is four times the value of C_{cell} .

Using GCD curves maximum energy (E_{max}) and power (P_{max}) density of the full cell device can also be calculated, where V_{cell} represents the cell voltage, C_{cell} is the capacitance of the cell, R_{esr} equivalent series resistance, and m (g) total mass of the two serially connected electrode. P_{max} ($W\ kg^{-1}$) and E_{max} ($Wh\ kg^{-1}$) is as shown in the equations below [132]:

$$E_{max} = \frac{1}{2} C_{cell} (V_{cell})_{max}^2 \quad P_{max} = \frac{1}{4m} \frac{(V_{cell})_{max}^2}{R_{esr}}$$

6.5.1.3 Electrochemical Impedance Spectroscopy (EIS)

EIS is used to measure the electrical series resistance (ESR) and help to further investigate the electrochemical characteristics of the material. Over a frequency range of 0.01 Hz to 1 MHz, small magnitudes of an alternating current is applied to the supercapacitor [132]. A Nyquist plot showing imaginary resistance (Z'') against real resistance (Z') is obtained in which the point intersection of the impedance curve on the x-axis gives the ESR of the cell (Figure 6.8). A semicircle followed by a line region of 45° and 90° is typical for the charge storage mechanisms of capacitive and pseudocapacitive materials [122]. In the lower frequency region, a 45° line starting from the ESR which continues as a parallel (close to parallel) to the imaginary axis is typical for porous electrodes. Such a behavior shows that in a short time all the reactive sites on the electrode are accessible showing a capacitor-like behavior [134]. On the other hand, a semicircle formation at the high-frequency region is correlated to the interfacial impedance originated at the interface of the current collector and the active material or due to charge transfer resistance. Recording the ESR at different potentials can help to distinguish the reason for such behavior since interfacial impedance will be constant through all the potentials. In addition to that, throughout the three-electrode measurements, the impedance of the cell is affected from the position of the RE with respect to WE, use of porous frits at the tip of the RE, presence of air bubbles, or clogging in the filling solution of the RE. Therefore,

for the EIS measurements maintenance and proper selection of the RE is highly important [122].

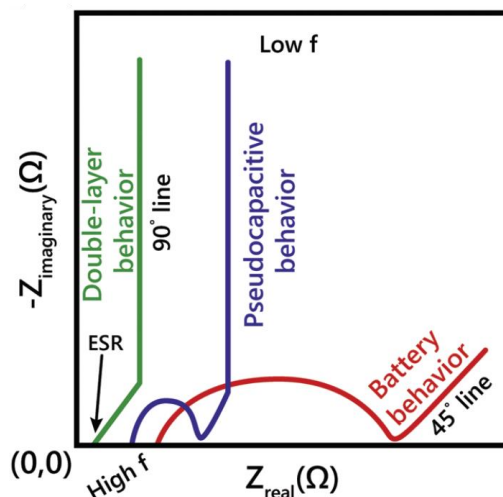


Figure 6.8 Representation of a typical Nyquist plot showing the behavior of an EDLC (green), a pseudocapacitive material (blue) and a battery (red) [122].

6.6 Results and Discussion

6.6.1 Electrochemical Deposition of Ni(OH)₂

A three-electrode setup was used and Ag-Pt core-shell NW network prepared on PET substrate was used as WE. Conformal deposition of Ni(OH)₂ was performed according to the previous work done by Yuksel et al. [46]. Electrodeposition was conducted using 0.1 M freshly prepared nickel acetate (Ni(OCOCH₃)₂·4H₂O) solution under a constant potential of -0.9 V (vs. Ag/AgCl). Deposition of Ni(OH)₂ was performed for different periods of times as, 100, 200, 400 and 600 sec. Figure 6.9 shows SEM images representing the effect of deposition time on the morphology of the fabricated Ag-Pt-Ni(OH)₂ NWs.

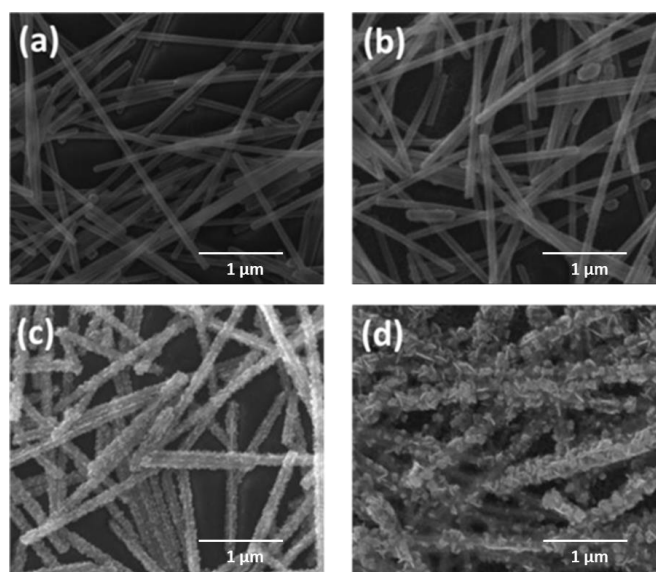


Figure 6.9 SEM images of the Ag-Pt-Ni(OH)₂ nanocomposites fabricated using deposition times of (a) 100, (b) 200, (c) 400 and (d) 600 sec.

The optimum deposition time was determined as 400 sec since Ni(OH)₂ flake formation and a considerable amount of thickness increase (~ 15 nm) was observed for 400 sec of deposition. For the 600 sec deposition, cracks in Ni(OH)₂ were observed visually on the electrode material due to excessive coating of Ni(OH)₂.

EDS mapping was conducted on the 400 sec Ni(OH)₂ deposited Ag-Pt core-shell NWs. Results are provided in Figure 6.10 (a). Figure 6.10 (b) shows EDS maps for Ag, Pt and Ni, where the conformal deposition of Ni(OH)₂ on Ag-Pt core-shell NWs was achieved.

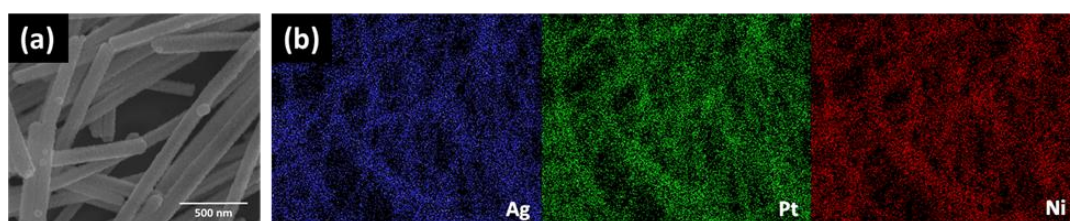


Figure 6.10 (a) SEM image, (b) EDS maps for Ag (blue), Pt (green) and Ni (red) for 400 sec Ni(OH)₂ deposited Ag-Pt core-shell NWs.

To further characterize the Ag-Pt-Ni(OH)₂ electrodes, XPS analysis was performed for Ni 2p and results are provided in Figure 6.11 (a). Two peaks at 855.8 and 873.4

eV corresponds to Ni 2p_{3/2} and Ni 2p_{1/2}, respectively. The spin energy difference is 17.6 eV, which is characteristic to the Ni(OH)₂ phase and their satellite peaks at 861.5 and 880.6 eV corresponds to the Ni 2p_{3/2} and Ni 2p_{1/2}, respectively, is in good agreement with previous studies in literature [126],[135],[136]. XRD was conducted to determine the phase of the electrodeposited Ni(OH)₂. Figure 6.11 (b) shows the XRD pattern of Ag-Pt core-shell NWs and Ag-Pt-Ni(OH)₂ nanocomposite electrodes. Diffraction angles of 38.82°, 45.14° and 65.72° were assigned to be (111), (200) and (220) planes, respectively, and showed that Ag-Pt core-shell NWs has the FCC structure. XRD patterns of Ag-Pt-Ni(OH)₂ nanocomposite electrodes is given in Figure 4.7 (b) were the diffraction angles of 38.44°, 52.02° and 65.04° corresponds to the (011), (012) and (111) planes of β -Ni(OH)₂ (JCPDS Card no: 74-2075) having hexagonal structure. Results shows that there exist only β -Ni(OH)₂, which is the preferred phase since β -Ni(OH)₂ has higher stability than α -Ni(OH)₂ and widely used for electrochemical applications.

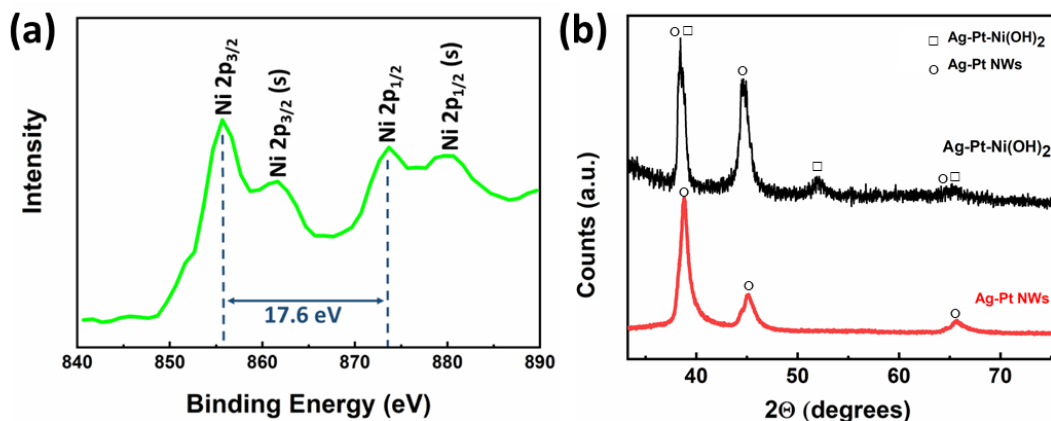
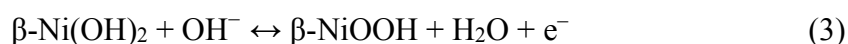


Figure 6.11 (a) XPS spectrum of Ni 2p from Ag-Pt-Ni(OH)₂ electrodes. (b) XRD patterns of Ag-Pt core-shell NWs (red) and Ag-Pt-Ni(OH)₂ nanocomposite electrodes (black).

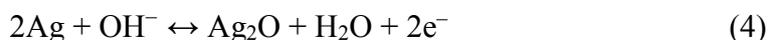
6.6.2 Electrochemical Characterization

6.6.2.1 Nanocomposite Electrodes

Electrochemical characterization of Ag-Pt-Ni(OH)₂ nanocomposite electrodes was conducted via CV, GCD and EIS methods. CV measurements were conducted in an aqueous solution of 1 M KOH within the potential window of 0 - 0.6 V (vs. Ag/AgCl). The potential window was determined considering the existence of reversible and strong redox reactions within the specific potential range. Redox peaks apparent in the CV measurements in Figure 6.12 (a) are due to the transformation of β - Ni(OH)₂ to β - NiOOH according to the Reaction (3) shown below:



Ag-Pt NW network functioned as a stable conducting path for the deposition of Ni(OH)₂ layer and charge transfer between core and Ni(OH)₂ layer was obtained. Strong peaks at 0.16 V and 0.48V correspond to the oxidation and reduction peaks for Ag-Pt-Ni(OH)₂ nanocomposite, according to the reversible Faradaic reaction in (4), respectively. Peaks at 0.04 V and 0.16 V on the other hand corresponds to the Ag/Ag⁺ redox couple due to the reversible redox reactions of the thin layer of silver (I) oxide (Ag₂O) formed during the CV measurements according to the following Reaction (4):



Although there also exists the pseudocapacitive behavior of partially coated Ag-Pt NWs, which are in contact with the KOH electrolyte, their effect on pseudocapacitance is insignificant compared to the overall Ni(OH)₂ layer on Ag-Pt core-shell NWs. During the CV measurements, increasing the scan rate led to an increase in redox reaction peak intensities in addition to the peak shifts towards the opposite directions. As the scan rate is increased, active materials can not interact sufficiently with the electrolyte ions to take part in the Faradaic reactions due to the

ionic-electronic diffusion limitation. As a result of such restriction in the redox reactions at high rates, specific capacitance decreases accordingly. This shows the rate-dependency of the charge storage capacity [137].

Specific capacitance of the electrodes were calculated according to the following equation, where I represents charge-discharge current in ampere (A), Δt discharging time in seconds (s), m mass of the active material in grams (g), and ΔV potential drop during discharging in volts (V):

$$C_{sp} = \frac{I \times \Delta t}{m \Delta V}$$

GCD measurements were conducted in a potential window of 0 - 0.6 V at different current densities ranging from 5 to 40 A/g (Figure 6.12 (b)). A non-linear GCD profile was obtained as it was expected due to the pseudocapacitive profile of the nanocomposite electrodes. With an increase in current density, ions could not find enough time to diffuse therefore, shorter time for redox reactions was observed from the charge-discharge curves at higher current densities. Specific capacitance values calculated from the GCD curve was 816.7 F/g at a current density of 5 A/g.

Specific capacitance was found to decrease to 661.2 F/g at the current density of 10 A/g and to 290.7 F/g at the current density of 20 A/g. Voltage plateaus on the GCD curves are consistent with the redox peaks in the CV. The second plateau observed around 0.06 V at lower current densities is due to the redox reaction of Ag/Ag⁺ redox couple, which is consistent with the CV curves and previous studies [137], [138].

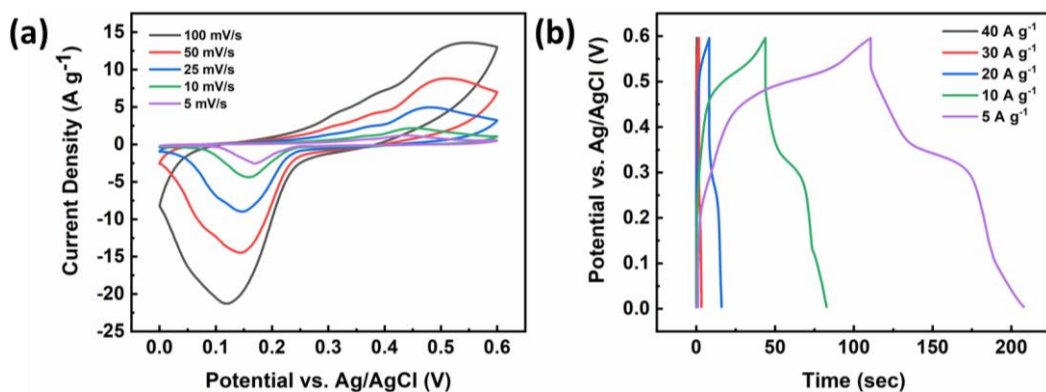


Figure 6.12 (a) CV plots of the Ag-Pt-Ni(OH)₂ nanocomposite electrode in 1 M aqueous KOH electrolyte with scan rates ranging from 100 mV/s to 5 mV/s. (b) GCD curves of Ag-Pt-Ni(OH)₂ electrode at current densities ranging from 40 A g⁻¹ to 5 A g⁻¹.

Lower IR drop was observed for Ag-Pt-Ni(OH)₂ nanocomposite compared to Ag-Ni(OH)₂ indicating lower internal resistance, favourable for energy storage applications. In Figure 6.13 (a), higher charge-discharge time of Ag-Pt-Ni(OH)₂ nanocomposite indicates higher specific capacitance compared to Ag-Ni(OH)₂ electrode. The specific capacitance value of the Ag-Pt-Ni(OH)₂ electrode is larger than that of the Ag-Ni(OH)₂ electrode (110.7 F/g) at 5 A g⁻¹.

Comparison of the electrochemical impedance spectroscopy (EIS) results for Ag-Pt-Ni(OH)₂ and Ag-Ni(OH)₂ electrodes is shown in Figure 6.13 (b). EIS was conducted under a 5 mV AC perturbation within a range of 100 kHz to 100 mHz. Semicircle formation was not observed for Ag-Pt-Ni(OH)₂ electrode, which indicated the high conductivity of the electrode in the high frequency region and low resistance at the electrode-electrolyte interface for the charge transfer process. Due to the pseudocapacitive property of the active material, sharp increase in the low frequency region was observed. Such a sharp inclination in the low frequency region, which is close to the ideal pseudocapacitor behavior, indicated the low diffusion resistance of Ag-Pt-Ni(OH)₂ electrode compared to Ag-Ni(OH)₂ electrode. Therefore, the higher specific capacitance of Ag-Pt-Ni(OH)₂ was due to the low electrical resistance and IR drop with fast charge transfer properties of the electrode.

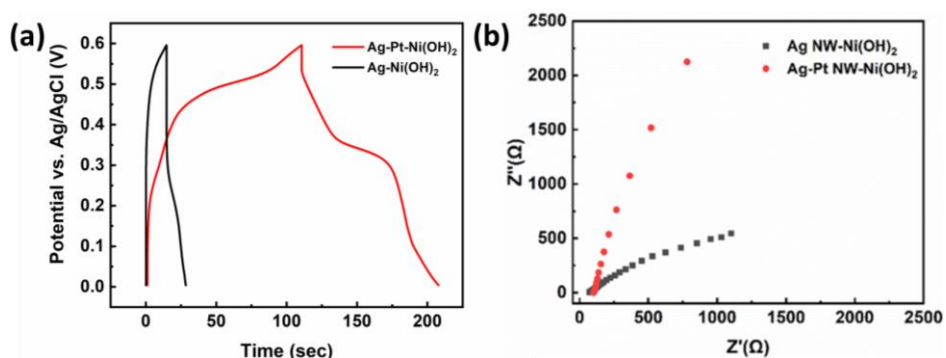


Figure 6.13 (a) Comparison of the GCD curves of Ag-Ni(OH)₂ and Ag-Pt-Ni(OH)₂ electrodes at a current density of 5 A g⁻¹. (b) EIS of Ag-Pt-Ni(OH)₂ and Ag-Ni(OH)₂ electrodes.

Electrochemical stability of the fabricated Ag-Pt core-shell electrodes were studied under different potential windows. Three-electrode measurements were conducted in the potential window of -0.1-0.75 V for Ag-Pt core-shell and bare Ag NW electrodes. Both of the NW networks were coated with a Ni(OH)₂ under same electrodeposition conditions. As shown in Figure 6.14 (a) and (c) higher current densities were observed for the Ag-Pt-Ni(OH)₂ electrode in all scan rates. Larger CV curve area indicates higher capacitance for Ag-Pt-Ni(OH)₂ electrode compared to Ag-Ni(OH)₂ electrode. This results were also supported with the GCD curves in Figure 6.14 (b) and (d). Discharge time was longer for Ag-Pt-Ni(OH)₂ electrode, which provides higher capacitance compared to Ag-Ni(OH)₂.

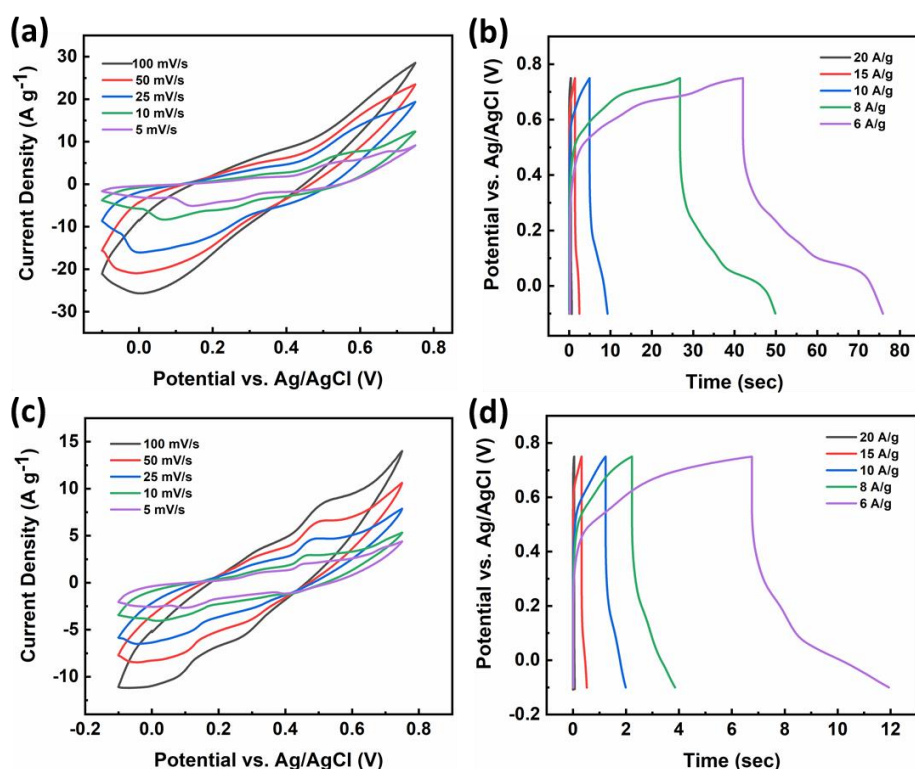


Figure 6.14 CV plots of (a) Ag-Pt-Ni(OH)₂ and (c) Ag-Ni(OH)₂ electrodes in 1 M aqueous KOH electrolyte with scan rates ranging from 100 mV/s to 5 mV/s in the potential window of -0.1-0.75V. GCD curves of (b) Ag-Pt-Ni(OH)₂ and (d) Ag-Ni(OH)₂ electrodes electrode at current densities ranging from 20 A g⁻¹ to 6 A g⁻¹.

Potential window was further increased to -0.3-0.8 V and CV analysis was conducted. Figure 6.15 (a) and (b) shows the CV plots of the Ag-Pt-Ni(OH)₂ and Ag-Ni(OH)₂ electrodes, respectively. Similar to the previous results, higher current densities and curve area was observed for Ag-Pt-Ni(OH)₂ electrode, which provided higher capacitance compared to Ag-Ni(OH)₂ electrode. A comparison of the CV curves at the scan rate of 25 mV/s (Figure 6.15 (c)) clearly shows the improvement of capacitance with the use of a Ag-Pt-Ni(OH)₂ electrode in large potential window.

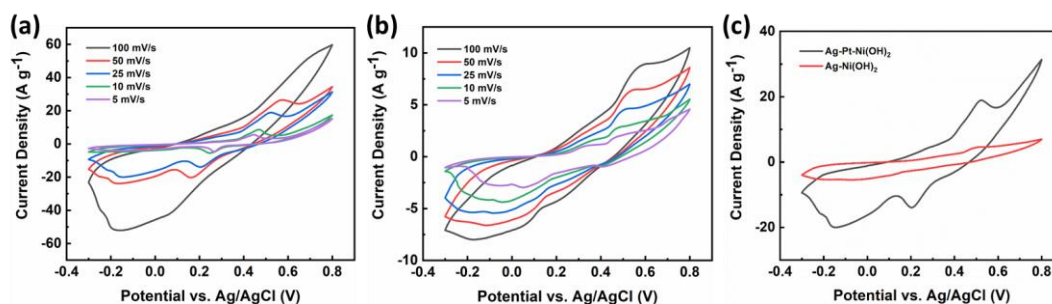


Figure 6.15 CV plots of (a) Ag-Pt-Ni(OH)₂ and (b) Ag-Ni(OH)₂ electrodes with scan rates ranging from 5 mV/s to 100 mV/s, (c) the comparison of Ag-Pt-Ni(OH)₂ (black curve) and Ag-Ni(OH)₂ (red curve) electrodes at the scan rate of 25 mV/s within the potential window of -0.3-0.8V in 1 M aqueous KOH electrolyte.

In all cases for Ag-Pt-Ni(OH)₂ electrodes, current density and CV area was found to increase with the potential window. However, when aqueous electrolytes are used such an increase in the potential window causes electrolyte degradation, which is observed within the potential region of 0.7 to 0.8 V. With the use of aqueous electrolyte, water splitting reactions causes gas evolution, which is highly dependent on the concentration of OH⁻ and H⁺ species in the electrolyte [139]. Such gas evolution also causes bubble formation on the surface of the electrode and prolonged bubble formation on the surface may alter the results of the electrochemical measurements and eventually harm the integrity of the NW network. Therefore, these results also show that the Ag-Pt-Ni(OH)₂ electrodes with enlarged potential window should be utilized with gel electrolyte to get all the benefits, such as enhanced power and energy densities.

CHAPTER 7

CONCLUSIONS AND FUTURE RECOMMENDATIONS

7.1 Conclusions

This work is focused on the simple solution based synthesis of Ag-Pt core-shell NWs and their utilization in electrochemical applications. Detailed characterizations on the Ag-Pt core-shell NWs through SEM, HR-TEM, XPS and XRD analysis evidenced the presence of a conformal Pt layer on Ag NWs. High chemical stability of the Ag-Pt core-shell NWs provided by the conformal Pt shell layer allowed the use of Ag-Pt core-shell NWs for electrochemical applications as demonstrated here through H₂O₂ sensors and supercapacitor electrodes .

High chemical stability of the Ag-Pt core-shell NWs under H₂O₂ exposure (1, 5, 10 mM H₂O₂) compared to that of bare Ag NWs and ability of Ag-Pt core-shell NWs to withstand an applied potential of 0.8 V (vs. Ag/AgCl) showed the superior performance of Ag-Pt core-shell NWs compared to bare Ag NWs for amperometric H₂O₂ detection. Fabricated amperometric H₂O₂ sensor operated with a sensitivity of 0.167 $\mu\text{A}/\mu\text{M}$ in the linear range of 16.11-194.81 μM . Low detection limit of 4.75 μM (S/N=3) and fast response time of 2.44 sec were obtained. Both their high stability against H₂O₂ exposure and their high electrochemical stability provided the fabrication of stable, reproducible and selective amperometric H₂O₂ sensors. In addition to their outstanding performance over bare Ag NW based H₂O₂ sensors, Ag-Pt core-shell NWs based H₂O₂ sensors, with a thin Pt layer, are also promising candidates due to their low fabrication cost over Pt nanostructure based H₂O₂ sensors.

The Ag-Pt core-shell NW networks were also utilized as supercapacitor electrodes. Ni(OH)₂ layer was electrodeposited onto Ag-Pt core-shell NWs to obtain Ag-Pt-Ni(OH)₂ nanocomposite electrodes. A specific capacitance (C_{sp}) of 816.7 F/g at a

current density of 5 A/g was obtained from the fabricated Ag-Pt-Ni(OH)₂ nanocomposite electrodes. Potential window of the Ag-Pt-Ni(OH)₂ electrodes was also widened from 0-0.6 V to -0.3-0.8 V, showing promising electrochemical stability of the electrodes.

Results presented in this work provides a solution for the improvement of the stability of Ag NWs and opens up new avenues for their utilization in electrochemical and optoelectronic devices.

7.2 Future Recommendations

In this work, synthesis route and the use of Ag-Pt core-shell NWs for two different electrochemical applications were presented. Fabricated Ag-Pt core-shell NWs based amperometric sensors provided high sensitivity, selectivity and stability for the detection of H₂O₂. For electrolyte-free, portable and flexible sensors, fabrication and design of the sensor should be further investigated. Afterwards, microsensor design can be employed for the Ag-Pt core-shell NWs to widen their application areas.

High electrocatalytic activity of the Pt shell layer on the core Ag NWs can also be investigated as the electrode materials for hydrogen (HER) and oxygen evolution (OER) applications. Performance of the fabricated Ag-Pt core-shell NWs should be compared to Pt NP decorated Ag NWs to clearly analyze the benefits of the core-shell structure.

For the supercapacitors, high electrochemical stability of the fabricated Ag-Pt core-shell NW electrodes allows deposition of various other pseudocapacitive materials. Under the electrodeposition conditions where Ag NWs fail to operate, Ag-Pt core-shell NWs can be used without any problem. Therefore, electrodeposition of various pseudocapacitive materials such as oxides, hydroxides, sulfides and conducting polymers on Ag-Pt core-shell NWs can be investigated. Based on those different

pseudocapacitive materials, symmetric or asymmetric supercapacitor devices can be fabricated and their electrochemical properties can be investigated.

Although Ag-Pt-Ni(OH)₂ nanocomposite supercapacitor electrodes were investigated in this thesis, there is still extensive work to be conducted on the performance improvement of the electrodes. To determine the best performance of the electrodes, effect of the amount of Ni(OH)₂ deposited, use of different aqueous or gel electrolytes can be further studied.

To increase the specific capacitance by widening the potential window and at the same time to prevent the electrolyte degradation occurring due to the use of aqueous electrolytes at high potentials, an asymmetric supercapacitor based on Ag-Pt-Ni(OH)₂ should be fabricated using a gel electrolyte such as PVA/KOH.

Other electrochemical devices like electrochromics can also be engineered with Ag-Pt core-shell NWs developed in this work.

REFERENCES

- [1] C. Dhand *et al.*, “Methods and strategies for the synthesis of diverse nanoparticles and their applications: A comprehensive overview,” *RSC Adv.*, vol. 5, no. 127, pp. 105003–105037, 2015, doi: 10.1039/c5ra19388e.
- [2] Y. Shi *et al.*, “Synthesis and applications of silver nanowires for transparent conductive films,” *Micromachines*, vol. 10, no. 5, 2019, doi: 10.3390/mi10050330.
- [3] Y. Sun, B. Mayers, T. Herricks, and Y. Xia, “Polyol synthesis of uniform silver nanowires: A plausible growth mechanism and the supporting evidence,” *Nano Lett.*, vol. 3, no. 7, pp. 955–960, 2003, doi: 10.1021/nl034312m.
- [4] F. Fievet, J. P. Lagier, and M. Figlarz, “Preparing Monodisperse Metal Powders in Micrometer and Submicrometer Sizes by the Polyol Process,” *MRS Bull.*, vol. 14, no. 12, pp. 29–34, 1989, doi: 10.1557/S0883769400060930.
- [5] Y. Sun, B. Gates, B. Mayers, and Y. Xia, “Crystalline Silver Nanowires by Soft Solution Processing,” *Nano Lett.*, vol. 2, no. 2, pp. 165–168, 2002, doi: 10.1021/nl010093y.
- [6] P. Zhang *et al.*, “Behind the role of bromide ions in the synthesis of ultrathin silver nanowires,” *Mater. Lett.*, vol. 213, pp. 23–26, 2018, doi: 10.1016/j.matlet.2017.10.128.
- [7] S. Coskun, B. Aksoy, and H. E. Unalan, “Polyol synthesis of silver nanowires: An extensive parametric study,” *Cryst. Growth Des.*, vol. 11, no. 11, pp. 4963–4969, 2011, doi: 10.1021/cg200874g.
- [8] G. Khanarian *et al.*, “The optical and electrical properties of silver nanowire mesh films,” *J. Appl. Phys.*, vol. 114, no. 2, 2013, doi: 10.1063/1.4812390.
- [9] J. Jiu and K. Suganuma, “Metallic nanowires and their application,” *IEEE Trans. Components, Packag. Manuf. Technol.*, vol. 6, no. 12, pp. 1733–

1751, 2016, doi: 10.1109/TCPMT.2016.2581829.

- [10] M. Aeaelj and I. Stanković, “From percolating to dense random stick networks: Conductivity model investigation,” *Phys. Rev. B - Condens. Matter Mater. Phys.*, vol. 86, no. 13, pp. 1–6, 2012, doi: 10.1103/PhysRevB.86.134202.
- [11] M. Lagrange, D. P. Langley, G. Giusti, C. Jiménez, Y. Bréchet, and D. Bellet, “Optimization of silver nanowire-based transparent electrodes: Effects of density, size and thermal annealing,” *Nanoscale*, vol. 7, no. 41, pp. 17410–17423, 2015, doi: 10.1039/c5nr04084a.
- [12] D. P. Langley *et al.*, “Metallic nanowire networks: Effects of thermal annealing on electrical resistance,” *Nanoscale*, vol. 6, no. 22, pp. 13535–13543, 2014, doi: 10.1039/c4nr04151h.
- [13] D. Tigan, S. P. Genlik, B. Imer, and H. E. Unalan, “Core/shell copper nanowire networks for transparent thin film heaters,” *Nanotechnology*, vol. 30, no. 32, 2019, doi: 10.1088/1361-6528/ab19c6.
- [14] C. Sachse, N. Weiß, N. Gaponik, L. Müller-Meskamp, A. Eychmüller, and K. Leo, “ITO-Free, small-molecule organic solar cells on spray-coated copper-nanowire-based transparent electrodes,” *Adv. Energy Mater.*, vol. 4, no. 2, 2014, doi: 10.1002/aenm.201300737.
- [15] J. W. Borchert, I. E. Stewart, S. Ye, A. R. Rathmell, B. J. Wiley, and K. I. Winey, “Effects of length dispersity and film fabrication on the sheet resistance of copper nanowire transparent conductors,” *Nanoscale*, vol. 7, no. 34, pp. 14496–14504, 2015, doi: 10.1039/c5nr03671b.
- [16] T. Tokuno *et al.*, “Fabrication of silver nanowire transparent electrodes at room temperature,” *Nano Res.*, vol. 4, no. 12, pp. 1215–1222, 2011, doi: 10.1007/s12274-011-0172-3.
- [17] J. Lee, I. Lee, T. S. Kim, and J. Y. Lee, “Efficient welding of silver nanowire networks without post-processing,” *Small*, vol. 9, no. 17, pp.

2887–2894, 2013, doi: 10.1002/sml.201203142.

- [18] S. B. Yang, H. K. Choi, D. S. Lee, C. G. Choi, S. Y. Choi, and I. D. Kim, “Improved Optical Sintering Efficiency at the Contacts of Silver Nanowires Encapsulated by a Graphene Layer,” *Small*, vol. 11, no. 11, pp. 1293–1300, 2015, doi: 10.1002/sml.201402474.
- [19] D. J. Lee, Y. Oh, J. M. Hong, Y. W. Park, and B. K. Ju, “Light sintering of ultra-smooth and robust silver nanowire networks embedded in poly(vinylbutyral) for flexible OLED,” *Sci. Rep.*, vol. 8, no. 1, pp. 1–9, 2018, doi: 10.1038/s41598-018-32590-0.
- [20] J. A. Spechler, K. A. Nagamatsu, J. C. Sturm, and C. B. Arnold, “Improved efficiency of hybrid organic photovoltaics by pulsed laser sintering of silver nanowire network transparent electrode,” *ACS Appl. Mater. Interfaces*, vol. 7, no. 19, pp. 10556–10562, 2015, doi: 10.1021/acsami.5b02203.
- [21] G. Deignan and I. A. Goldthorpe, “The dependence of silver nanowire stability on network composition and processing parameters,” *RSC Adv.*, vol. 7, no. 57, pp. 35590–35597, 2017, doi: 10.1039/c7ra06524h.
- [22] C. Kleber, R. Wiesinger, J. Schnöller, U. Hilfrich, H. Hutter, and M. Schreiner, “Initial oxidation of silver surfaces by S₂-and S₄⁺ species,” *Corros. Sci.*, vol. 50, no. 4, pp. 1112–1121, 2008, doi: 10.1016/j.corsci.2007.12.001.
- [23] J. Jiu *et al.*, “The effect of light and humidity on the stability of silver nanowire transparent electrodes,” *RSC Adv.*, vol. 5, no. 35, pp. 27657–27664, 2015, doi: 10.1039/c5ra02722e.
- [24] C. Mayousse, C. Celle, A. Fraczkiewicz, and J. P. Simonato, “Stability of silver nanowire based electrodes under environmental and electrical stresses,” *Nanoscale*, vol. 7, no. 5, pp. 2107–2115, 2015, doi: 10.1039/c4nr06783e.
- [25] I. K. Moon, J. Il Kim, H. Lee, K. Hur, W. C. Kim, and H. Lee, “2D graphene

- oxide nanosheets as an adhesive over-coating layer for flexible transparent conductive electrodes,” *Sci. Rep.*, vol. 3, pp. 1–7, 2013, doi: 10.1038/srep01112.
- [26] J. L. Elechiguerra, L. Larios-Lopez, C. Liu, D. Garcia-Gutierrez, A. Camacho-Bragado, and M. J. Yacaman, “Corrosion at the nanoscale: The case of silver nanowires and nanoparticles,” *Chem. Mater.*, vol. 17, no. 24, pp. 6042–6052, 2005, doi: 10.1021/cm051532n.
- [27] H. H. Khaligh and I. A. Goldthorpe, “Failure of silver nanowire transparent electrodes under current flow,” *Nanoscale Res. Lett.*, vol. 8, no. 1, pp. 2–7, 2013, doi: 10.1186/1556-276x-8-235.
- [28] J. Bang *et al.*, “Advances in protective layer-coating on metal nanowires with enhanced stability and their applications,” *Appl. Mater. Today*, vol. 22, p. 100909, 2021, doi: 10.1016/j.apmt.2020.100909.
- [29] R. Yuksel, S. Coskun, and H. E. Unalan, “Coaxial silver nanowire network core molybdenum oxide shell supercapacitor electrodes,” *Electrochim. Acta*, vol. 193, pp. 39–44, 2016, doi: 10.1016/j.electacta.2016.02.033.
- [30] A. Khan *et al.*, “Stability Enhancement of Silver Nanowire Networks with Conformal ZnO Coatings Deposited by Atmospheric Pressure Spatial Atomic Layer Deposition,” *ACS Appl. Mater. Interfaces*, vol. 10, no. 22, pp. 19208–19217, 2018, doi: 10.1021/acsami.8b03079.
- [31] H. R. Liu *et al.*, “Worm-like Ag/ZnO core-shell heterostructural composites: Fabrication, characterization, and photocatalysis,” *J. Phys. Chem. C*, vol. 116, no. 30, pp. 16182–16190, 2012, doi: 10.1021/jp2115143.
- [32] D. Chen *et al.*, “Thermally Stable Silver Nanowire-Polyimide Transparent Electrode Based on Atomic Layer Deposition of Zinc Oxide on Silver Nanowires,” *Adv. Funct. Mater.*, vol. 25, no. 48, pp. 7512–7520, 2015, doi: 10.1002/adfm.201503236.
- [33] Y. Won *et al.*, “Annealing-free fabrication of highly oxidation-resistant

- copper nanowire composite conductors for photovoltaics,” *NPG Asia Mater.*, vol. 6, no. 6, pp. 1–9, 2014, doi: 10.1038/am.2014.36.
- [34] Z. Chen, S. Ye, I. E. Stewart, and B. J. Wiley, “Copper nanowire networks with transparent oxide shells that prevent oxidation without reducing transmittance,” *ACS Nano*, vol. 8, no. 9, pp. 9673–9679, 2014, doi: 10.1021/nm504308n.
- [35] P. Ramasamy, D. M. Seo, S. H. Kim, and J. Kim, “Effects of TiO₂ shells on optical and thermal properties of silver nanowires,” *J. Mater. Chem.*, vol. 22, no. 23, pp. 11651–11657, 2012, doi: 10.1039/c2jm00010e.
- [36] T. Y. Chen, C. M. Fan, J. Y. Wu, and T. L. Lin, “Hybrid silver nanowire/titanium oxides nanocomposites as anode for dye-sensitized solar cell application,” *J. Chinese Chem. Soc.*, vol. 56, no. 6, pp. 1244–1249, 2009, doi: 10.1002/jccs.200900179.
- [37] D. G. Lee, D. Lee, J. S. Yoo, S. Lee, and H. S. Jung, “Effective passivation of Ag nanowire-based flexible transparent conducting electrode by TiO₂ nanoshell,” *Nano Converg.*, vol. 3, no. 1, 2016, doi: 10.1186/s40580-016-0080-z.
- [38] Y. Huang *et al.*, “TiO₂-Coated Core-Shell Ag Nanowire Networks for Robust and Washable Flexible Transparent Electrodes,” *ACS Appl. Nano Mater.*, vol. 2, no. 4, pp. 2456–2466, 2019, doi: 10.1021/acsanm.9b00337.
- [39] B. Sciacca, S. A. Mann, F. D. Tichelaar, H. W. Zandbergen, M. A. Van Huis, and E. C. Garnett, “Solution-phase epitaxial growth of quasi-monocrystalline cuprous oxide on metal nanowires,” *Nano Lett.*, vol. 14, no. 10, pp. 5891–5898, 2014, doi: 10.1021/nl502831t.
- [40] Z. Gao, H. Wang, Z. Cao, T. Zhou, C. An, and Y. Zhao, “Silver Nanowires@Mn₃O₄ Core-Shell Nanocables as Advanced Electrode Materials for Aqueous Asymmetric Supercapacitors,” *Energy Technol.*, vol. 5, no. 12, pp. 2275–2282, 2017, doi: 10.1002/ente.201700327.

- [41] B. Hwang *et al.*, “Highly Flexible and Transparent Ag Nanowire Electrode Encapsulated with Ultra-Thin Al₂O₃: Thermal, Ambient, and Mechanical Stabilities,” *Sci. Rep.*, vol. 7, no. October 2016, pp. 1–7, 2017, doi: 10.1038/srep41336.
- [42] C. Celle *et al.*, “Oxidation of copper nanowire based transparent electrodes in ambient conditions and their stabilization by encapsulation: Application to transparent film heaters,” *Nanotechnology*, vol. 29, no. 8, 2018, doi: 10.1088/1361-6528/aaa48e.
- [43] K. L. Zhou *et al.*, “Electrochromic modulation of near-infrared light by WO₃ films deposited on silver nanowire substrates,” *J. Mater. Sci.*, vol. 52, no. 21, pp. 12783–12794, 2017, doi: 10.1007/s10853-017-1391-0.
- [44] S. Vlassov *et al.*, “Shape restoration effect in Ag-SiO₂ core-shell nanowires,” *Nano Lett.*, vol. 14, no. 9, pp. 5201–5205, 2014, doi: 10.1021/nl5019063.
- [45] P. F. Flowers, M. J. Catenacci, and B. J. Wiley, “High-speed, solution-coatable memory based on Cu-SiO₂ core-shell nanowires,” *Nanoscale Horizons*, vol. 1, no. 4, pp. 313–316, 2016, doi: 10.1039/c6nh00020g.
- [46] R. Yuksel, S. Coskun, Y. E. Kalay, and H. E. Unalan, “Flexible, silver nanowire network nickel hydroxide core-shell electrodes for supercapacitors,” *J. Power Sources*, vol. 328, pp. 167–173, 2016, doi: 10.1016/j.jpowsour.2016.08.008.
- [47] H. Du *et al.*, “Silver nanowire/nickel hydroxide nanosheet composite for a transparent electrode and all-solid-state supercapacitor,” *Nanoscale Adv.*, vol. 1, no. 1, pp. 140–146, 2019, doi: 10.1039/c8na00110c.
- [48] L. Li, K. S. Hui, K. N. Hui, T. Zhang, J. Fu, and Y. R. Cho, “High-performance solid-state flexible supercapacitor based on reduced graphene oxide/hierarchical core-shell Ag nanowire@NiAl layered double hydroxide film electrode,” *Chem. Eng. J.*, vol. 348, no. February, pp. 338–349, 2018, doi: 10.1016/j.cej.2018.04.164.

- [49] S. Wu, K. S. Hui, and K. N. Hui, "One-Dimensional Core-Shell Architecture Composed of Silver Nanowire@Hierarchical Nickel-Aluminum Layered Double Hydroxide Nanosheet as Advanced Electrode Materials for Pseudocapacitor," *J. Phys. Chem. C*, vol. 119, no. 41, pp. 23358–23365, 2015, doi: 10.1021/acs.jpcc.5b07739.
- [50] J. Liu *et al.*, "A one-dimensional Ag NW@NiCo/NiCo(OH)₂ core-shell nanostructured electrode for a flexible and transparent asymmetric supercapacitor," *J. Mater. Chem. A*, vol. 7, no. 14, pp. 8184–8193, 2019, doi: 10.1039/c9ta01303b.
- [51] J. Xu *et al.*, "Preparation of one dimensional silver nanowire/nickel-cobalt layered double hydroxide and its electrocatalysis of glucose," *J. Electroanal. Chem.*, vol. 823, no. April, pp. 315–321, 2018, doi: 10.1016/j.jelechem.2018.06.028.
- [52] W. Alshammari, D. S. Patil, S. A. Pawar, and J. C. Shin, "Silver nanowires-copper sulfide core/shell nanostructure for electrochemical supercapacitors," *Mater. Today Chem.*, vol. 5, pp. 72–80, 2017, doi: 10.1016/j.mtchem.2017.07.004.
- [53] J. Liu *et al.*, "Electrophoresis deposition of flexible and transparent silver nanowire/graphene composite film and its electrochemical properties," *J. Alloys Compd.*, vol. 745, pp. 370–377, 2018, doi: 10.1016/j.jallcom.2018.02.241.
- [54] R. Chen, S. R. Das, C. Jeong, M. R. Khan, D. B. Janes, and M. A. Alam, "Co-percolating graphene-wrapped silver nanowire network for high performance, highly stable, transparent conducting electrodes," *Adv. Funct. Mater.*, vol. 23, no. 41, pp. 5150–5158, 2013, doi: 10.1002/adfm.201300124.
- [55] D. S. Patil, S. A. Pawar, P. S. Patil, and J. C. Shin, "Improved electrochemical performance of sandwich-like silver nanowires/graphene oxide nanostructure," *J. Appl. Electrochem.*, vol. 47, no. 4, pp. 487–496, 2017, doi: 10.1007/s10800-017-1053-6.

- [56] S. M. Li *et al.*, “Fabrication of a silver nanowire-reduced graphene oxide-based electrochemical biosensor and its enhanced sensitivity in the simultaneous determination of ascorbic acid, dopamine, and uric acid,” *J. Mater. Chem. C*, vol. 3, no. 36, pp. 9444–9453, 2015, doi: 10.1039/c5tc01564b.
- [57] C. S. Lee, J. E. Yoo, K. Shin, C. O. Park, and J. Bae, “Carbon nanotube-silver nanowire composite networks on flexible substrates: High reliability and application for supercapacitor electrodes,” *Phys. Status Solidi Appl. Mater. Sci.*, vol. 211, no. 12, pp. 2890–2897, 2014, doi: 10.1002/pssa.201431538.
- [58] S. J. Lee *et al.*, “SWCNT–Ag nanowire composite for transparent stretchable film heater with enhanced electrical stability,” *J. Mater. Sci.*, vol. 53, no. 17, pp. 12284–12294, 2018, doi: 10.1007/s10853-018-2526-7.
- [59] I. K. Moon, S. Yoon, and J. Oh, “3D Highly Conductive Silver Nanowire@PEDOT:PSS Composite Sponges for Flexible Conductors and Their All-Solid-State Supercapacitor Applications,” *Adv. Mater. Interfaces*, vol. 4, no. 22, pp. 1–8, 2017, doi: 10.1002/admi.201700860.
- [60] D. S. Patil, S. A. Pawar, J. H. Kim, P. S. Patil, and J. C. Shin, “Facile Preparation and Enhanced Capacitance of the Ag-PEDOT:PSS/Polyaniline Nanofiber Network for Supercapacitors,” *Electrochim. Acta*, vol. 213, pp. 680–690, 2016, doi: 10.1016/j.electacta.2016.07.156.
- [61] Z. Yu, C. Li, D. Abbitt, and J. Thomas, “Flexible, sandwich-like Ag-nanowire/PEDOT:PSS-nanopillar/MnO₂ high performance supercapacitors,” *J. Mater. Chem. A*, vol. 2, no. 28, pp. 10923–10929, 2014, doi: 10.1039/c4ta01245c.
- [62] M. A. Shinde and H. Kim, “Flexible electrochromic device with simple solution processed stable silver: Nanowire based transparent conductive electrodes,” *Synth. Met.*, vol. 254, no. June, pp. 97–105, 2019, doi: 10.1016/j.synthmet.2019.05.017.

- [63] J. Park, D. Han, S. Choi, Y. Kim, and J. Kwak, "Flexible transparent film heaters using a ternary composite of silver nanowire, conducting polymer, and conductive oxide," *RSC Adv.*, vol. 9, no. 10, pp. 5731–5737, 2019, doi: 10.1039/c9ra00341j.
- [64] R. Yuksel, E. Alpugan, and H. E. Unalan, "Coaxial silver nanowire/polypyrrole nanocomposite supercapacitors," *Org. Electron.*, vol. 52, no. August 2017, pp. 272–280, 2018, doi: 10.1016/j.orgel.2017.10.012.
- [65] C. Zhang, S. Govindaraju, K. Giribabu, Y. S. Huh, and K. Yun, "AgNWs-PANI nanocomposite based electrochemical sensor for detection of 4-nitrophenol," *Sensors Actuators, B Chem.*, vol. 252, pp. 616–623, 2017, doi: 10.1016/j.snb.2017.06.039.
- [66] A. B. V. K. Kumar, J. Jiang, C. W. Bae, D. M. Seo, L. Piao, and S. H. Kim, "Silver nanowire/polyaniline composite transparent electrode with improved surface properties," *Mater. Res. Bull.*, vol. 57, pp. 52–57, 2014, doi: 10.1016/j.materresbull.2014.05.031.
- [67] H. Kim, J. Yeo, and S. H. Ko, "Highly Stretchable and Transparent Supercapacitor by Ag – Au Core – Shell Nanowire Network with High Electrochemical Stability," 2016, doi: 10.1021/acsami.6b04364.
- [68] H. Moon, H. Lee, J. Kwon, Y. D. Suh, and D. K. Kim, "Ag / Au / Polypyrrole Core-shell Nanowire Network for Transparent , Stretchable and Flexible Supercapacitor in Wearable Energy Devices," no. February, pp. 1–10, 2017, doi: 10.1038/srep41981.
- [69] M. Yang, Z. D. Hood, X. Yang, M. Chi, and Y. Xia, "Facile synthesis of Ag@Au core-sheath nanowires with greatly improved stability against oxidation," *Chem. Commun.*, vol. 53, no. 12, pp. 1965–1968, 2017, doi: 10.1039/c6cc09878a.
- [70] Y. L. Shen, S. Y. Chen, J. M. Song, and I. G. Chen, "Kinetic study of Pt nanocrystal deposition on Ag nanowires with clean surfaces via galvanic replacement," *Nanoscale Res. Lett.*, vol. 7, pp. 1–7, 2012, doi:

10.1186/1556-276X-7-245.

- [71] S. Park, A. W. M. Tan, J. Wang, and P. S. Lee, “Coaxial Ag-base metal nanowire networks with high electrochemical stability for transparent and stretchable asymmetric supercapacitors,” *Nanoscale Horizons*, vol. 2, no. 4, pp. 199–204, 2017, doi: 10.1039/c7nh00024c.
- [72] S. Wojtysiak, J. Solla-gullón, P. Dłu, and A. Kudelski, “Colloids and Surfaces A : Physicochemical and Engineering Aspects Synthesis of core – shell silver – platinum nanoparticles , improving shell integrity,” vol. 441, pp. 178–183, 2014.
- [73] Y. Yang, J. Liu, Z. W. Fu, and D. Qin, “Galvanic replacement-free deposition of au on ag for core-shell nanocubes with enhanced chemical stability and SERS activity,” *J. Am. Chem. Soc.*, vol. 136, no. 23, pp. 8153–8156, 2014, doi: 10.1021/ja502472x.
- [74] N. Murshid, I. Gourevich, N. Coombs, and V. Kitaev, “Gold plating of silver nanoparticles for superior stability and preserved plasmonic and sensing properties,” *Chem. Commun.*, vol. 49, no. 97, pp. 11355–11357, 2013, doi: 10.1039/c3cc46075d.
- [75] T. Fu, J. Fang, C. Wang, and J. Zhao, “Hollow porous nanoparticles with Pt skin on a Ag-Pt alloy structure as a highly active electrocatalyst for the oxygen reduction reaction,” *J. Mater. Chem. A*, vol. 4, no. 22, pp. 8803–8811, 2016, doi: 10.1039/c6ta02202b.
- [76] I. E. Stewart, S. Ye, Z. Chen, P. F. Flowers, and B. J. Wiley, “Synthesis of Cu – Ag , Cu – Au , and Cu – Pt Core – Shell Nanowires and Their Use in Transparent Conducting Films,” 2015, doi: 10.1021/acs.chemmater.5b03709.
- [77] C. Li and Y. Yamauchi, “Facile solution synthesis of Ag@Pt core-shell nanoparticles with dendritic Pt shells,” *Phys. Chem. Chem. Phys.*, vol. 15, no. 10, pp. 3490–3496, 2013, doi: 10.1039/c3cp44313b.

- [78] E. Sumesh, M. S. Bootharaju, Anshup, and T. Pradeep, "A practical silver nanoparticle-based adsorbent for the removal of Hg²⁺ from water," *J. Hazard. Mater.*, vol. 189, no. 1–2, pp. 450–457, 2011, doi: 10.1016/j.jhazmat.2011.02.061.
- [79] Z. Huang *et al.*, "Continuous synthesis of size-tunable silver nanoparticles by a green electrolysis method and multi-electrode design for high yield," *J. Mater. Chem. A*, vol. 3, no. 5, pp. 1925–1929, 2015, doi: 10.1039/c4ta06782g.
- [80] B. Xi, Y. C. Tan, and H. C. Zeng, "A General Synthetic Approach for Integrated Nanocatalysts of Metal-Silica@ZIFs," *Chem. Mater.*, vol. 28, no. 1, pp. 326–336, 2016, doi: 10.1021/acs.chemmater.5b04147.
- [81] D. Lützenkirchen-Hecht and H. H. Strehblow, "Anodic silver (II) oxides investigated by combined electrochemistry, ex situ XPS and in situ X-ray absorption spectroscopy," *Surf. Interface Anal.*, vol. 41, no. 10, pp. 820–829, 2009, doi: 10.1002/sia.3106.
- [82] N. J. Ronkainen, H. B. Halsall, and W. R. Heineman, "Electrochemical biosensors," *Chem. Soc. Rev.*, vol. 39, no. 5, pp. 1747–1763, 2010, doi: 10.1039/b714449k.
- [83] X. Yang, J. Bai, Y. Wang, X. Jiang, and X. He, "Hydrogen peroxide and glucose biosensor based on silver nanowires synthesized by polyol process," *Analyst*, vol. 137, no. 18, pp. 4362–4367, 2012, doi: 10.1039/c2an35407a.
- [84] E. Kurowska, A. Brzózka, M. Jarosz, G. D. Sulka, and M. Jaskuła, "Silver nanowire array sensor for sensitive and rapid detection of H₂O₂," *Electrochim. Acta*, vol. 104, pp. 439–447, 2013, doi: 10.1016/j.electacta.2013.01.077.
- [85] R. D. Abdel- Rahim, M. Y. Emran, A. M. Naguib, O. A. Farghaly, and M. A. Taher, "Silver nanowire size- dependent effect on the catalytic activity and potential sensing of H₂O₂," *Electrochem. Sci. Adv.*, no. October, pp. 1–12, 2020, doi: 10.1002/elsa.202000031.

- [86] K. Habermüller, M. Mosbach, and W. Schuhmann, "Electron-transfer mechanisms in amperometric biosensors," *Fresenius. J. Anal. Chem.*, vol. 366, no. 6–7, pp. 560–568, 2000, doi: 10.1007/s002160051551.
- [87] J. H. Han, E. Lee, S. Park, R. Chang, and T. D. Chung, "Effect of nanoporous structure on enhanced electrochemical reaction," *J. Phys. Chem. C*, vol. 114, no. 21, pp. 9546–9553, 2010, doi: 10.1021/jp909382b.
- [88] M. Kesik *et al.*, "A functional immobilization matrix based on a conducting polymer and functionalized gold nanoparticles: Synthesis and its application as an amperometric glucose biosensor," *Polymer (Guildf.)*, vol. 54, no. 17, pp. 4463–4471, 2013, doi: 10.1016/j.polymer.2013.06.050.
- [89] R. A. Sheldon, "Enzyme immobilization: The quest for optimum performance," *Adv. Synth. Catal.*, vol. 349, no. 8–9, pp. 1289–1307, 2007, doi: 10.1002/adsc.200700082.
- [90] C. Garcia-Galan, Á. Berenguer-Murcia, R. Fernandez-Lafuente, and R. C. Rodrigues, "Potential of different enzyme immobilization strategies to improve enzyme performance," *Adv. Synth. Catal.*, vol. 353, no. 16, pp. 2885–2904, 2011, doi: 10.1002/adsc.201100534.
- [91] G. Bharath *et al.*, "Enzymatic electrochemical glucose biosensors by mesoporous 1D hydroxyapatite-on-2D reduced graphene oxide," *J. Mater. Chem. B*, vol. 3, no. 7, pp. 1360–1370, 2015, doi: 10.1039/c4tb01651c.
- [92] L. Wang, X. Gao, L. Jin, Q. Wu, Z. Chen, and X. Lin, "Amperometric glucose biosensor based on silver nanowires and glucose oxidase," *Sensors Actuators, B Chem.*, vol. 176, pp. 9–14, 2013, doi: 10.1016/j.snb.2012.08.077.
- [93] Y. Lu, M. Yang, F. Qu, G. Shen, and R. Yu, "Enzyme-functionalized gold nanowires for the fabrication of biosensors," *Bioelectrochemistry*, vol. 71, no. 2, pp. 211–216, 2007, doi: 10.1016/j.bioelechem.2007.05.003.
- [94] X. Yang, Y. Wang, Y. Liu, and X. Jiang, "A sensitive hydrogen peroxide

- and glucose biosensor based on gold/silver core-shell nanorods,” *Electrochim. Acta*, vol. 108, pp. 39–44, 2013, doi: 10.1016/j.electacta.2013.06.017.
- [95] S. G. Leonardi *et al.*, “Amperometric Sensing of H₂O₂ using Pt-TiO₂/Reduced Graphene Oxide Nanocomposites,” *ChemElectroChem*, vol. 1, no. 3, pp. 617–624, 2014, doi: 10.1002/celec.201300106.
- [96] S. Liu, J. Tian, L. Wang, and X. Sun, “Microwave-assisted rapid synthesis of Ag nanoparticles/graphene nanosheet composites and their application for hydrogen peroxide detection,” *J. Nanoparticle Res.*, vol. 13, no. 10, pp. 4539–4548, 2011, doi: 10.1007/s11051-011-0410-3.
- [97] A. M. Noor, M. M. Shahid, P. Rameshkumar, and N. M. Huang, “A glassy carbon electrode modified with graphene oxide and silver nanoparticles for amperometric determination of hydrogen peroxide,” *Microchim. Acta*, vol. 183, no. 2, pp. 911–916, 2016, doi: 10.1007/s00604-015-1679-1.
- [98] S. Liu, J. Tian, L. Wang, H. Li, Y. Zhang, and X. Sun, “Stable aqueous dispersion of graphene nanosheets: Noncovalent functionalization by a polymeric reducing agent and their subsequent decoration with Ag nanoparticles for enzymeless hydrogen peroxide detection,” *Macromolecules*, vol. 43, no. 23, pp. 10078–10083, 2010, doi: 10.1021/ma102230m.
- [99] J. Tian, S. Liu, and X. Sun, “Supramolecular microfibrils of o-phenylenediamine dimers: Oxidation-induced morphology change and the spontaneous formation of Ag nanoparticle decorated nanofibers,” *Langmuir*, vol. 26, no. 19, pp. 15112–15116, 2010, doi: 10.1021/la103038m.
- [100] W. H. Hsiao *et al.*, “Urchin-like Ag nanowires as non-enzymatic hydrogen peroxide sensor,” *J. Chinese Chem. Soc.*, vol. 59, no. 4, pp. 500–506, 2012, doi: 10.1002/jccs.201100500.
- [101] S. Guo and E. Wang, “Noble metal nanomaterials: Controllable synthesis and application in fuel cells and analytical sensors,” *Nano Today*, vol. 6, no.

- 3, pp. 240–264, 2011, doi: 10.1016/j.nantod.2011.04.007.
- [102] E. Sitta, A. M. Gómez-Marín, A. Aldaz, and J. M. Feliu, “Electrocatalysis of H₂O₂ reduction/oxidation at model platinum surfaces,” *Electrochem. commun.*, vol. 33, pp. 39–42, 2013, doi: 10.1016/j.elecom.2013.04.014.
- [103] W. Jia *et al.*, “Electrocatalytic oxidation and reduction of H₂O₂ on vertically aligned Co₃O₄ nanowalls electrode: Toward H₂O₂ detection,” *J. Electroanal. Chem.*, vol. 625, no. 1, pp. 27–32, 2009, doi: 10.1016/j.jelechem.2008.09.020.
- [104] I. Katsounaros *et al.*, “Hydrogen peroxide electrochemistry on platinum: Towards understanding the oxygen reduction reaction mechanism,” *Phys. Chem. Chem. Phys.*, vol. 14, no. 20, pp. 7384–7391, 2012, doi: 10.1039/c2cp40616k.
- [105] Y. Yang, R. Fu, J. Yuan, S. Wu, J. Zhang, and H. Wang, “Highly sensitive hydrogen peroxide sensor based on a glassy carbon electrode modified with platinum nanoparticles on carbon nanofiber heterostructures,” *Microchim. Acta*, vol. 182, no. 13–14, pp. 2241–2249, 2015, doi: 10.1007/s00604-015-1558-9.
- [106] S. He, Z. Chen, Y. Yu, and L. Shi, “A novel non-enzymatic hydrogen peroxide sensor based on poly-melamine film modified with platinum nanoparticles,” *RSC Adv.*, vol. 4, no. 85, pp. 45185–45190, 2014, doi: 10.1039/c4ra06925k.
- [107] Q. M. Wang, H. L. Niu, C. J. Mao, J. M. Song, and S. Y. Zhang, “Facile synthesis of trilaminar core-shell Ag@C@Ag nanospheres and their application for H₂O₂ detection,” *Electrochim. Acta*, vol. 127, pp. 349–354, 2014, doi: 10.1016/j.electacta.2014.02.051.
- [108] Y. Zhou, G. Yu, F. Chang, B. Hu, and C. J. Zhong, “Gold-platinum alloy nanowires as highly sensitive materials for electrochemical detection of hydrogen peroxide,” *Anal. Chim. Acta*, vol. 757, pp. 56–62, 2012, doi: 10.1016/j.aca.2012.10.036.

- [109] Y. Zhang, Y. Li, Y. Jiang, Y. Li, and S. Li, “The synthesis of Au@C@Pt core-double shell nanocomposite and its application in enzyme-free hydrogen peroxide sensing,” *Appl. Surf. Sci.*, vol. 378, pp. 375–383, 2016, doi: 10.1016/j.apsusc.2016.04.001.
- [110] S. Koylan, “Solution-Based Synthesis Of Silver-Platinum Core-Shell Nanowires With Enhanced Stability,” Middle East Technical University, 2019.
- [111] S. Koylan *et al.*, “Highly Stable Silver-Platinum Core-Shell Nanowires for H₂O₂ Detection,” *Nanoscale*, 2021, doi: 10.1039/D1NR01976G.
- [112] A. González, E. Goikolea, J. A. Barrena, and R. Mysyk, “Review on supercapacitors: Technologies and materials,” *Renew. Sustain. Energy Rev.*, vol. 58, pp. 1189–1206, 2016, doi: 10.1016/j.rser.2015.12.249.
- [113] P. Simon and Y. Gogotsi, “Perspectives for electrochemical capacitors and related devices,” *Nat. Mater.*, vol. 19, no. 11, pp. 1151–1163, 2020, doi: 10.1038/s41563-020-0747-z.
- [114] M. Salanne *et al.*, “Efficient storage mechanisms for building better supercapacitors,” *Nat. Energy*, vol. 1, no. 6, 2016, doi: 10.1038/nenergy.2016.70.
- [115] P. Simon, “Simon2009,” *Nat. Mater.*, vol. 7, pp. 845–854, 2008.
- [116] A. Muzaffar, M. B. Ahamed, K. Deshmukh, and J. Thirumalai, “A review on recent advances in hybrid supercapacitors: Design, fabrication and applications,” *Renew. Sustain. Energy Rev.*, vol. 101, no. November 2018, pp. 123–145, 2019, doi: 10.1016/j.rser.2018.10.026.
- [117] J. Libich, J. Máca, J. Vondrák, O. Čech, and M. Sedlářiková, “Supercapacitors: Properties and applications,” *J. Energy Storage*, vol. 17, no. March, pp. 224–227, 2018, doi: 10.1016/j.est.2018.03.012.
- [118] G. Yu, X. Xie, L. Pan, Z. Bao, and Y. Cui, “Hybrid nanostructured materials for high-performance electrochemical capacitors,” *Nano Energy*, vol. 2, no.

- 2, pp. 213–234, 2013, doi: 10.1016/j.nanoen.2012.10.006.
- [119] M. Horn, J. MacLeod, M. Liu, J. Webb, and N. Motta, “Supercapacitors: A new source of power for electric cars?,” *Econ. Anal. Policy*, vol. 61, pp. 93–103, 2019, doi: 10.1016/j.eap.2018.08.003.
- [120] L. Zhang, X. Hu, Z. Wang, F. Sun, and D. G. Dorrell, “A review of supercapacitor modeling, estimation, and applications: A control/management perspective,” *Renew. Sustain. Energy Rev.*, vol. 81, no. June 2017, pp. 1868–1878, 2018, doi: 10.1016/j.rser.2017.05.283.
- [121] P. Simon, Y. Gogotsi, and B. Dunn, “and Supercapacitors Begin?,” *Science (80-.)*, vol. 343, no. March, pp. 1210–1211, 2014.
- [122] T. S. Mathis, N. Kurra, X. Wang, D. Pinto, P. Simon, and Y. Gogotsi, “Energy Storage Data Reporting in Perspective—Guidelines for Interpreting the Performance of Electrochemical Energy Storage Systems,” *Adv. Energy Mater.*, vol. 9, no. 39, 2019, doi: 10.1002/aenm.201902007.
- [123] W. Wei, X. Cui, W. Chen, and D. G. Ivey, “Manganese oxide-based materials as electrochemical supercapacitor electrodes,” *Chem. Soc. Rev.*, vol. 40, no. 3, pp. 1697–1721, 2011, doi: 10.1039/c0cs00127a.
- [124] Y. Wang *et al.*, “Maximized Energy Density of RuO₂//RuO₂ Supercapacitors through Potential Dependence of Specific Capacitance,” *ChemElectroChem*, vol. 7, no. 4, pp. 928–936, 2020, doi: 10.1002/celec.201901898.
- [125] C. Guan *et al.*, “Iron oxide-decorated carbon for supercapacitor anodes with ultrahigh energy density and outstanding cycling stability,” *ACS Nano*, vol. 9, no. 5, pp. 5198–5207, 2015, doi: 10.1021/acsnano.5b00582.
- [126] H. B. Li *et al.*, “Amorphous nickel hydroxide nanospheres with ultrahigh capacitance and energy density as electrochemical pseudocapacitor materials,” *Nat. Commun.*, vol. 4, no. May, pp. 1–7, 2013, doi: 10.1038/ncomms2932.

- [127] X. Xiong *et al.*, “Three-dimensional ultrathin Ni(OH)₂ nanosheets grown on nickel foam for high-performance supercapacitors,” *Nano Energy*, vol. 11, pp. 154–161, 2015, doi: 10.1016/j.nanoen.2014.10.029.
- [128] H. Wang, H. Yi, X. Chen, and X. Wang, “Facile synthesis of a nanostructured nickel oxide electrode with outstanding pseudocapacitive properties,” *Electrochim. Acta*, vol. 105, pp. 353–361, 2013, doi: 10.1016/j.electacta.2013.05.031.
- [129] A. Eftekhari, L. Li, and Y. Yang, “Polyaniline supercapacitors,” *J. Power Sources*, vol. 347, pp. 86–107, 2017, doi: 10.1016/j.jpowsour.2017.02.054.
- [130] Y. Huang *et al.*, “Nanostructured Polypyrrole as a flexible electrode material of supercapacitor,” *Nano Energy*, vol. 22, pp. 422–438, 2016, doi: 10.1016/j.nanoen.2016.02.047.
- [131] H. Zhang, H. Li, F. Zhang, J. Wang, Z. Wang, and S. Wang, “Polyaniline nanofibers prepared by a facile electrochemical approach and their supercapacitor performance,” *J. Mater. Res.*, vol. 23, no. 9, pp. 2326–2332, 2008, doi: 10.1557/jmr.2008.0304.
- [132] B. K. Kim, S. Sy, A. Yu, and J. Zhang, “Electrochemical Supercapacitors for Energy Storage and Conversion,” *Handb. Clean Energy Syst.*, pp. 1–25, 2015, doi: 10.1002/9781118991978.hces112.
- [133] P. Yang and W. Mai, “Flexible solid-state electrochemical supercapacitors,” *Nano Energy*, vol. 8, pp. 274–290, 2014, doi: 10.1016/j.nanoen.2014.05.022.
- [134] J. P. Diard, B. Le Gorrec, and C. Montella, “Linear diffusion impedance. General expression and applications,” *J. Electroanal. Chem.*, vol. 471, no. 2, pp. 126–131, 1999, doi: 10.1016/S0022-0728(99)00262-4.
- [135] D. Zhu *et al.*, “A 2D metal-organic framework/Ni(OH)₂ heterostructure for an enhanced oxygen evolution reaction,” *Nanoscale*, vol. 11, no. 8, pp. 3599–3605, 2019, doi: 10.1039/c8nr09680e.
- [136] W. He, X. Li, S. An, T. Li, Y. Zhang, and J. Cui, “3D β-Ni(OH)₂

nanowires/RGO composite prepared by phase transformation method for superior electrochemical performance,” *Sci. Rep.*, vol. 9, no. 1, pp. 1–8, 2019, doi: 10.1038/s41598-019-47120-9.

- [137] S. Lv *et al.*, “In situ construction of Ag/Ni(OH)₂ composite electrode by combining electroless deposition technology with electrodeposition,” *Metals (Basel)*, vol. 9, no. 8, 2019, doi: 10.3390/met9080826.
- [138] M. Usman, L. Pan, A. Sohail, Z. Mahmood, and R. Cui, “Fabrication of 3D vertically aligned silver nanoplates on nickel foam-graphene substrate by a novel electrodeposition with sonication for efficient supercapacitors,” *Chem. Eng. J.*, vol. 311, pp. 359–366, 2017, doi: 10.1016/j.cej.2016.11.105.
- [139] A. Kang *et al.*, “Tracking Compression Changes in an Aqueous Electrolyte for Real-Time H₂ and O₂ Gas Evolution Quantification during Total Water Splitting Using BARDS,” *ACS Appl. Energy Mater.*, vol. 3, no. 2, pp. 2000–2009, 2020, doi: 10.1021/acsaem.9b02436.

APPENDICES

A. Electrodeposition of Ni(OH)₂ on NW Networks

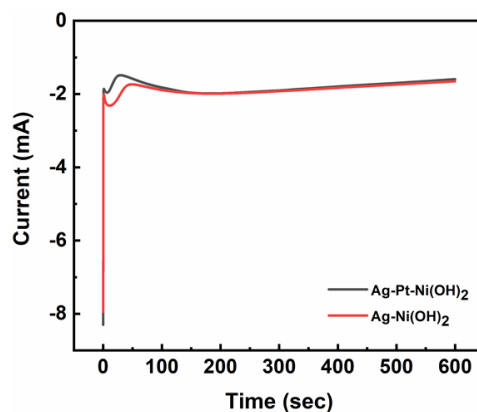


Figure A. 1 Chronoamperometry curve for the electrodeposition of Ni(OH)₂ on Ag-Pt core-shell NW (black) and bare Ag NW (red) networks.

B. Symmetric Supercapacitor

A symmetric supercapacitor (SC) was fabricated using a two electrode setup configuration. A polyvinyl alcohol/potassium hydroxide (PVA/KOH) gel electrolyte was fabricated and two identical Ag-Pt-Ni(OH)₂ electrodes were sandwiched together via PVA/KOH gel electrolyte. A specific capacitance of 1373.9 mF/g was calculated at the scan rate of 5 mV/s.

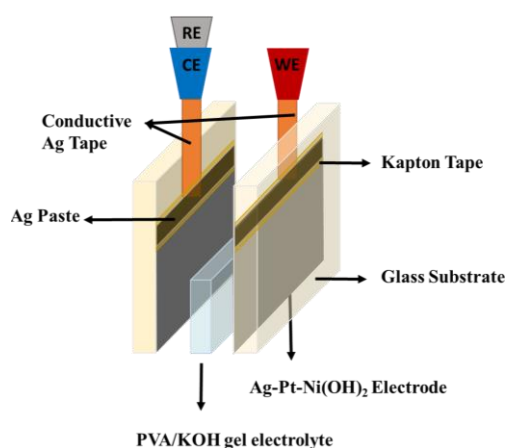


Figure B. 1 Two electrode setup for a symmetric full device.

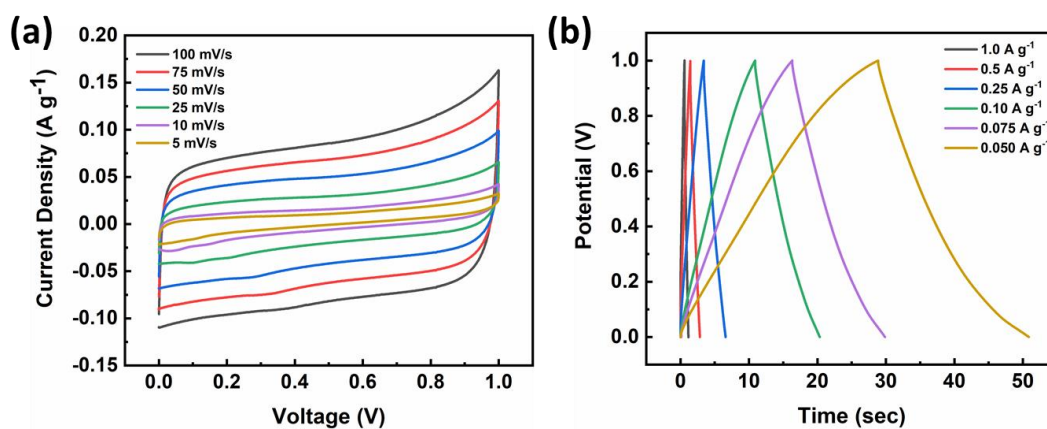


Figure B. 2 (a) CV plots of the Ag-Pt-Ni(OH)₂ nanocomposite supercapacitor with scan rates from 100 mV/s to 5 mV/s. (b) GCD curves of the symmetric device of Ag-Pt-Ni(OH)₂ nanocomposite at current densities ranging from 1 A g⁻¹ to 0.05 A g⁻¹.

Fabricated Ag-Pt-Ni(OH)₂ SC exhibited a Specific capacitance of 757.2, 802.4, 855.0 and 942.6 mF/g when the potential window was widened upto 1.1, 1.2 1.3 and 1.4 V, respectively. A capacitance retention of 98.7 % was observed upon 2000 cycles of CV.

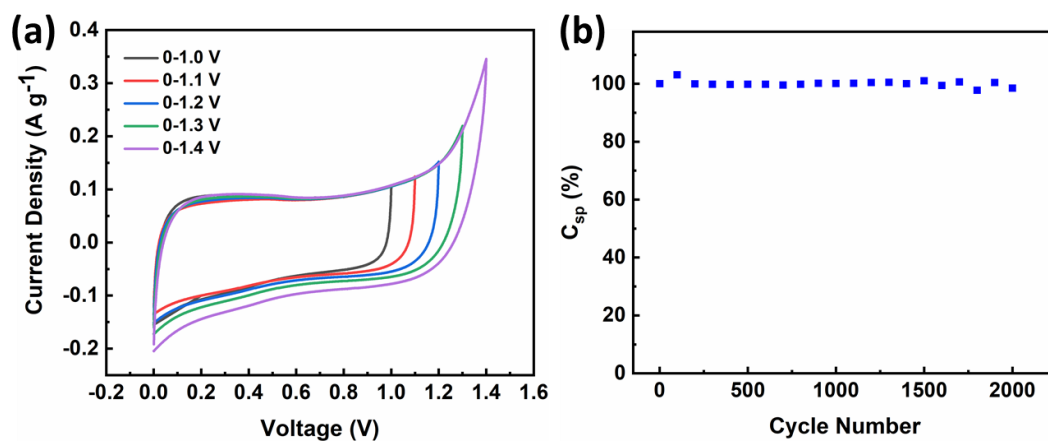


Figure B. 3 (a) The CV curves of Ag-Ni(OH)₂ symmetric supercapacitor in different potential windows at 100 mv/s scan rate. (b) Capacitance retention upon 2000 cycles of CV.

C. Permission License



This is a License Agreement between Sensu Tunca ("User") and Copyright Clearance Center, Inc. ("CCC") on behalf of the Rightsholder identified in the order details below. The license consists of the order details, the CCC Terms and Conditions below, and any Rightsholder Terms and Conditions which are included below.

All payments must be made in full to CCC in accordance with the CCC Terms and Conditions below.

Order Date	26-Jul-2021	Type of Use	Republish in a thesis/dissertation
Order License ID	1136008-1	Publisher	RSC Pub
ISSN	2040-3364	Portion	Image/photo/illustration

LICENSED CONTENT

Publication Title	Nanoscale	Language	English
Article Title	Highly Stable Silver-Platinum Core-Shell Nanowires for H ₂ O ₂ Detection	Country	United Kingdom of Great Britain and Northern Ireland
Author/Editor	Guo jia na mi ke xue zhong xin (China), Royal Society of Chemistry (Great Britain)	Rightsholder	Royal Society of Chemistry
Date	01/01/2009	Publication Type	Journal

REQUEST DETAILS

Portion Type	Image/photo/illustration	Distribution	Worldwide
Number of Images / photos / illustrations	5	Translation	Original language of publication
Format (select all that apply)	Print, Electronic	Copies for the disabled?	No
Who will republish the content?	Author of requested content	Minor editing privileges?	No
Duration of Use	Life of current edition	Incidental promotional use?	No
Lifetime Unit Quantity	Up to 499	Currency	USD
Rights Requested	Main product		

NEW WORK DETAILS

Title	SILVER-PLATINUM CORE-SHELL NANOWIRES FOR ELECTROCHEMICAL APPLICATIONS	Institution name	Middle East Technical University
Instructor name	Sensu Tunca	Expected presentation date	2021-08-15

ADDITIONAL DETAILS

Order reference number	N/A	The requesting person / organization to appear on the license	Sensu Tunca
------------------------	-----	---	-------------

REUSE CONTENT DETAILS

Title, description or numeric reference of the portion(s)	Figure 1 (g), (h), (i)	Title of the article/chapter the portion is from	Highly Stable Silver-Platinum Core-Shell Nanowires for H ₂ O ₂ Detection
Editor of portion(s)	Koylan, Serkan; Tunca, Senu; Polat, Gokhan; Durukan, Mete batuhan; Kim, Donggiwan; Kalay, Yunus Eren; Ko, Seung Hwan; Unalan, Husnu Emrah	Author of portion(s)	Koylan, Serkan; Tunca, Senu; Polat, Gokhan; Durukan, Mete batuhan; Kim, Donggiwan; Kalay, Yunus Eren; Ko, Seung Hwan; Unalan, Husnu Emrah
Volume of serial or monograph	N/A	Issue, if republishing an article from a serial	N/A
Page or page range of portion	5	Publication date of portion	2021-06-28

CCC Terms and Conditions

1. **Description of Service; Defined Terms.** This Reproduction License enables the User to obtain licenses for reproduction of one or more copyrighted works as described in detail on the relevant Order Confirmation (the "Work(s)"). Copyright Clearance Center, Inc. ("CCC") grants licenses through the Service on behalf of the rightsholder identified on the Order Confirmation (the "Rightsholder"). "Reproduction", as used herein, generally means the inclusion of a Work, in whole or in part, in a new work or works, also as described on the Order Confirmation. "User", as used herein, means the person or entity making such reproduction.
2. The terms set forth in the relevant Order Confirmation, and any terms set by the Rightsholder with respect to a particular Work, govern the terms of use of Works in connection with the Service. By using the Service, the person transacting for a reproduction license on behalf of the User represents and warrants that he/she/it (a) has been duly authorized by the User to accept, and hereby does accept, all such terms and conditions on behalf of User, and (b) shall inform User of all such terms and conditions. In the event such person is a "freelancer" or other third party independent of User and CCC, such party shall be deemed jointly a "User" for purposes of these terms and conditions. In any event, User shall be deemed to have accepted and agreed to all such terms and conditions if User reproduces the Work in any fashion.
3. **Scope of License; Limitations and Obligations.**
 - 3.1. All Works and all rights therein, including copyright rights, remain the sole and exclusive property of the Rightsholder. The license created by the exchange of an Order Confirmation (and/or any invoice) and payment by User of the full amount set forth on that document includes only those rights expressly set forth in the Order Confirmation and in these terms and conditions, and conveys no other rights in the Work(s) to User. All rights not expressly granted are hereby reserved.
 - 3.2. **General Payment Terms:** You may pay by credit card or through an account with us payable at the end of the month. If you and we agree that you may establish a standing account with CCC, then the following terms apply: Remit Payment to: Copyright Clearance Center, 29118 Network Place, Chicago, IL 60673-1291. **Payments Due:** Invoices are payable upon their delivery to you (or upon our notice to you that they are available to you for downloading). After 30 days, outstanding amounts will be subject to a service charge of 1-1/2% per month or, if less, the maximum rate allowed by applicable law. Unless otherwise specifically set forth in the Order Confirmation or in a separate written agreement signed by CCC, invoices are due and payable on "net 30" terms. While User may exercise the rights licensed immediately upon issuance of the Order Confirmation, the license is automatically revoked and is null and void, as if it had never been issued, if complete payment for the license is not received on a timely basis either from User directly or through a payment agent, such as a credit card company.
 - 3.3. Unless otherwise provided in the Order Confirmation, any grant of rights to User (i) is "one-time" (including the editions and product family specified in the license), (ii) is non-exclusive and non-transferable and (iii) is subject to any and all limitations and restrictions (such as, but not limited to, limitations on duration of use or circulation) included in the Order Confirmation or invoice and/or in these terms and conditions. Upon completion of the licensed use, User shall either secure a new permission for further use of the Work(s) or immediately cease any new use of the Work(s) and shall render inaccessible (such as by deleting or by removing or severing links or other locators) any further copies of the Work (except for copies printed on paper in accordance with this license and still in User's stock at the end of such period).

- 3.4. In the event that the material for which a republication license is sought includes third party materials (such as photographs, illustrations, graphs, inserts and similar materials) which are identified in such material as having been used by permission, User is responsible for identifying, and seeking separate licenses (under this Service or otherwise) for, any of such third party materials; without a separate license, such third party materials may not be used.
- 3.5. Use of proper copyright notice for a Work is required as a condition of any license granted under the Service. Unless otherwise provided in the Order Confirmation, a proper copyright notice will read substantially as follows: "Republished with permission of [Rightsholder's name], from [Work's title, author, volume, edition number and year of copyright]; permission conveyed through Copyright Clearance Center, Inc. " Such notice must be provided in a reasonably legible font size and must be placed either immediately adjacent to the Work as used (for example, as part of a by-line or footnote but not as a separate electronic link) or in the place where substantially all other credits or notices for the new work containing the republished Work are located. Failure to include the required notice results in loss to the Rightsholder and CCC, and the User shall be liable to pay liquidated damages for each such failure equal to twice the use fee specified in the Order Confirmation, in addition to the use fee itself and any other fees and charges specified.
- 3.6. User may only make alterations to the Work if and as expressly set forth in the Order Confirmation. No Work may be used in any way that is defamatory, violates the rights of third parties (including such third parties' rights of copyright, privacy, publicity, or other tangible or intangible property), or is otherwise illegal, sexually explicit or obscene. In addition, User may not conjoin a Work with any other material that may result in damage to the reputation of the Rightsholder. User agrees to inform CCC if it becomes aware of any infringement of any rights in a Work and to cooperate with any reasonable request of CCC or the Rightsholder in connection therewith.
4. Indemnity. User hereby indemnifies and agrees to defend the Rightsholder and CCC, and their respective employees and directors, against all claims, liability, damages, costs and expenses, including legal fees and expenses, arising out of any use of a Work beyond the scope of the rights granted herein, or any use of a Work which has been altered in any unauthorized way by User, including claims of defamation or infringement of rights of copyright, publicity, privacy or other tangible or intangible property.
5. Limitation of Liability. UNDER NO CIRCUMSTANCES WILL CCC OR THE RIGHTSHOLDER BE LIABLE FOR ANY DIRECT, INDIRECT, CONSEQUENTIAL OR INCIDENTAL DAMAGES (INCLUDING WITHOUT LIMITATION DAMAGES FOR LOSS OF BUSINESS PROFITS OR INFORMATION, OR FOR BUSINESS INTERRUPTION) ARISING OUT OF THE USE OR INABILITY TO USE A WORK, EVEN IF ONE OF THEM HAS BEEN ADVISED OF THE POSSIBILITY OF SUCH DAMAGES. In any event, the total liability of the Rightsholder and CCC (including their respective employees and directors) shall not exceed the total amount actually paid by User for this license. User assumes full liability for the actions and omissions of its principals, employees, agents, affiliates, successors and assigns.
6. Limited Warranties. THE WORK(S) AND RIGHT(S) ARE PROVIDED "AS IS". CCC HAS THE RIGHT TO GRANT TO USER THE RIGHTS GRANTED IN THE ORDER CONFIRMATION DOCUMENT. CCC AND THE RIGHTSHOLDER DISCLAIM ALL OTHER WARRANTIES RELATING TO THE WORK(S) AND RIGHT(S), EITHER EXPRESS OR IMPLIED, INCLUDING WITHOUT LIMITATION IMPLIED WARRANTIES OF MERCHANTABILITY OR FITNESS FOR A PARTICULAR PURPOSE. ADDITIONAL RIGHTS MAY BE REQUIRED TO USE ILLUSTRATIONS, GRAPHS, PHOTOGRAPHS, ABSTRACTS, INSERTS OR OTHER PORTIONS OF THE WORK (AS OPPOSED TO THE ENTIRE WORK) IN A MANNER CONTEMPLATED BY USER; USER UNDERSTANDS AND AGREES THAT NEITHER CCC NOR THE RIGHTSHOLDER MAY HAVE SUCH ADDITIONAL RIGHTS TO GRANT.
7. Effect of Breach. Any failure by User to pay any amount when due, or any use by User of a Work beyond the scope of the license set forth in the Order Confirmation and/or these terms and conditions, shall be a material breach of the license created by the Order Confirmation and these terms and conditions. Any breach not cured within 30 days of written notice thereof shall result in immediate termination of such license without further notice. Any unauthorized (but licensable) use of a Work that is terminated immediately upon notice thereof may be liquidated by payment of the Rightsholder's ordinary license price therefor; any unauthorized (and unlicensable) use that is not terminated immediately for any reason (including, for example, because materials containing the Work cannot reasonably be recalled) will be subject to all remedies available at law or in equity, but in no event to a payment of less than three times the Rightsholder's ordinary license price for the most closely analogous licensable use plus Rightsholder's and/or CCC's costs and expenses incurred in collecting such payment.

8. Miscellaneous.

- 8.1. User acknowledges that CCC may, from time to time, make changes or additions to the Service or to these terms and conditions, and CCC reserves the right to send notice to the User by electronic mail or otherwise for the purposes of notifying User of such changes or additions; provided that any such changes or additions shall not apply to permissions already secured and paid for.
- 8.2. Use of User-related information collected through the Service is governed by CCC's privacy policy, available online here: <https://marketplace.copyright.com/rs-ui-web/mp/privacy-policy>
- 8.3. The licensing transaction described in the Order Confirmation is personal to User. Therefore, User may not assign or transfer to any other person (whether a natural person or an organization of any kind) the license created by the Order Confirmation and these terms and conditions or any rights granted hereunder; provided, however, that User may assign such license in its entirety on written notice to CCC in the event of a transfer of all or substantially all of User's rights in the new material which includes the Work(s) licensed under this Service.
- 8.4. No amendment or waiver of any terms is binding unless set forth in writing and signed by the parties. The Rightsholder and CCC hereby object to any terms contained in any writing prepared by the User or its principals, employees, agents or affiliates and purporting to govern or otherwise relate to the licensing transaction described in the Order Confirmation, which terms are in any way inconsistent with any terms set forth in the Order Confirmation and/or in these terms and conditions or CCC's standard operating procedures, whether such writing is prepared prior to, simultaneously with or subsequent to the Order Confirmation, and whether such writing appears on a copy of the Order Confirmation or in a separate instrument.
- 8.5. The licensing transaction described in the Order Confirmation document shall be governed by and construed under the law of the State of New York, USA, without regard to the principles thereof of conflicts of law. Any case, controversy, suit, action, or proceeding arising out of, in connection with, or related to such licensing transaction shall be brought, at CCC's sole discretion, in any federal or state court located in the County of New York, State of New York, USA, or in any federal or state court whose geographical jurisdiction covers the location of the Rightsholder set forth in the Order Confirmation. The parties expressly submit to the personal jurisdiction and venue of each such federal or state court. If you have any comments or questions about the Service or Copyright Clearance Center, please contact us at 978-750-8400 or send an e-mail to support@copyright.com.

v1.1